LBL-34882
UC-404

Lawrence Berkeley Laboratory
UNIVERSITY OF CALIFORNIA

Materials Sciences Division

Applications of Highly Spin-Polarized Xenon in NMR

H.W. Long
(Ph.D. Thesis)

September 1993

Prepared for the U.S. Department of Energy under Contract Number DE-AC03-76SF00098

DISCLAIMER

LBL-34882
UC-404

Applications of Highly Spin-Polarized Xenon in NMR

Henry W. Long

Department of Chemistry
University of California

and

Materials Sciences Division
Lawrence Berkeley Laboratory
University of California
Berkeley, California 94720

September 1993

This work was supported by the Director, Office of Energy Research, Office of Basic Energy Sciences, Materials Sciences Division, of the U.S. Department of Energy under Contract No. DE-AC03-76SF00098.

Applications of Highly Spin-Polarized Xenon in NMR

by

Henry W. Long

Abstract

Applications of Highly Spin-Polarized Xenon in NMR

by

Henry W. Long

Doctor of Philosophy in Chemistry
University of California at Berkeley
Professor Alexander Pines, Chair

For the past ten years xenon NMR has increased steadily in importance as a spectroscopically sensitive probe of a wide variety of materials and their surfaces. Most samples studied to date have relatively high surface area where enough xenon can be loaded so as to generate sufficient signal-to-noise ratios for the studies to be undertaken. The success of xenon NMR in the study of these systems adds impetus to allow information to be obtained from more materials. The main goal of the work presented in this thesis is produce highly spin-polarized xenon to create much greater signal intensities (up to 54,000 times greater) so as to allow studies to be made on systems with low surface area and long spin-lattice relaxation times. The spin-exchange optical pumping technique used to create high nuclear spin polarization is described in detail in chapter two. This technique is initially applied to some multiple-pulse optically detected NMR experiments in low magnetic field (50G) that allow the study of quadrupolar interactions with a surface of only a few square centimeters. In chapter three the apparatus used to allow high field ^{129}Xe NMR studies to be performed with extremely high sensitivity is described and applied to experiments on diamagnetic susceptibility effects in thin ($\approx$2000 layers) films of frozen xenon. Preliminary surface investigations of laser polarized ^{129}Xe adsorbed an a variety of materials (salts, molecular crystals, amorphous carbon, graphite) are then discussed. A full detailed study of the surface of a particular polymer, poly(acrylic acid), is presented in chapter four which shows the kind of detailed information that can be obtained from this technique. Along with preliminary results for

several similar polymers, a summary is given of xenon studies of a novel ultra-high surface area polymer, poly(triarylcarbinol). Finally in chapter five the exciting possibility of transferring the high spin order of the laser polarized xenon to other nuclei is discussed and several schemes are proposed. Highly spin-polarized xenon has been used to transfer nuclear spin order to $^{13}CO_2$ in a xenon matrix and to protons on poly(triarylcarbinol).

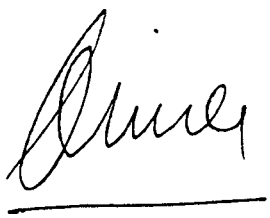

Table of Contents

List of Figures

Acknowledgements

It is a pleasure to thank the many people that I have worked with over the past five years at Berkeley. Without all of their help the work presented in this thesis could not have been done. First, my advisor Alex Pines provided a very stimulating and challenging laboratory in which to work. I thank him for his time, commitment and inspiration. Professor Jeff Reimer was a supportive collaborator. Dan Raftery was an excellent co-worker and originally got me involved in his "weekend project". Phil Grandinetti, Linda Reven and Pei Tang were fantastic postdocs who put in a great deal of work on various aspects of the project. Thomas Meersmann came from Tübingen for one year and contributed a great deal to the design of the high field experiment. Jay Shore, Tanya Pietraβ, and Russ Bowers injected considerable talent into the project at key times which kept everything moving ahead. Holly Gaede has been a very congenial co-worker over the past two years and I wish her well in her continuing work. Joe, Raz, Bruce, Jay and the rest of the Pinenuts were all very supportive.

The departmental shops were extremely helpful and cheerful about sharing their expertise to construct the many parts of the experiment. In particular Tom and Cathy in the glass shop devoted a great deal of time and effort to create the glassware for all of the experiments described herein.

Most importantly I would like to thank my family for their encouragement and support of my education.

CHAPTER 1 Introduction

Nuclear magnetic resonance (NMR) has been a technique of enormous utility in science, technology and medicine. It is a non-invasive, local probe of chemical environments that has reached a high degree of sophistication in the forty years since its discovery. Two general issues facing all spectroscopic techniques are resolution and sensitivity. High resolution has long been achieved in NMR simply due to the presence of rapid thermal motion such as is present in liquids [1]. In solids the appropriate mechanical reorientation of the sample (sometimes with multiple rf pulses) achieves in some cases the same line narrowing effect as in liquids [2, 3]. Low sensitivity, however, is inherent with NMR due to the low transition frequencies involved (tens to hundreds of megahertz or $\approx 10^{-6}$ eV). The nuclear polarization (the relative population excess of spins pointing along the field over those pointing against the field) is only a few parts per million even in the highest magnetic fields available. Sensitivity limitations can impair or render impossible the study of certain physical systems such as surfaces. A recently developed technique in atomic physics, spin-exchange optical pumping [4], offers to increase the nuclear polarization of noble gas atoms by several orders of magnitude. The main topic of this thesis is the application of highly spin polarized xenon to the study of surfaces either indirectly, through the xenon NMR parameters (chapters 3,4), or directly, through polarization transfer to the surface itself (chapter 5).

This introductory chapter discusses several sensitivity enhancement techniques that have been used in NMR and outlines the theory of the chemical shift interaction by which information about a nuclei's environment is detected. The success of xenon NMR in studying a wide variety of materials is reviewed in a general fashion followed by a summary of two specific systems studied with conventional xenon NMR.

1.1 Sensitivity Considerations in NMR

A population difference is required for the net absorption or emission of energy and the relative populations of adjacent energy levels in thermal equilibrium are given by the Boltzmann distribution

$$\frac{N_m}{N_{m+1}} = e^{-\beta\Delta E} = e^{-\gamma\hbar H/kT}. \tag{1.1}$$

This is more conveniently discussed by introducing the fractional polarization of a two level system:

$$\wp = \frac{N_+ - N_-}{N_+ + N_-}. \tag{1.2}$$

This can be expressed using (1.1) as

$$\wp = \tanh(\beta\Delta E) \approx \tfrac{1}{2}\beta\Delta E. \tag{1.3}$$

The magnetization of a sample is obtained by multiplying the polarization by the magnetic moment and number density of the nuclei. Typical parameters for ^{129}Xe NMR are a magnetic field of 4.3 Tesla, T=300K, giving $\Delta E/h$ =50 MHz, kT=0.026 eV. These parameters lead to a polarization of $\wp$ = 4.0 parts per million (ppm). In contrast, for optical spectroscopy typical energy differences are on the order of 1 eV and the polarization of the electronic energy levels is of order unity. While a more complete analysis of the signal-to-noise ratio of an NMR experiment [5] shows that it scales as the frequency to the 3/2 power

(for a solenoid coil), the signal is directly proportional to the polarization. This sets a rough limit of approximately 10^{18} nuclei that can be detected in one scan (cf. figure 3.4).

Naturally many methods have been invented to increase the sensitivity. The most straightforward is simply to signal average. The signal adds in linearly with the number of scans N while the random noise increases only as the square root, $\sqrt{N}$, thus the signal to noise increases as $N/\sqrt{N} = \sqrt{N}$. However, one can only acquire scans as rapidly as the magnetization of the spin system is replenished by the lattice (i.e. T_1), and, when the relaxation time is long, this can be a severe limitation. Examining equation 1.1 shows one obvious approach to increasing the magnetization acquired in a single scan is to lower the temperature. In practice for significant (>10) enhancement this requires a temperature below 1K and the spin-lattice relaxation times in insulating solids typically becomes so long (months to years [6, 7]) at these temperatures that high nuclear spin polarization is not simply obtained by this method. The only practical method of exploiting this approach has been developed by Waugh and co-workers [7, 8, 9] who have immersed samples in liquid ^{3}He to provide a relaxation mechanism for nuclei at millikelvin temperatures.

One of the most widely used sensitivity enhancement techniques in NMR is cross polarization (CP) [10, 11]. Equation 1.1 shows that when all nuclei are at thermodynamic equilibrium (i.e. they have the same spin temperature equal to the lattice temperature), nuclei with larger gyromagnetic ratios, γ, will have a larger polarization due to their larger energy level splittings (higher NMR frequency). Protons, which have the largest γ, are more sensitively observed than any other nucleus. Techniques to exploit this have become very widely used since the pioneering work of Hartmann and Hahn [10] and Pines, Gibby, Waugh [11]. Cross polarization is an extremely valuable technique as it allows an increase in single shot magnetization as well as a faster signal averaging at the T_1 of the abundant species. Cross polarization will be discussed in more detail in chapter 5.

Electrons have magnetic moments about 2000 times larger than nuclear moments and correspondingly larger polarization. Several schemes have exploited electron-nuclear

couplings to use this higher polarization either directly or indirectly. Examples are ENDOR (electron nuclear double resonance) [12], DNP (dynamic nuclear polarization) and the solid effect [13]. Reaction dynamics involving radical recombination have been observed to lead to enhanced nuclear polarization in an effect known as CIDNP (chemically induced dynamic nuclear polarization) [14, 15]. Reactions that exploit the polarization of rotational states in parahydrogen also lead to similar effects known as PASADENA (parahydrogen and synthesis allow dramatically enhanced nuclear alignment) [16, 17]. Here the magnetization is not directly created as a population difference but from a more subtle form of spin order.

A different means of achieving higher sensitivity is to employ an alternative detection method. In luminescent solids NMR transitions may affect the polarization or intensity of the emitted light [18]. In the gas phase certain atoms can be very sensitively detected by optical characteristics that depend upon the ground state sublevel distribution. A technique of this nature (paramagnetic Faraday rotation) will be used in chapter 2 to indirectly detect xenon in the gas phase. It is of some interest to note that there is at least one method of detection where polarization is not needed. In the molecular beam resonance method of Rabi [19], a particle is detected by a change in flux at the detector irrespective of whether it has gained or lost energy as both cause a deflection of the beam. The detection sensitivity of this technique is extremely high.

1.2 Chemical Shift Interaction

The most important observable (spin interaction) in using ^{129}Xe as a probe of its environment is the chemical shift. (The quadrupole interaction is dominant for ^{131}Xe and will be discussed briefly in section 2.2.) This interaction is responsible for small frequency shifts that are characteristic of perturbations of the immediate electronic environment. The origin of the chemical shift is the magnetic coupling of the *orbital* angular momentum of the electrons with the nuclear spin angular momentum. (The electron *spin* angular momentum

coupling with the nucleus gives rise to the Knight shift, that is important when there are unpaired electron spins.) The orbital angular momentum of a charged particle (the electron) gives rise to a magnetic field that changes the local magnetic field at the nucleus. The interaction is zero when there is no applied magnetic field since the angular momentum is quenched by the crystalline electric fields. In the presence of an external magnetic field, the electronic Zeeman interaction slightly polarizes the electron system, "unquenching" the orbital angular momentum which leads to an non zero coupling [20].

The most general interaction between two vectors (in this case the nuclear magnetic moment, $\gamma\hbar\vec{I}$, and the magnetic field, $\vec{B}$) is by contraction with a second rank tensor (typically denoted $\bar{\bar{\sigma}}$ for the chemical shift)

$$H = \hbar\gamma\vec{I}\cdot\bar{\bar{\sigma}}\cdot\vec{B}. \tag{1.4}$$

This interaction can be decomposed into two parts that will be discussed separately.

1.2.1 Isotropic Shifts of Xenon

In the presence of rapid motion only the invariant (isotropic) part of the tensor remains, $\frac{1}{3}\mathrm{Tr}(\bar{\bar{\sigma}}) = \sigma_{iso}$, and the net effect is a small change in the magnetic field strength seen by the nucleus that can be written as a change in the resonance frequency

$$\omega = \gamma B_{tot} = \gamma B_o(1-\sigma_{iso}). \tag{1.5}$$

For closed shell atomic systems, such as xenon, a derivation of the shielding in the absence of additional external perturbations is straightforward and has been given by Lamb [21]. The general Hamiltonian in the presence of a vector potential, A, is

$$\hat{H} = \frac{1}{2m}\left(p+\frac{e}{c}A\right)^2 + V \qquad A = A_{nuc} + A_{elec} \tag{1.6}$$

where a definite gauge (Coulomb) has been assumed chosen for the vector potential [22]. There are two contributions that can have equal magnitude to the chemical shift from

perturbation theory, a first order cross term in $A_{elec}A_{nuc}$, and a second order contribution from the term linear in A_{elec}. The first order term is dominant for isolated atoms and gives rise to the diamagnetic shielding,

$$\sigma_D = -\frac{e^2}{3mc^2}\left\langle \sum_i \frac{1}{r_i} \right\rangle. \tag{1.7}$$

Some conclusions can be read directly from this formula. First. the 1/r expectation value implies that only local perturbations in the (ground state) electronic environment are important in determining the chemical shift (as opposed to susceptibility, which has an r^2 dependence on the electronic wavefunction and will be discussed in chapter 3). Second, since it involves a sum over the electrons, *i*, and the atomic number (Z) of xenon is 54, it can be expected to rather large. In fact it has been estimated by Hartree-Fock calculations to be 5744 ppm [23] (cf. Xe^{54+} in figure 1.1). Thus, in the absence of other perturbations, in an applied field of 10,000 G the xenon nucleus sees an effective field that is 57.4 G smaller.

Paramagnetic contributions to the chemical shift are important in the few xenon compounds that have been studied [24], although in a molecular system there is no unique origin and thus the division into diamagnetic and paramagnetic contributions depends on the choice of gauge [22]. The paramagnetic contribution has been derived by Ramsey [25], and may be written as

$$\sigma_P = \frac{e^2h^2}{2m^2c^2}\sum_n \frac{\langle 0|\sum_i \frac{\vec{L}_i}{r_i^2}|n\rangle\langle n|\sum_k L_{zk}|0\rangle}{E_n - E_0}. \tag{1.8}$$

This equation involves a sum over all of the energy levels of the system which accounts for the difficulty in *ab initio* calculations of chemical shielding.

During a collision, when the xenon can be considered part of a molecular complex, the "deformation of the electron cloud" (i.e. excitation of the xenon into a superposition of excited electronic states of the unperturbed system) can lead to isotropic paramagnetic

shifts, (deshielding), when averaged over many collisions [26, 27]. These shifts are virtually impossible to interpret on the fundamental level of equations 1.7 and 1.8, however they can still lead to extremely useful information about chemical systems when studied systematically as a function of some appropriate external parameter such as pressure, temperature or a structural property of a material. Isotropic shifts of xenon in a wide variety of environments are shown in figure 1.1 and are discussed more fully at the beginning of section 1.3.

1.2.1 Anisotropic Shifts of Xenon

In an anisotropic environment, such as a solid or liquid crystal, in addition to the isotropic part the chemical shift has an orientation dependent component [2]. It is described by the symmetric traceless part of $\bar{\bar{\sigma}}$ that can be written as

$$\sigma = \sigma^{ref} + \Delta\sigma\left[\tfrac{1}{2}(3\cos^2\theta - 1) + \tfrac{1}{2}\eta\sin^2\theta\cos\varphi\right], \qquad (1.9)$$

where (θ,φ) are the polar angles of the direction of the principal axis of the tensor with respect to the external magnetic field, $\bar{B}$ [2]. Only cases where the asymmetry parameter η is zero will be considered. In this case the frequency of the NMR transition can be written (in ppm) as

$$\omega = \Delta\sigma(\cos^2\theta - \tfrac{1}{3}). \qquad (1.10)$$

For a random distribution of environments (such as crystallites in a powder), if the distributions of axis systems is plotted on a sphere then it will be constant. Thus the integrated intensity of the line I(ω) will be proportional to an integral over a sphere:

$$\int I(\omega)d\omega = \iint \sin\theta d\theta d\varphi. \qquad (1.11)$$

On the right hand side of equation 1.11 one integrates over φ and changes variables from θ to an integral over ω by inverting equation 1.10

$$\theta = \arccos\sqrt{\left(\tfrac{\omega}{\Delta\sigma} + \tfrac{1}{3}\right)}. \qquad (1.12)$$

Substituting this into (1.11) leads to two integrals that are equal (for the same limits). Therefore their integrands can be equated yielding the final answer:

$$I(\omega) = \frac{\sqrt{3}}{2\Delta\sigma} \frac{1}{\sqrt{1 + (3\omega / \Delta\sigma)}} . \qquad (1.13)$$

In this equation the frequency varies from $-\Delta\sigma/3 \leq \omega \leq 2\Delta\sigma/3$ (according to equation 1.10) and the intensity has a characteristic singularity at $-\Delta\sigma/3$. This is the line shape for an axially symmetric shielding tensor; examples are the ^{129}Xe spectra of XeF_2 (a linear molecule) in the solid state, figure 1.3, and the ^{129}Xe spectra of xenon/β–quinol clathrate compound, figure 5.1.

In this derivation it was assumed that the principal axis system is isotropically distributed in three dimensional space, however, there are physical situations where this is not true [28, 29]. One such system was studied by Opella and Waugh [30] where an extruded polymer film (polyethylene) had been partially oriented and there was disorder in only two dimensions. The line shape for this situation is derived by integrating equation 1.11 over a cylinder (i.e. the integrand is just $d\theta$). The result is

$$I(\omega) = \Delta\sigma \frac{1}{\sqrt{1 - \left(\frac{2\omega}{\Delta\sigma}\right)^2}}, \qquad (1.14)$$

which is readily identified as it has two singularities at $\pm\Delta\sigma/2$. Simulations appear in figure 1.2 of the chemical shift anisotropy line shape for both situations.

1.3 Examples of Xenon as a Probe

The use of atomic xenon as a probe or spy of different chemical environments has increased dramatically in the past ten years since the pioneering studies of xenon in solutions [31], zeolites [32], and clathrates [33, 34]. There have been many subsequent applications to a wide variety of materials and a few characteristic xenon isotropic chemical shifts are indicated on the bottom half of figure 1.1. The chemical shift of xenon in NaY

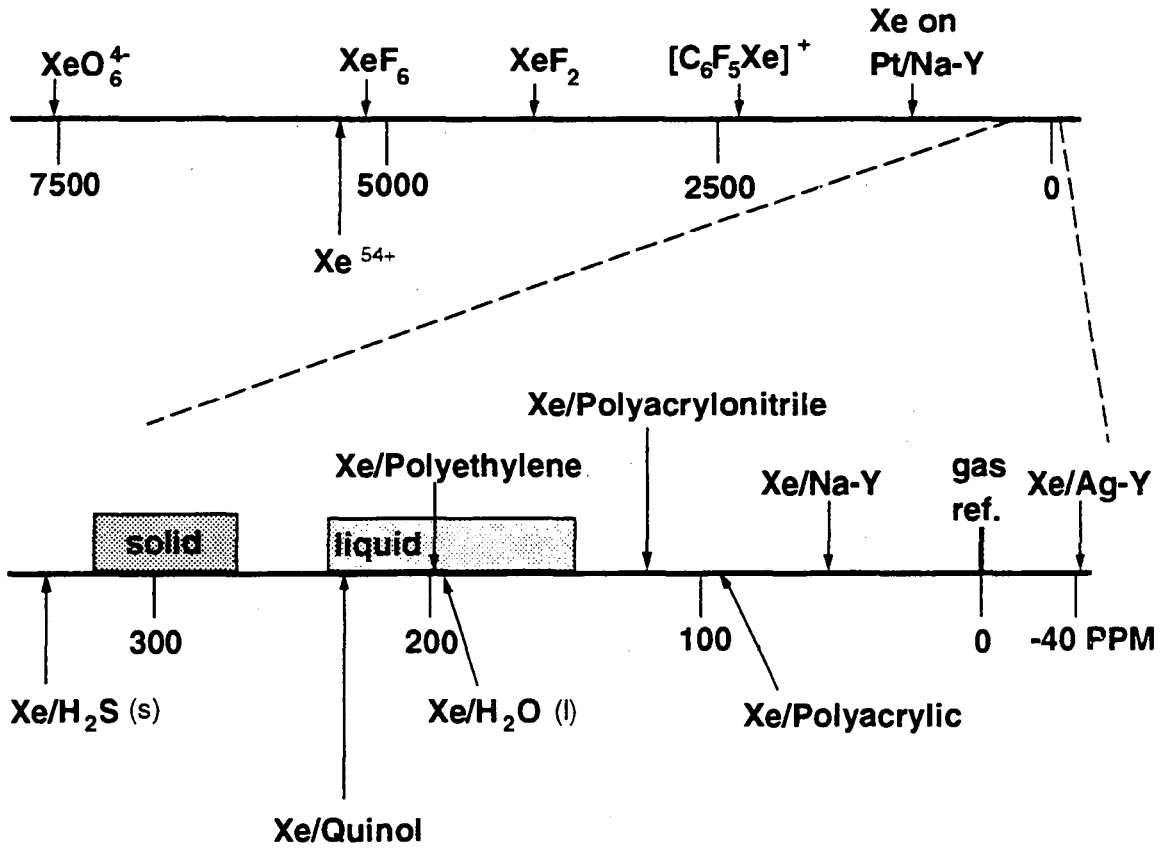

Figure 1.1 Isotropic chemical shift range of xenon with several examples. See the beginning of section 1.3 for comments on the various points.

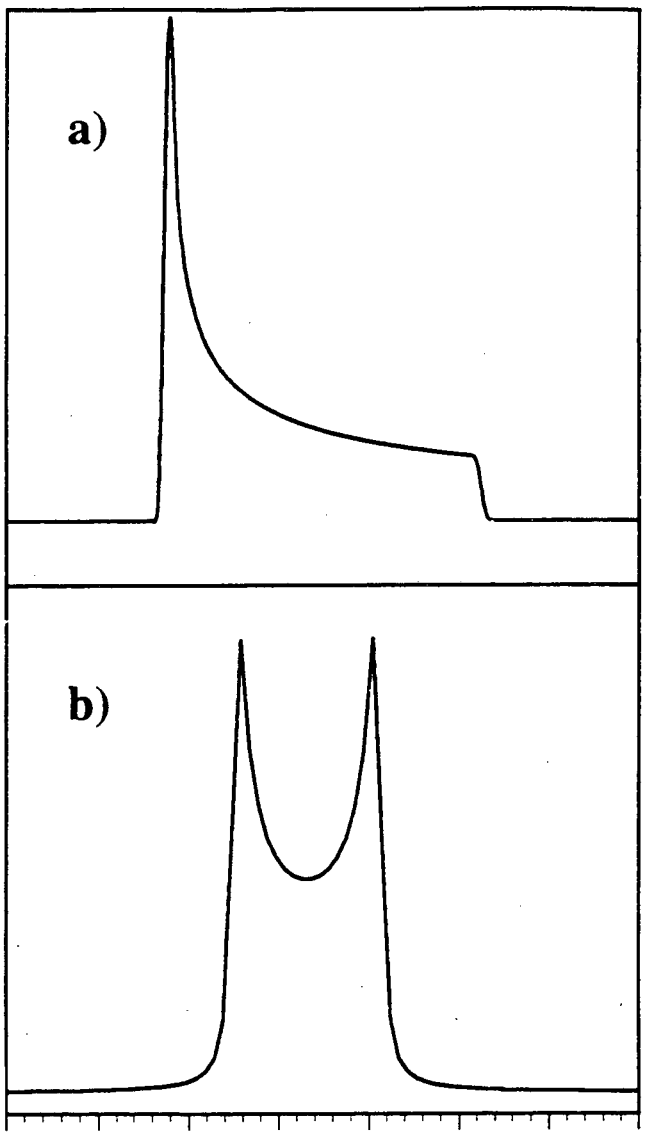

Figure 1.2 Line shape simulations of a) 3D and b) 2D chemical shift anisotropies with zero asymmetry parameter.

zeolite is 58 ppm in the limit of zero xenon loading showing the interaction with the catalyst framework. Xenon adsorbed in NaY with small platinum particles in the pores shows a much larger interaction [35] due to the Knight shift on the metal surface in agreement with the large shifts of small molecules on metal surfaces studied by Slichter and co-workers [36]. The only other zeolite point in figure 1.1 is the anomalous silver-Y zeolite system (AgY) that is the only system showing magnetic shielding greater than the pure gas [37]. Clearly this must be extra diamagnetic shielding and it has been ascribed to d-π back bonding from silver ions in the pore framework to the xenon. A simple clathrate is represented on the figure by the Xe/β-quinol system that is marked at the isotropic shift (222 ppm) of the broad (160 ppm) chemical shift anisotropy characteristic of the size and symmetry of the cage xenon is trapped in [33, 38] (see figure 5.1). The polyethylene point is the shift for xenon dissolved *into* the amorphous region of this polymer [39], while the polyacrylic and polyacrylonitrile points are the shifts for xenon adsorbed *onto* the surface of these polymers in the limit of zero coverage [40]. This type of surface chemical shift measurement will be discussed in detail in chapter 4.

Many review articles have been written on the use of xenon as a probe. Ito and Fraissard [41] have reviewed their pioneering work on zeolites. Barrie and Klinowski have written a more recent and candid article on xenon studies of zeolites and their potential [42]. Dybowski and Duncan [43] have reviewed the slightly wider area of xenon in confined environments. Raftery and Chmelka [44] have written a very broad overview of materials studies employing xenon and include a section on optical pumped xenon studies.

In the next sections two conventional xenon NMR studies are discussed. While they are not completely representative of the literature, they do give the flavor of xenon applications to materials investigations and illustrate the use of both xenon isotopes.

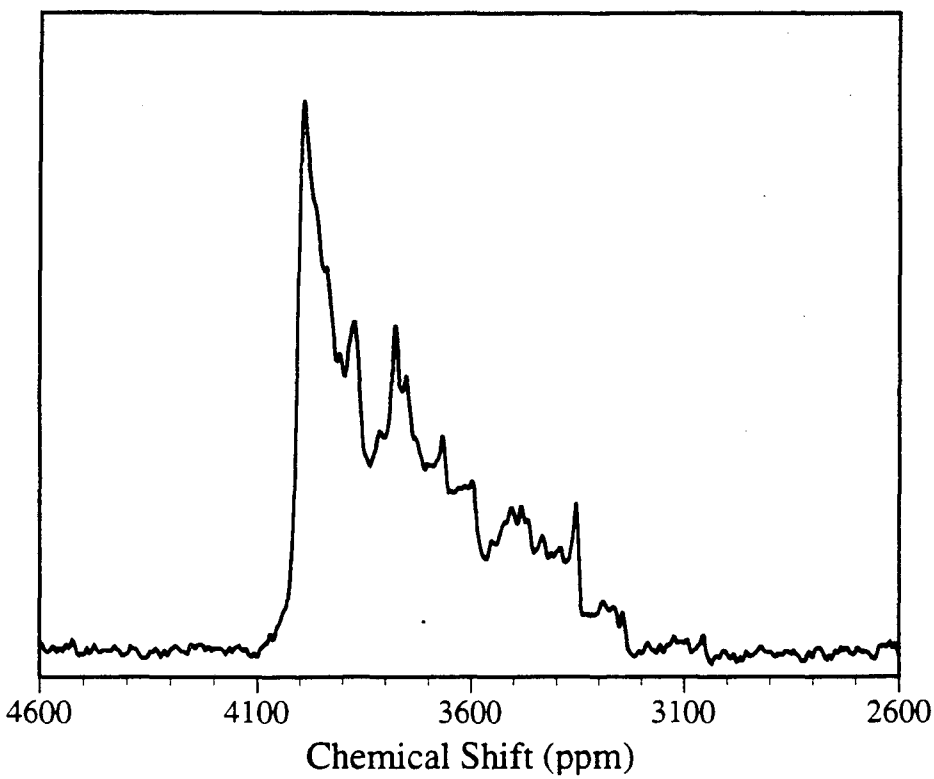

Figure 1.3 ^{129}Xe spectrum of polycrystalline XeF_2 with ^{19}F decoupling. NA=656, PD=60 sec., LB = 200 Hz. The chemical shift parameters are $\Delta\sigma$=771 ppm, σ_{iso} =3751 ppm from low pressure gas (σ_{iso} =3630 ppm for XeF_2 in solution with SO_2ClF [24]). The spectrum appears ragged due to the large average crystallite size.

1.3.1 Xenon in Confined Liquid Crystals

Liquid crystals have great technological importance due to the widespread use of liquid crystal displays (LCD's) [45, 46]. They are a phase of matter in which there is long range orientational order but no positional order. Since NMR parameters are very sensitive to orientation (such as chemical shift, equation 1.10), it is a particularly useful tool for studying liquid crystals [47]. A molecule dissolved in a liquid crystal is oriented on average along the director that acts as a local principal axis system. It was first observed in 1978 that ^{131}Xe showed isotropic quadrupolar splittings in a liquid crystal [48]. The spectrum showed a sharp triplet indicative of a well defined average electric field gradient at the nucleus that was homogeneous throughout the sample. Diehl and co-workers have used several noble gases [49, 50] with quadrupolar nuclei to perform a systematic study of several nematics and have attempted to explain the observed electric field gradients in the bulk liquid crystal [50].

Surfaces have interesting effects on liquid crystals. A grooved surface can strongly anchor the molecules parallel to the surface and various surfactants can also exert effects on the director field of the liquid crystal [51]. Experiments using optical techniques, such as surface ellipsometry, have long been able to investigate these effects [52], but NMR, lacking sufficient sensitivity to probe a surface of just a few square centimeters, had been capable only of bulk studies. Recently several high surface area systems have been investigated; sufficient liquid crystal material can be loaded in these systems to allow studies of selectively deuterated compounds, and surface effects were observed with NMR [53]. These systems are typically submicron sized cavities in which the liquid crystal behaves quite differently than the bulk. Usually, liquid crystals orient themselves along the direction of an applied magnetic field due to anisotropic diamagnetic susceptibility. When there are competing effects between a wall and a magnetic field, the effects of the wall decrease exponentially over a characteristic distance. This magnetic coherence length, ξ_m [54], is determined by the magnetic field strength B, the susceptibility anisotropy $\Delta\chi$, and

the elastic constant of the medium K through $\xi_m = (K/\Delta\chi)^{1/2} / B$. For the systems considered here this distance is on the order of 1 micron and thus the orientation of the director field is determined completely by the surface in these confined geometries.

Xenon NMR can provide valuable information about nuclear shielding and electric field gradients in liquid crystals that should be extended to these confined geometries. Xenon studies have the advantage that no special synthesis is required for the liquid crystal and different timescales are probed than in deuterium studies.

The high surface area liquid crystal system studied is an anopore™ membrane shown schematically in figure 1.4. These membranes are each about 60μ thick and may be cut into square sheets. They have an average pore diameter of 0.2μ and extremely high pore density — up to 10^9 pores/cm^2 giving BET surface areas (see chapter 4) of 10 m^2/g [55]. The membranes were treated with lecithin, which orients the liquid crystal director perpendicular at the surface of the pore, although there is a preferred direction at the center of the pore; this is known as the planar-polar structure (shown above the membrane in figure 1.4).

The anopores were then loaded with ZLI1132 (Merck, a mixture of several compounds) which has been well characterized in the bulk by xenon NMR. Several cells were constructed from square tubing to accommodate the membranes tightly and allow orientational studies to be performed easily. The anopores (≈100) were stacked into cells and one cell was loaded with 2 atm enriched ^{129}Xe, and another with 5 atm enriched ^{131}Xe. They were both briefly heated to above 100°C to let the xenon dissolve rapidly into the isotropic phase of the liquid crystal before starting the experiments.

In a bulk sample of ZLI1132 at 27°C the isotropic chemical shift of ^{129}Xe was measured to be 222 ppm with a line width of 1.5 ppm (equal to the magnetic field inhomogeneity). Figure 1.5 shows the spectrum of ^{129}Xe in the anopore sample with

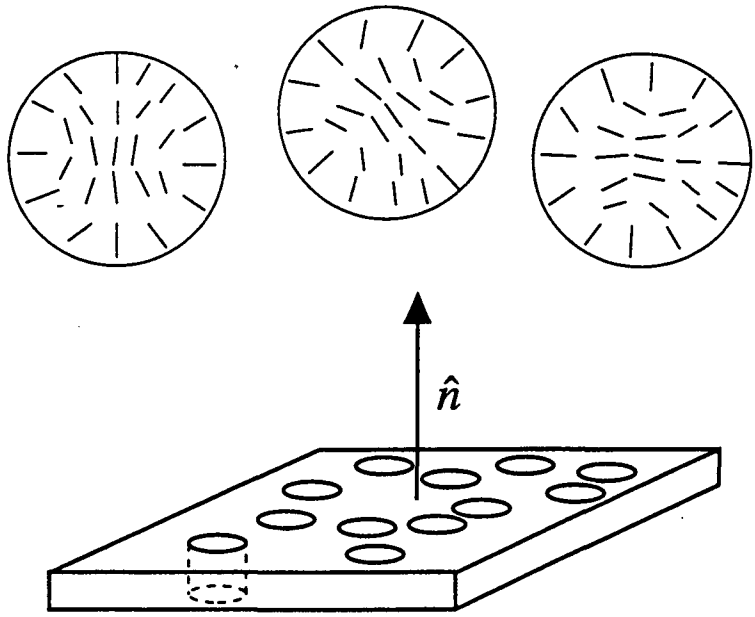

Figure 1.4 Schematic picture of an anopore membrane whose unit normal is denoted $\hat{n}$. The lecithin induced "planar polar" director field within the pores is sketched above.

various orientations of $\hat{n}$ (the normal to the membrane surface, which is itself perpendicular to all of the directors). There is a strong orientation dependence to the line shape. With $\hat{n} \perp \vec{B}$ an anisotropy of 12 ppm is observed; the line shape is in fact just the two dimensional "powder pattern" discussed in section 1.2.

The chemical shift anisotropy has been measured in several liquid crystals by observing the change in chemical shift at the nematic-isotropic transition [56]. This is subject to several experimental uncertainties due to the temperature and phase (mostly density) dependence of σ_{iso}, but from the data of Jokkisari and Diehl [57] the anisotropy appears to be 11 ppm for bulk ZLI1132. It should be noted that these researchers have reported the nematic-isotropic transition temperature to be 62°C in this liquid crystal, but it was measured to be 74°C in our (bulk) sample.

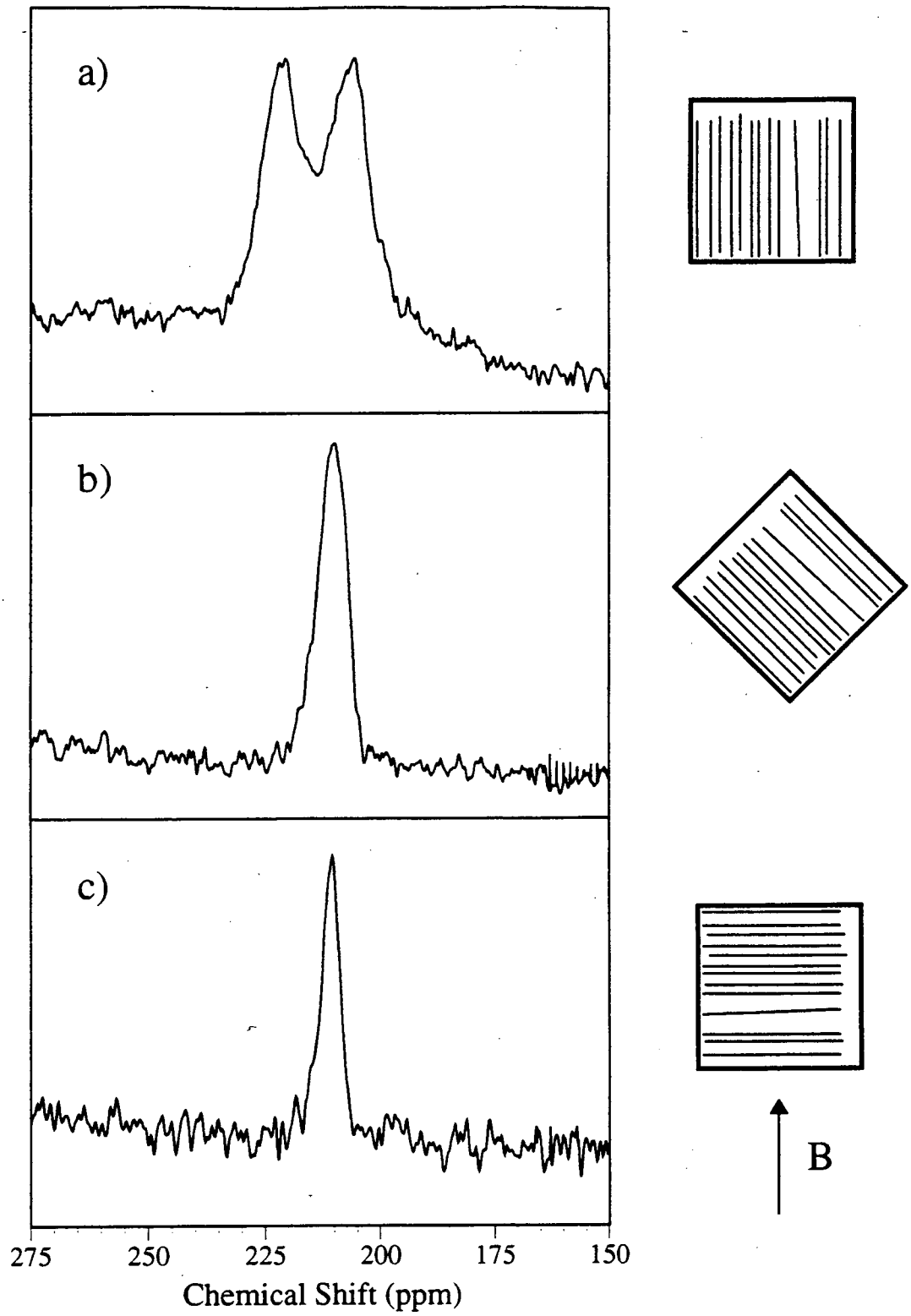

Figure 1.5 ^{129}Xe spectra in ZLI1132 confined within anopore membranes (T= 19°C) at various orientations with respect to the magnetic field. (a) $\hat{n} \perp \vec{B}$ (b) 45° (c) $\hat{n} \parallel \vec{B}$.

Figure 1.6 shows the spectrum of ^{131}Xe in a bulk sample of ZLI1132 and in the anopore sample with $\hat{n} \| \vec{B}$. The quadrupolar splitting (defined as the distance between satellites) in the bulk at 29°C is 207 kHz in agreement with previous work [58] (the satellite appears antiphase due to large phase distortion in the FID). The quadrupolar splitting has been measured as 230 kHz at 49°C in the bulk [58], but in the anopore membrane at 49°C the quadrupolar splitting is just 140 kHz. A scaling of 1/2 is anticipated if the liquid crystal is oriented perpendicular to the surface because, with this macroscopic orientation of the membranes, all of the directors are perpendicular to the field (cf. figure 1.4). The quadrupolar splitting is known to scale as $P_2(\cos\theta)$, where θ is the angle between the director and the magnetic field. Since the splitting is significantly more than one half of the bulk value it appears that the electric field gradient experienced by the xenon is larger in the confined liquid crystal than in the bulk. The satellite transitions are difficult to observe in the ^{131}Xe spectrum since they are broadened by temperature gradients over the sample and fluctuations over the acquisition time. Also, the anopores are not uniformly oriented, and a small distribution of orientations also broadens the transitions. The central transition is 1.2 kHz broad and the satellites are about 4.5 kHz in width. These broaden out rapidly upon rotating the sample and are unobservable at more than a few degrees.

There is clearly a distribution of directors within the pores as well as a distribution of polar directions amongst the pores. Either of these two distributions could explain the anisotropic line shape observed for ^{129}Xe. Thus to interpret the xenon NMR parameters that have been measured in this system the regions that the xenon is averaging over must be determined and the motion of the xenon quantified. The xenon dynamics were studied by two dimensional exchange spectroscopy [59, 60] which allows the xenon to be observed directly on timescales longer than the free induction decay. In this technique the resonance frequency of xenon at one point in time is correlated with its resonance frequency at fixed time later (t_{mix}), thus motion between distinct sites can be studied at times up to the spin-lattice relaxation time (which is about 20-30 seconds in this sample).

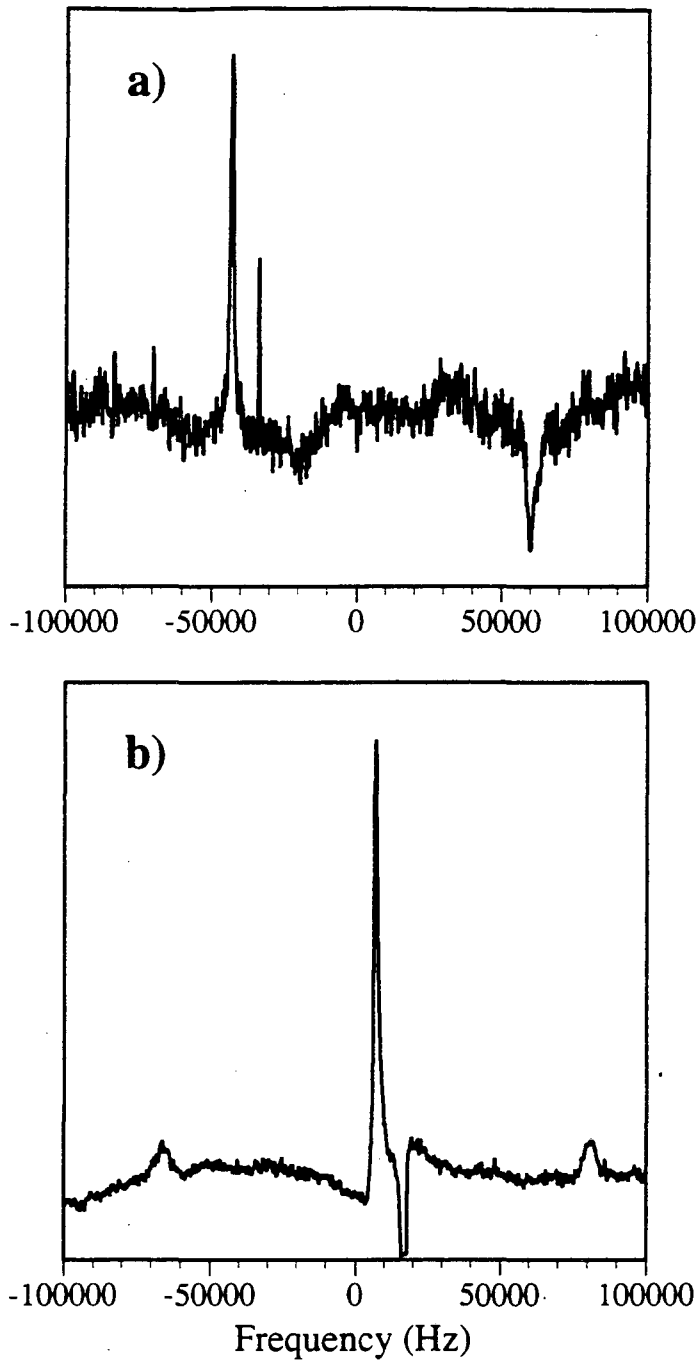

Figure 1.6 (a) ^{131}Xe spectra in bulk ZLI1132 showing the central transition and high frequency satellite, T=29°C, splitting = 207 kHz. NA= 333,000. (b) ^{131}Xe spectra in ZLI1132 within anopore membranes shows the entire triplet (and the gas phase peak which is inverted and truncated), T=48°C, splitting = 140 kHz. NA= 206,450.

Figure 1.7 shows the two dimensional exchange spectrum obtained with a mixing time of 200 msec. There are off diagonal peaks connecting the gas and liquid crystal resonances indicating exchange is occurring between these two regions within 200 msec. The expansion above the spectrum shows the detail of the liquid crystal region and clearly displays exchange among the different regions making up the liquid crystal line. This could be due to intrapore exchange or interpore diffusion via the gas (or a combination of both). Preliminary experiments at different mixing times indicate that exchange within the liquid crystal is faster than gas to liquid crystal exchange and thus xenon must be exchanging between different environments within a single pore. There are two possible mechanisms for this. If the observed 1D line shape (figure 1.5a) is representative of a single pore, then the xenon may remain bound near the liquid crystal/anopore surface for times around 40 msec and then rapidly diffuse through the pore until binding at the surface where there is a different director orientation. If the distribution comes from different pores, then the average environment experienced by the xenon within each pore must be varying on this timescale indicative of some reorientation of the planar polar director structure within the pore.

It would be interesting to do a temperature study of both isotopes in these samples just above the nematic-isotropic transition. Here there is surface induced order in the *isotropic* phase which has been the subject of several detailed investigations [61]. In this system the two isotopes of xenon give two separate experimental observables of the ordering that would be interesting to compare to theoretical predictions.

Further xenon studies in other confined systems would also be interesting. Nucleopore™ membranes have different surface properties from the anopores and thus different director field structures such as planar-bipolar and an escape-twisted [51]. These membranes are also available in a range of diameters allowing systems with different curvature to be investigated. Small spherical droplets of liquid crystal can be trapped within a polymer matrix and display a variety of surface effects [62].

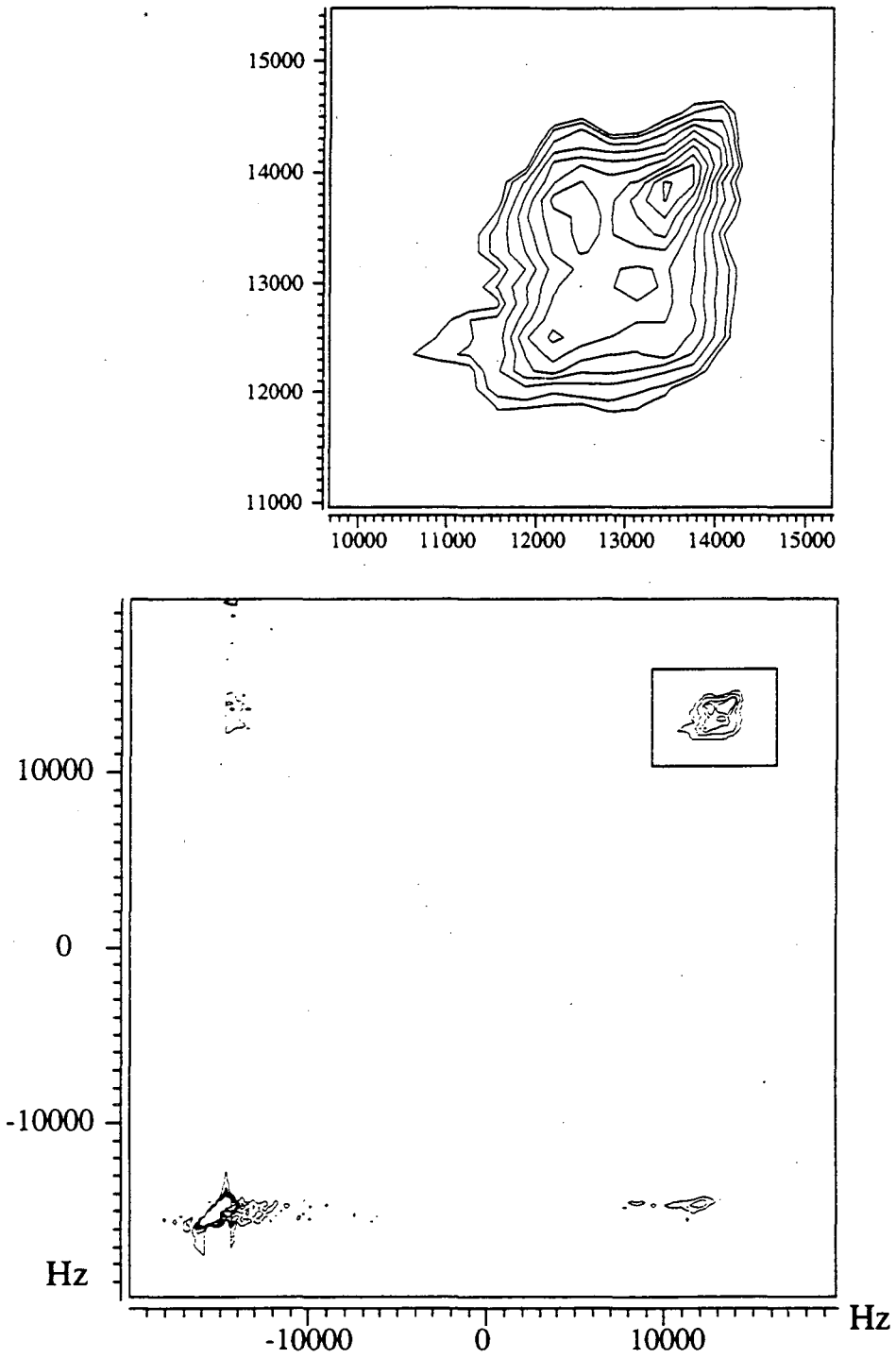

Figure 1.7 2D exchange spectra of xenon in ZLI1132 loaded into anopore membranes at T= 33°C with t_{mix}=200 msec. The upper spectrum is an expansion of the liquid crystal region (boxed).

1.3.2 Xenon Dynamics in NaA Zeolite

Xenon has found widespread use as a probe of zeolites for the past ten years. Zeolites are extremely important as molecular sieves and industrial catalysts used in the cracking of hydrocarbons. Xenon NMR has been shown to be useful in identifying cation sites, guest molecules, estimating cage size, measuring mobility's and diffusion coefficients. The field has been reviewed by several researchers [41, 42].

A particularly interesting example of xenon-zeolite studies is afforded by sodium-A zeolite. In this system the window diameter of the α-cages is approximately 4.2 Å while the xenon is nominally 4.4 Å in diameter. This considerably hinders the xenon adsorption although it is readily accomplished at elevated temperature and pressures. The ^{129}Xe spectrum consists of a series of discrete peaks due to differing numbers of xenon occluded in the zeolite cages [63, 64]. Observation of changes in this distribution as a function of equilibration time show that the xenon can actually diffuse between cages. This slow process can be studied directly with two dimensional exchange NMR to quantify the xenon intercage exchange rates and barriers [65]. Figure 1.8 shows some typical two dimensional spectra taken at various temperatures and mixing times of xenon adsorbed in NaA zeolite at 30 atm and 523 K. From a series of such spectra the motion of the xenon can been quantified in great detail. Taking into account all of the processes that can contribute to the off diagonal intensity, a fit to spectra at variable mix times and constant temperature determines the microscopic rate coefficient, k_n, as a function of the xenon cage occupancy. k_n varies from about 0.1 sec^{-1} for n=1 to 0.8 sec^{-1} for n=7. The rate expressions take an Arrhenius from which the sorption energy at each cage occupancy can be inferred. From variable temperature measurements the activation energy of transport has been estimated to be 60 kJ/mol.

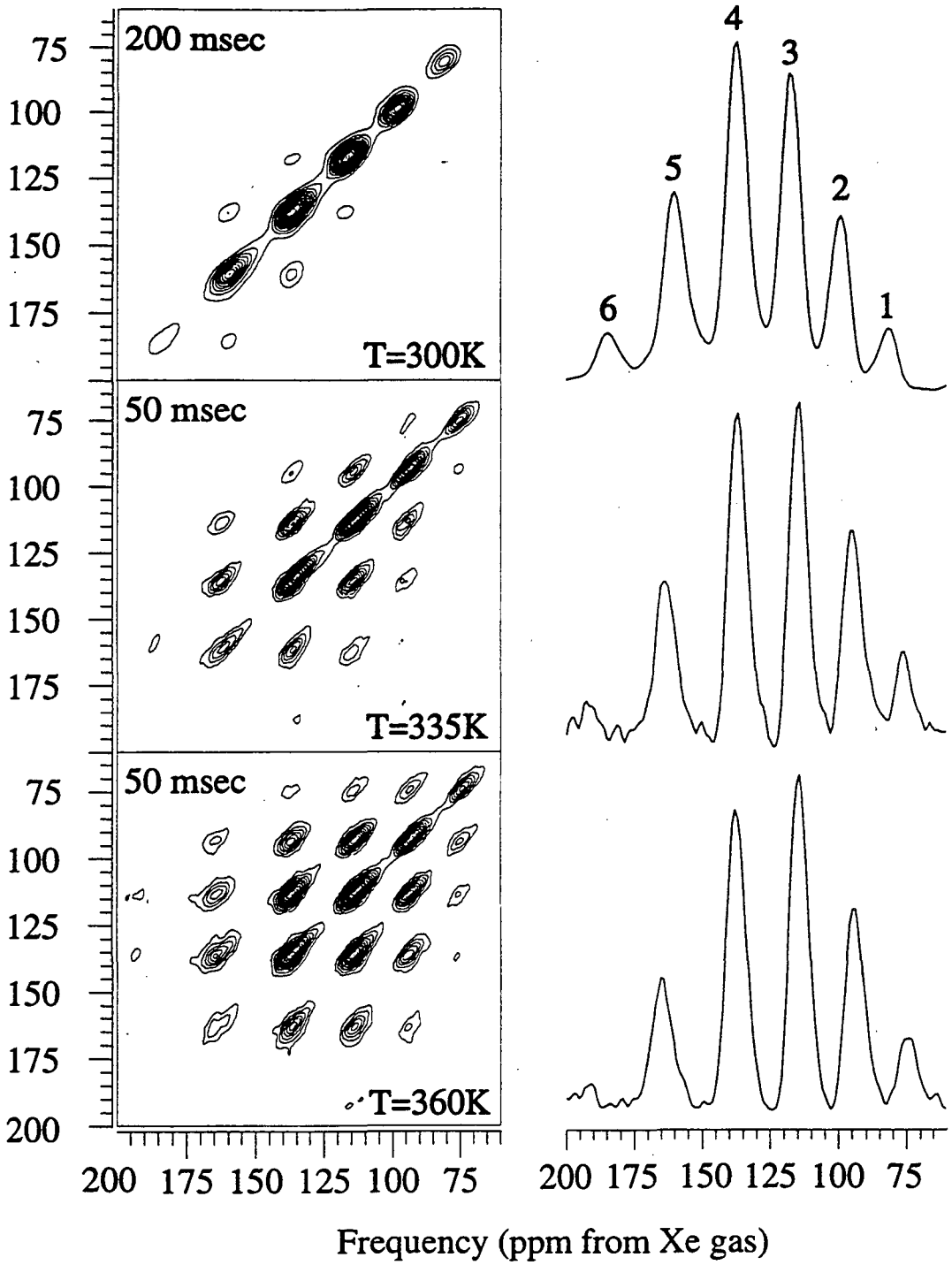

Figure 1.8 2D exchange spectra of xenon in NaA zeolite.

CHAPTER 2 Low Field Experiments

Optical pumping has had a long and illustrious history in atomic physics. First proposed by Alfred Kastler in 1949 [66], the basic idea of "optique pompage" is the transfer of angular momentum from polarized resonance light to an atomic system leading to nonthermal population distributions. Following the first successful observations of these population imbalances in the early fifties [67, 68], this technique has led to many important applications. These include precision measurements of atomic hyperfine structure [69], magnetic moments, atom-atom and atom-light interactions [70], as well as the construction of masers [71], magnetometers [72], and frequency standards [73]. One of the most important extensions of the original experiment was the discovery of spin-exchange. In a brilliant early experiment, Dehmelt optically pumped sodium atoms in the presence of free electrons that subsequently became polarized. This effect allowed him to make a high precision measurement of the anomalous g-factor of the electron [74]. Purcell and Field invoked spin-exchange to explain thermalization of interstellar hydrogen in order to quantify observations of the 21 cm line (ground state hyperfine transition) in radio astronomy [75].

In the sixties there were several attempts to apply optical pumping techniques to problems of chemical interest, most notably by Bersohn and co-workers [76]. These experiments, however, were not very successful due to the very short relaxation times induced by most buffer gases, especially those with permanent dipole moments [77]. A

very good introduction to this work (and optical pumping in general) is the book by Bernheim [78] which contains a selection of reprints up to 1965.

In 1978 renewed interest arose in spin-exchange optical pumping due to the unexpected discovery of high xenon nuclear spin polarization in rubidium pumping cells being used as a magnetometer [79]. The initial work of the group at Litton Industries was followed up in great detail by the studies of Happer and co-workers at Princeton [80, 81]. The first section of this chapter will briefly recount their work on spin-exchange optical pumping of noble gas atoms. Low field optically detected NMR of xenon will then be described emphasizing new multiple-pulse techniques that may have applications to the many types of high resolution experiments involving these systems.

2.1 Spin-Exchange Optical Pumping of Noble Gas Atoms

A full quantum theory of optical pumping has been given by Barat and Cohen-Tannoudji [82, 83], here only a very simple overview will be given. Full details regarding the theory and practice of optical pumping can be found in many excellent review articles. Early reviews include those by Kastler [84] and Carver [85] as well as Kastler's 1966 Nobel Prize lecture [86]. An article with many useful experimental facts is [87]. Happer's authoritative review [88] is a good reference on theoretical issues related to optical pumping and contains a complete listing of the literature up to 1972. Balling has written a very lucid review [89] that is particularly strong for its density matrix treatment of spin-exchange and discussion of many experimental details. A pedagogical treatment of the subject is given by Happer in [90].

2.1.1 Basics

The essential idea is presented most easily in terms of a hypothetical alkali atom without nuclear spin (and thus no hyperfine structure) that has the energy level diagram shown in figure 2.1a. The ground state is denoted by the term symbol $^2S_{1/2}$ and the first

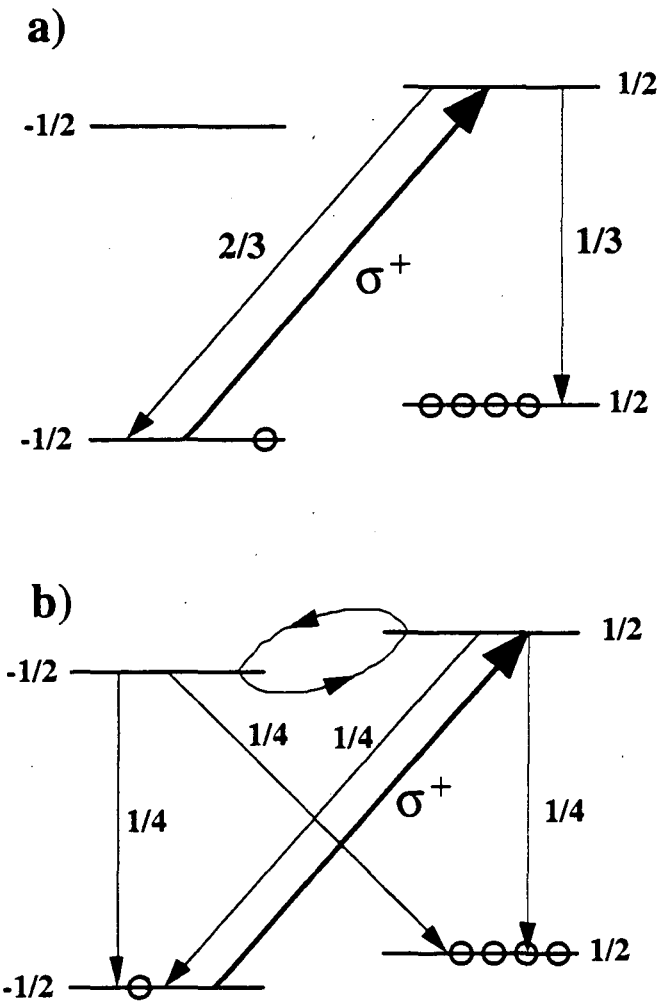

Figure 2.1 (a) Simplified energy level diagram for an alkali metal atom in a magnetic field. The states are labeled by the z-component of the total electronic angular momentum (J_z), and the transitions are labeled by their relative probabilities.

(b) Optical pumping dynamics when there is complete excited state mixing.

excited state by $^2P_{1/2}$ [91]. (The fine structure due to the spin-orbit coupling can be entirely neglected since it leads to a splitting of about 15nm for Rb and the $^2P_{3/2}$ state is thus completely out of resonance.) These levels are connected by the D_1 transition and split by the presence of a magnetic field. In an optical pumping experiment the atoms are illuminated by circularly polarized resonance light propagating along the magnetic field direction. The dark arrow in figure 2.1 shows the electronic transition excited by this light that has the selection rule for $\Delta m=+1$, since only atoms in the -1/2 magnetic substate can absorb the angular momentum of the photon. The exact branching ratio for spontaneous emission can be calculated from the appropriate Clebsch-Gordan coefficients and the relative rates are indicated in the diagram next to the thin lines. If the atom returns to the m=-1/2 ground state then it can absorb another photon, however, if it returns to the +1/2 ground state it will remain there for the lifetime of that state (which can be many seconds for an S state). After several photons have been absorbed it is increasingly likely that the atom will be left in the +1/2 state. Since the D_1 transition is electric dipole allowed, it has a large absorption cross section, and the angular momentum transfer is extremely efficient. Thus an ensemble of such atoms will be left with level populations far different from those of thermal equilibrium (Boltzmann statistics).

Figure 2.1b shows a more realistic situation for the xenon experiments in this thesis. Here there is rapid excited state mixing due to gas phase collisions with rubidium in the easily disoriented P state. The atom is equally likely to be in either excited state sublevel when it fluoresces (or is nonradiatively de-excited) back to the ground state. In this somewhat idealized picture it takes an average of only one photon to polarize an atom.

The real energy level structure of rubidium is shown in figure 2.2b. This diagram shows the hyperfine structure of both ^{85}Rb (I=5/2; natural abundance 72.2%) and ^{87}Rb (I=3/2; natural abundance 27.8%). This makes the spectrum (figure 2.2a) more complex but, with >100 torr of xenon in the pumping cell, pressure broadening leaves a single

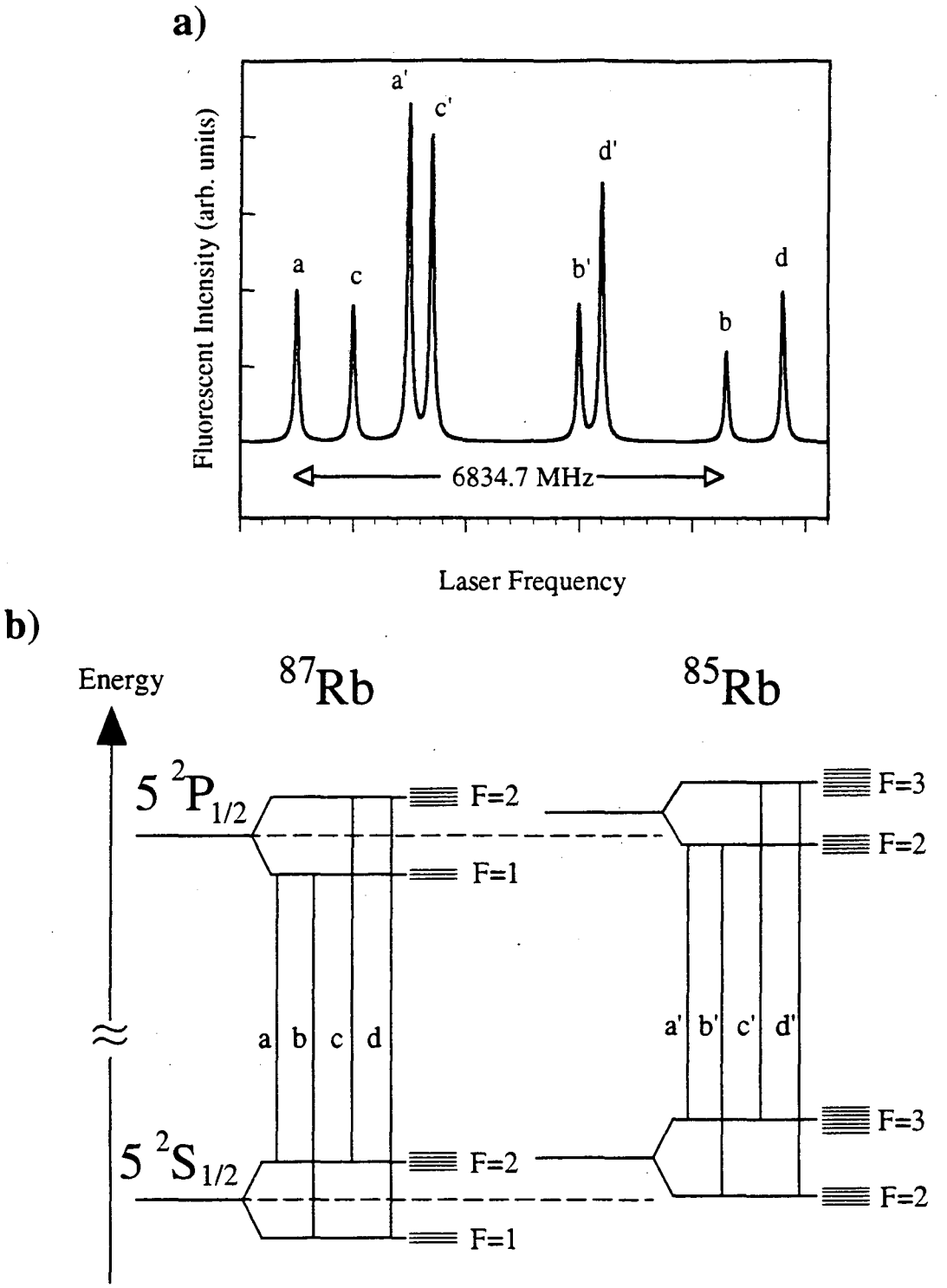

Figure 2.2 (a) Fluorescence spectrum of natural abundance rubidium obtained in as atomic beam (adapted from reference [92]). (b) Energy level diagram of rubidium isotopes with all the hyperfine transitions identified.

featureless absorption. The level multiplicity leads to a somewhat slower optical pumping rate since one needs (2F+1)/2 photons to polarize one atom under ideal conditions (with complete excited state mixing) but the essentials remain the same.

The most important advance in the range of applicability of optical pumping was spin-exchange, which can polarize species that cannot be pumped directly. Many interesting phenomena have been studied using this technique which is discussed in [93]. Spin-exchange between rubidium and xenon occurs during collisions between the two species in the pumping cell and results in xenon nuclear spin polarization [4]. A microscopic (molecular level) explanation of this is given followed by a macroscopic (thermodynamic) discussion.

2.1.2 Microscopic Picture

Happer and co-workers have found that short lived van der Waals molecules are important in the spin-exchange mechanism. In the presence of a buffer gas three body collisions can lead to a van der Waals complex forming between rubidium and the xenon that is particularly effective for spin-exchange due to the extended lifetime compared to a binary collision. The existence of these molecules had actually been inferred years before from relaxation measurements [94, 95]. A schematic diagram of the angular momenta involved in these complexes is shown in figure 2.3. The following Hamiltonian has been successfully used to explain all observed phenomena in this system [96]:

$$H = A\vec{I}\cdot\vec{S} + \gamma\vec{N}\cdot\vec{S} + \alpha\vec{K}\cdot\vec{S} \tag{2.1}$$

In this equation A is the isotropic hyperfine interaction between the Rb electron spin (S) and Rb nuclear spin (I), γ is the spin-rotation constant for the complex, and α is the isotropic hyperfine interaction between the rubidium electron spin and the nuclear spin of xenon (K). This "Fermi contact" term can be expanded in a spherical basis and written as

$$\alpha K\cdot S = \tfrac{8\pi}{3}\gamma_e\gamma_{Xe}|\Psi(0)|^2\Big[K_Z S_Z + \tfrac{1}{2}\underbrace{\big(K_+S_- + K_-S_+\big)}_{\text{exchange terms}}\Big]. \tag{2.2}$$

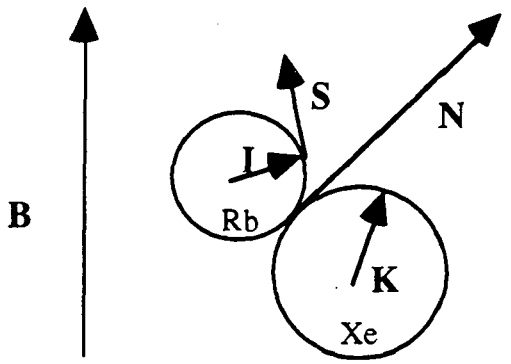

Figure 2.3 Schematic of a Rb-Xe van der Waals molecule with the various angular momenta labeled. N represents the rotational angular momentum of the complex.

The exchange terms, which lead to polarization transfer from rubidium to xenon, are explicitly identified in equation (2.2). The exchange depends on the probability for finding unpaired electron spin density at the xenon nucleus, denoted $|\Psi(0)|^2$. It is thought that this term is particularly large for xenon due to polarization of the xenon core electron shells during a collision [97, 98]. The polarization not transferred to the xenon is lost to the rotational angular momentum of the complex, $\vec{N}$, which is subsequently dissipated as translational energy when the complex is broken up in another collision. The van der Waals mechanism for spin-exchange is dominant when the collision limited lifetime of the complex is long and the magnetic field strengths <100 Gauss,. In higher field and/or at higher gas pressures, binary collisions become the dominant mechanism for spin-exchange [99].

This technique has been used to polarize the noble gas atoms, ^{3}He [100], ^{21}Ne [101], ^{83}Kr [102, 103] and the two xenon isotopes (as well as xenon in an excited nuclear state, ^{133m}Xe, possessing spin 5/2 [104]). Since only ^{3}He could be polarized easily by

other methods before the introduction of the spin-exchange technique, there has been a great deal of interest in the new experimental possibilities that have been created.

2.1.3 Macroscopic Picture

A macroscopic view of spin-exchange is important for developing an intuition about the process and deriving simple rate equations to describe it. Happer *et al.* have used an electrical network model in this regard [81]; here a simple thermodynamic model is employed, analogous to its use in solid state NMR [13, 29]. The spin systems are represented as thermal reservoirs and the various couplings provide contact between them. A simple picture is shown in figure 2.4. Basically the light pumps the Rb system so rapidly (T_{pump} << all other times) that it can be regarded as fixing the spin temperature of the rubidium at zero K. The angular momentum that is not lost to the lattice (T_1^{Rb} due to wall collisions and spin-rotation interaction) goes over to the xenon system where it is "stored" as the xenon is well insulated from the lattice (the gas phase T_1^{Xe} is very long, approaching 1 hour in coated cells). Simple phenomenological differential equations can be written down to quantify all of the angular momentum transfer. As mentioned above, the rubidium polarization, $\langle Rb \rangle$, can be considered a constant and it can easily be shown that the equilibrium xenon polarization, $\langle Xe \rangle$, is given by

$$\langle Xe \rangle = \frac{\langle Rb \rangle}{1 + T_{ex}/T_1^{Xe}}. \qquad (2.3)$$

Clearly the longer T_1^{Xe} is (or the shorter T_{ex} is) the more nearly that the xenon polarization will equal the rubidium polarization which can approach unity. Augustine and Zilm [105] have shown that the xenon T_1 is longer at high magnetic fields in sealed cells which leads to high polarizations despite the smaller spin-exchange rate. ^{3}He can be pumped with this method primarily due to the extremely long spin-lattice relaxation times (days! [106]) in appropriately constructed (aluminosilicate) cells [100].

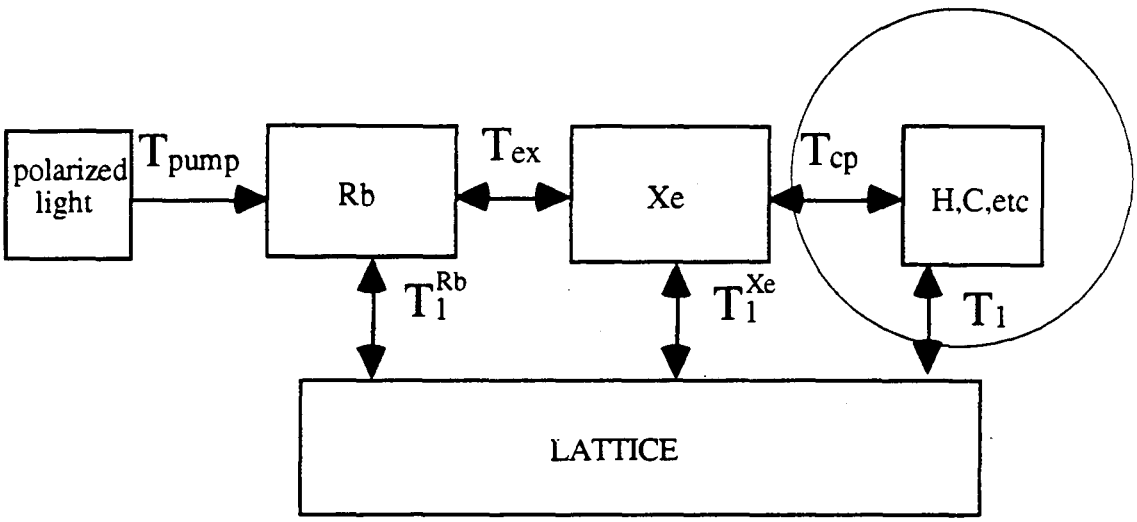

Figure 2.4 Thermodynamic picture of spin-exchange optical pumping.

The possibility for further transfer from xenon to another nuclear spin system is also indicated in figure 2.4; this process is discussed in detail in chapter 5. Also the transfer of angular momentum from xenon to rubidium is shown as a doubleheaded arrow — polarization can flow in either direction. This is exploited in the optical detection of xenon via rubidium discussed in the next section.

2.2 Optically Detected Xenon NMR

Experiments using optical techniques have recently demonstrated substantial enhancements of the xenon NMR signals from low pressure gas samples [96, 107, 108]. The use of spin-exchange optical pumping (to increase the nuclear polarization), combined in some cases with optical detection (to increase the signal detection efficiency), provides orders of magnitude increase in sensitivity. An example of this is

shown in figure 2.5 which shows the optically detected decay of each isotope of xenon sealed in a glass cell with a small amount of rubidium; approximately 2 x 10^{17} nuclei are in each cell. An rf field was applied continuously and periodically swept through resonance to adiabatically invert the xenon magnetization and more clearly show the decay in the presence of baseline drifts.

The optical pumping of ^{129}Xe has been investigated using optical detection methods to observe the effects of the cell surface and temperature on longitudinal (T_1) decay times and elucidate the spin-exchange mechanism. ^{131}Xe is more difficult to study since it has a much lower spin-exchange cross section than ^{129}Xe and the resulting polarization is approximately 16 times smaller [109] (cf. figure 2.5). However, ^{131}Xe NMR is particularly interesting in low field with optical detection since it can be used to probe quadrupolar interactions at the glass surface of the pumping cells. In a spherical cell the *average* quadrupolar coupling due to xenon gas-surface interactions is zero, but in an asymmetric cell, there remains a residual quadrupolar interaction that breaks the degeneracy of the Zeeman transitions in the NMR spectrum. Initial observations of ^{131}Xe quadrupolar splittings of this type were made by Kwon et al [110]. Happer and co-workers have further investigated these effects [111, 112], and, using cells with large well defined asymmetry, they have observed quadrupolar splittings on the order of 100 mHz. Similar methods have been employed in observations of very long gas decays used to search for spatial anisotropies [113, 114] and investigate possible nonlinearities in quantum mechanics [115, 116]. Such experiments typically rely on carefully shielded and stabilized low magnetic fields (about 0.1 gauss or less) in order to prevent dephasing of the observed magnetization due to magnetic field inhomogeneities that would obscure the small quadrupolar splittings.

In this section a low field pulsed NMR apparatus is described that is capable of a variety of experiments designed to remove the effects of magnetic field inhomogeneity. Drawing on the literature of compensated radio frequency pulse sequences and iterative

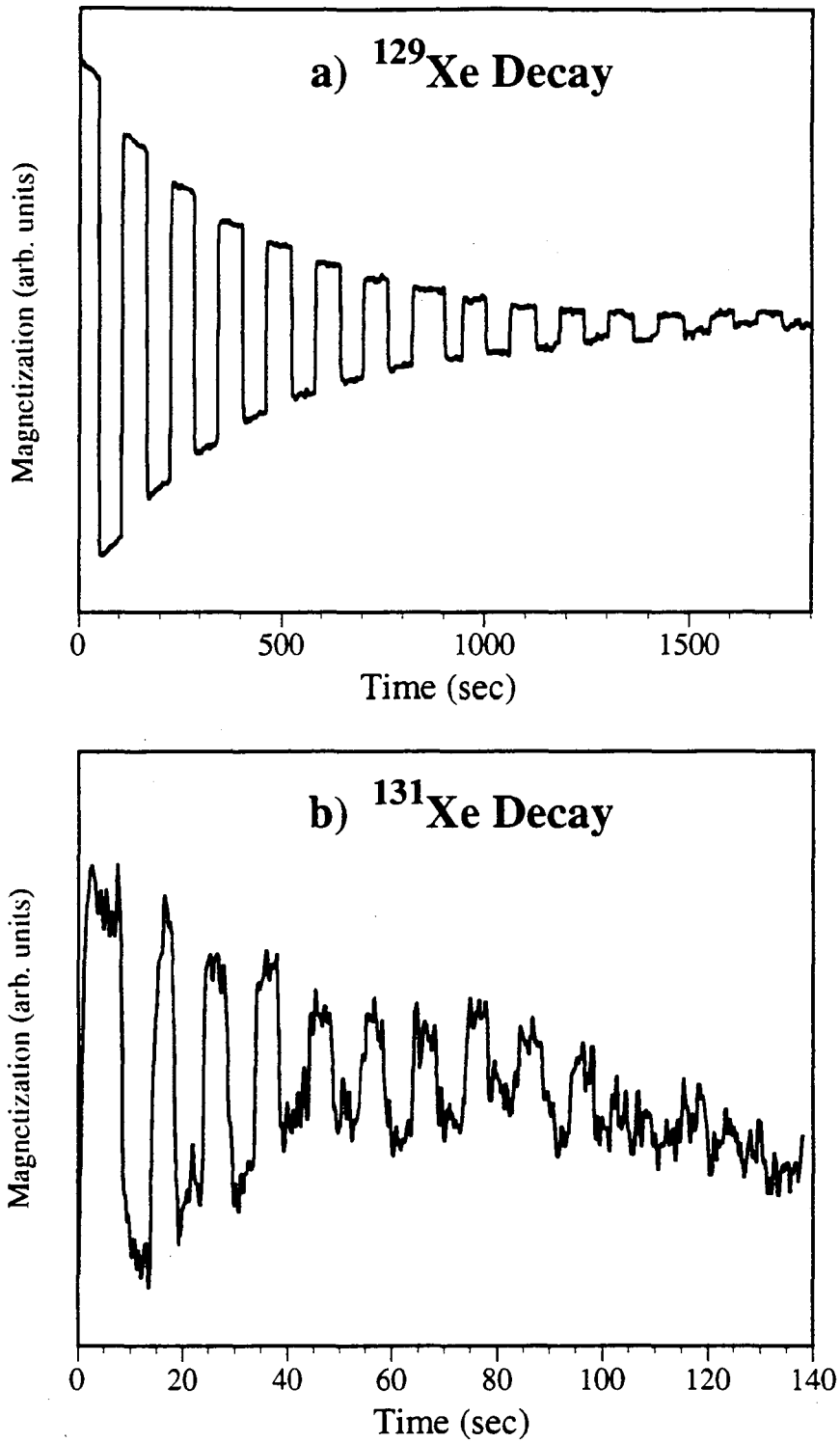

Figure 2.5 Adiabatic rapid passage sweeps show the optically detected T_1 decay of (a) ^{129}Xe (laser power=5mW) and (b) ^{131}Xe (laser power=40mW).

schemes (see [117] and references within), optically detected xenon NMR is observed with high resolution without the need for magnetic field stabilization and shielding characterizing earlier studies. Such pulsed NMR techniques can narrow the line width by more than a factor of 20 facilitating the investigation of surfaces with large quadrupolar interactions with ^{131}Xe.

2.2.1 Theory

A short discussion of the spin relaxation of ^{129}Xe and ^{131}Xe is given. Attention is focused on spin-lattice relaxation without the pumping light present and the dephasing mechanisms relevant in our experiments. The theory of quadrupolar splittings of ^{131}Xe in asymmetric cells is briefly recounted.

Relaxation and Dephasing of Xenon in Rubidium Cells

As discussed in the previous section, the spin-exchange polarization rate, 1/Tpump, of xenon is given by

$$\frac{1}{T_{pump}} = \frac{\Gamma}{2}[Rb]\bar{v}\sigma_{xe}, \tag{2.3}$$

where Γ is the laser pumping rate, [Rb] is the rubidium density, $\bar{v}$ is the relative velocity of the xenon and rubidium atoms and σ_{Xe} is the xenon spin-exchange cross section. The rubidium density is given empirically by [Rb] = 10 exp (23.97-4132/T) [118] (at 65°C [Rb] $\approx 10^{11}$ atom/cm^3).

Happer et al [96] have investigated the rubidium density-dependent relaxation of ^{129}Xe when the pumping light is turned off and found that the relaxation rate, $1/T_1$, may be written

$$\frac{1}{T_1} = [Rb]C + \gamma_{wall} \tag{2.4}$$

where C and γ_{wall} are constants. At temperatures above 100°C, [Rb] is large so that ^{129}Xe relaxation is caused primarily by spin-exchange collisions with rubidium and the T_1 is reduced to about 5 minutes (and, in the gas phase, $T_2=T_1/2$). Below about 60°C,

where γ_{wall} dominates, collisions with the glass walls, which contain paramagnetic impurities, cause relaxation and the T_1 can approach 30 minutes or more in coated cells.

In contrast to the case of ^{129}Xe, the T_1 for ^{131}Xe becomes short at low temperatures due to quadrupolar relaxation as the xenon spends more time on the surface. Spin-exchange collisions with rubidium do not affect the relaxation rate until one goes to higher temperatures where the roughly exponential increase of rubidium density also shortens the T_1. Thus there should be a minimum in the T_1 described by the following equation:

$$T_1^{-1} = [Rb]C + \gamma e^{2E/kT} + (T_1')^{-1}. \tag{2.5}$$

where T_1' represents all other contributions to the spin-lattice relaxation that are assumed to be only weakly temperature dependent.

Quadrupolar dephasing of nuclei due to surface collisions was discussed by Cohen-Tannoudji [119] in his studies of Hg relaxation in quartz cells. He assumed that the correlation time for the fluctuating electric field gradient was long compared to the sticking time, allowing the overall damping rate to be expressed as

$$T_Q^{-1} = \frac{\tau_C \tau_S}{\tau_S + \tau_V} \overline{\left[e^2 qQ\right]^2}. \tag{2.6}$$

The ratio of the surface sticking time to the total time, $\tau_s/(\tau_s + \tau_v)$ is the probability of finding the xenon at the wall. $\tau_v = V/4Sv$ is the time between collisions and is inversely related to the surface to volume ratio and the atomic velocity, v. Quadrupolar dephasing was not removed by any of the pulse sequences discussed in this chapter, although it is theoretically possible to do so with a sequence of 90° pulses.

The main dephasing mechanism for both isotopes in most of these experiments was magnetic field inhomogeneity. The B_0 homogeneity was approximately 40 ppm resulting in a ^{129}Xe line width of 3 Hz, which would make it very difficult to measure the

small (subhertz) quadrupolar splittings in ^{131}Xe. Hahn spin echoes [120] make it possible to refocus the dephasing of the spins in an inhomogeneous field, but in the presence of gas phase diffusion, dephasing of transverse magnetization can still occur rapidly as described quantitatively by

$$M_{trans}(t) = M_{\circ} e^{-2t/T_2} e^{\frac{2}{3}\gamma^2 (\delta B_z)^2 D t^3}. \qquad (2.7)$$

In the nutation experiments (where the radio frequency field is applied continuously) it is the inhomogeneity of the radiofrequency field that limits the resolution. Such inhomogeneity can be largely alleviated by means of coherent averaging methods and iterative pulse sequences originally developed to increase the tolerance and selectivity of multiple pulse and spin decoupling schemes. It is important to note that these sequences can work without effecting evolution due to bilinear spin interactions such as J-couplings or the quadrupolar interactions of ^{131}Xe.

Surface Induced Quadrupolar Energy Splittings

The spin Hamiltonian for ^{131}Xe atoms in the pumping cells consists of two parts

$$H = -\hbar \gamma H_{\circ} I_z + H_Q. \qquad (2.8)$$

$\gamma H_{\circ} = \omega_{\circ}$ is the Larmor frequency for xenon in the gas phase which is about 17 kHz in our 49 gauss field and H_Q is the quadrupolar term, arising from the interaction of the quadrupolar ^{131}Xe nucleus with the electric field gradients at the surface of the optical pumping cells. Induced distortions of the electron shells can enhance the electric field gradients felt by the nucleus, (the Sternheimer anti-shielding effect [20, 121]). The gradients are enhanced by a factor of 138 for ^{131}Xe [49, 122] which accounts for the high sensitivity of xenon to the field gradients rather than the size of the gradients themselves. In the optical pumping experiments, the electric field gradient is assumed to be axially symmetric ($\eta = 0$) and to point perpendicular to the surface. Due to the short adsorption time of xenon at the surface, the time-averaged quadrupolar interaction is small, so that

$H_Q << H_Z$, and to first order, only the secular part of the quadrupolar Hamiltonian in the laboratory frame has to be considered,

$$H_Q = \frac{e^2 qQ}{4I(2I-1)}\left(3I_z^2 - I^2\right)\tfrac{1}{2}\left(3\cos^2\theta - 1\right). \qquad (2.9)$$

The angular part of equation (2.9) must be averaged over the particular cell geometry used and weighted by the fraction of time spent on the surface. For very thin cylindrical cells the term is inversely proportional to the cell height and the NMR spectrum has a central transition at $\omega_\circ$ plus satellites at $\omega_\circ \pm \omega_Q$.

In a nutation experiment the signal is observed at the nutation frequency, ω_1, and the new Hamiltonian is obtained by transforming equation (2.9) to the rotating frame [20, 29]. The result is that the quadrupolar interaction is modified by a factor $(3\cos^2\beta - 1)/2$ where β is the angle between the axis of nutation and the laboratory z axis. For the on resonance case, which was used exclusively, $\beta = \pi/2$, and the splitting between the satellite transitions is scaled by a factor of 1/2.

2.2.2 Experimental Details

Because of the sensitivity of xenon spectra to cell preparation the construction procedure for our cells is described in detail. The optical pumping and detection apparatus is described and the experimental procedure outlined.

Cell Preparation

Cylindrical cells were constructed using circular Pyrex plates 2 mm thick and 50 mm in diameter, sealed onto the ends of a cylindrical tube. A small glass tube on the side of the cylinder connects to a stopcock with a 1/4" connection to a gas rack. The cells were washed with distilled water and acetone and dried overnight at 90°C in air. In the case of coated cells, such as for the ^{129}Xe experiments, cells were rinsed with cyclohexane, then washed three times with a 10% solution of Surfrasil (dichlorooctamethyltetra siloxane; Pierce Chemical Co., Rockford Ill.) in cyclohexane and finally rinsed with pure cyclohexane to get rid of any unreacted Surfrasil.

The cells were then evacuated at 10^{-5} torr at 120°C overnight. Rubidium metal was placed in the bottom of the stopcock tube in a nitrogen or argon filled glove box and the tube was remounted on the gas rack. A small amount of the rubidium was distilled over to the cell using a gas torch. Cells were filled with a few torr of enriched ^{129}Xe (80% , Isotec Inc.) or ^{131}Xe (70% , EG&G Mound) that was then frozen onto the bottom of the stopcock tube, during which time either pure nitrogen or a 8% hydrogen in nitrogen buffer gas was added. After waiting for the gases to mix [81], the cells were carefully torched off and cured at 120-150°C for a week or more. The curing process has been shown to be important in ^{131}Xe cells [112], and often quadrupolar splittings, or even rubidium absorption, was not observed in uncured cells or cells cured at only 70°C for a week.

Apparatus

A schematic drawing of the experimental apparatus is shown in figure 2.6. The glass sample cells are held in a Plexiglas oven that is heated using hot, flowing nitrogen gas, and feedback controlled to better than 0.1°C. A large solenoid magnet of an over wound design [123] 100 cm long and 30 cm in diameter produced a field of about 49 gauss when driven by a home-built 5 A constant-current power supply with 10 ppm/°C stability. The field homogeneity was corrected by observing the transient NMR signal from a water sample using standard pulsed NMR detection circuitry at 209 kHz. The corrections were made with four coils (X, Y, Z, Z^2) mounted within the magnet which resulted in a homogeneity better than 40 ppm over a 100 cm^3 sample volume.

Radio frequency pulses are applied to the sample using a transmitter controlled by a home-built pulse programmer card in a IBM compatible computer. The pulse programmer consists of 1k × 24 bits of FIFO memory that contains timing and digital word information that is clocked out using an on-board 1 MHz clock. The pulse programmer controls all timing of events in the experiment including opening and closing rf gates, moving the mirror, and triggering the data acquisition. Frequencies of up to 1

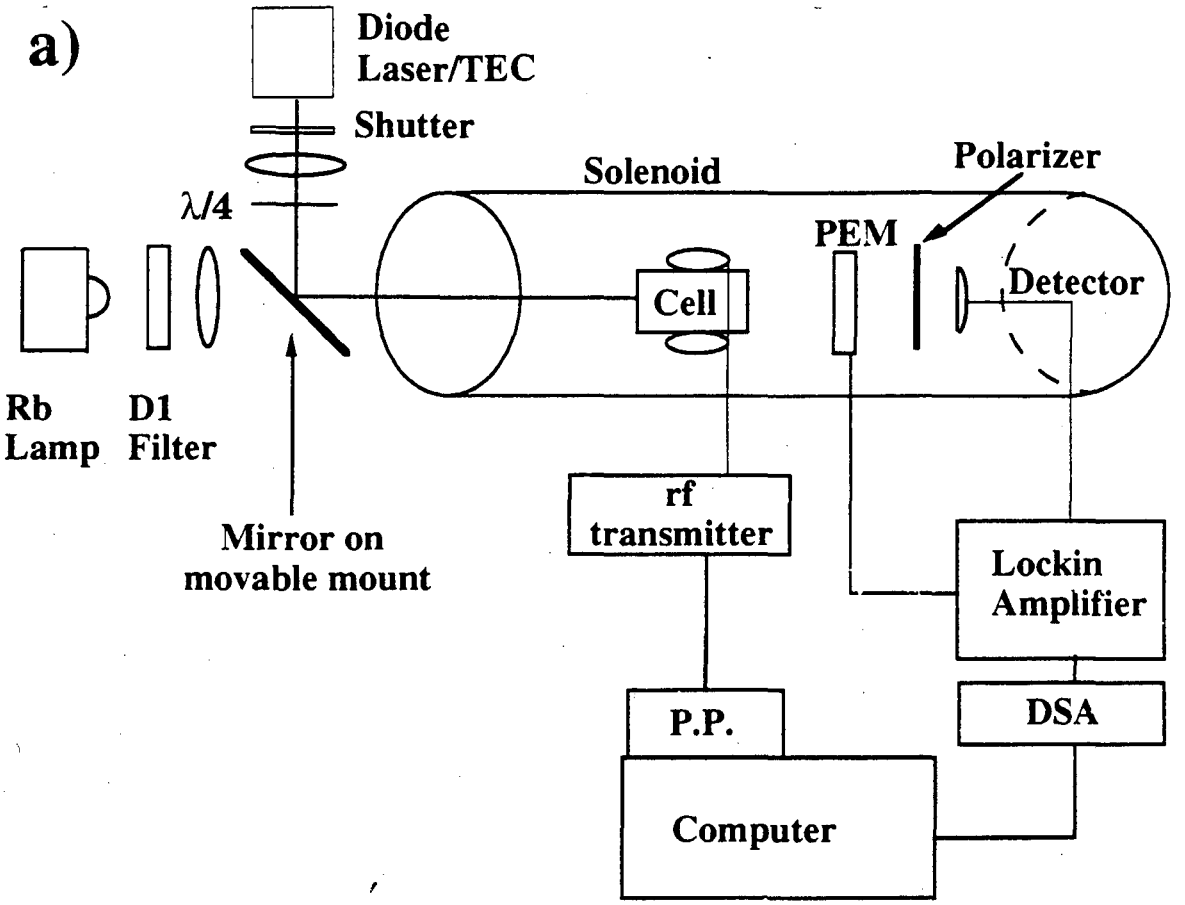

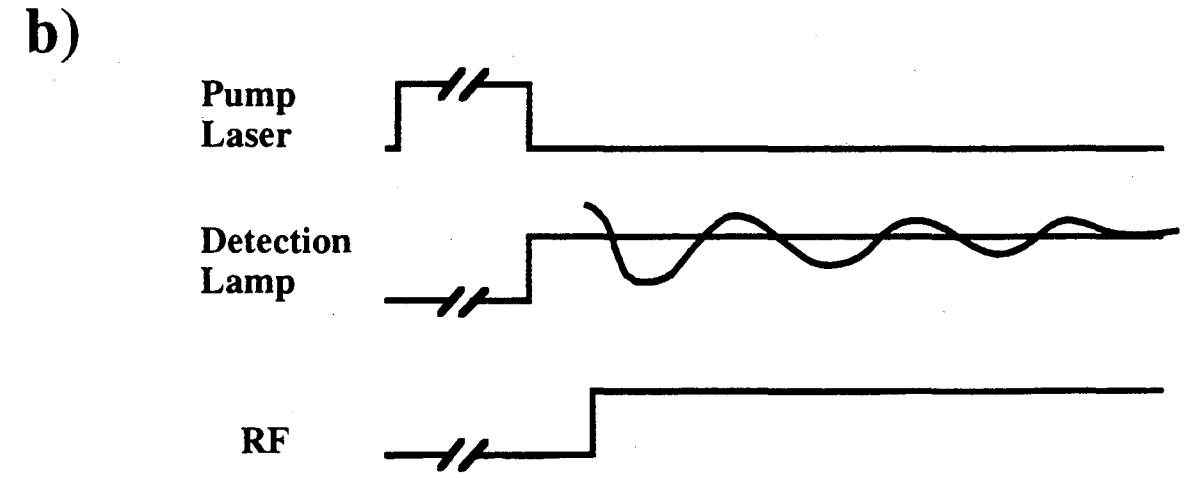

Figure 2.6 (a) Schematic diagram of the low field experimental apparatus as described in the text. P.P. is the pulse programmer, DSA is the Digital Signal Averager. Shim coils and oven are not shown.(b) Timing diagram for the nutation experiments.

MHz are derived from an external frequency synthesizer, and can be gated by the pulse programmer to create rf pulses. A phase shifter produces 0, 90,180 and 270 degree phase-shifted rf pulses using digital flip-flops [124]. The pulses are then filtered, amplified and sent to the tuned rf circuit. Several of our experimental pulse sequences are illustrated in figure 2.7 and discussed in detail in the Results section.

The sample cell is optically pumped using circularly polarized light from a 40 milliwatt Sharp LT016 laser diode laser operating at 794.7 nm. The laser is contained in a vacuum enclosure that is either evacuated or filled with nitrogen to avoid water condensation. The laser wavelength is tuned to the rubidium D_1 absorption line by lowering the temperature to approximately -38°C using thermoelectric coolers. The laser temperature could be controlled to better than 0.01°C using a thermistor and feedback current controller circuit. After pumping the sample for typically two minutes a shutter blocks the laser, the mirror is moved using a stepper motor and the cell is irradiated with unpolarized light from a Rb discharge lamp based on a design by Brewer [125]. This probes the birefringence induced in the rubidium vapor by the polarized xenon system. The polarized portion of the detection light is modulated using a photo-elastic modulator (model PEM080, Hinds International Inc.) and then analyzed with a linear polarizer and detected by a silicon photo-detector. The signal, proportional to $\langle Xe \rangle$, is fed into a lockin amplifier, (Stanford Research 575), whose time constant determines the bandwidth of the experiment, and then digitized using an 8 bit Tektronix DSA602 digital oscilloscope. In the nutation experiments up to 25 accumulations were made to improve the signal-to-noise ratio and offsets due to slow drifts were reduced by reading in the dc value of the polarization from the lockin before acquisition so that it could be removed.

To perform the T_1 measurements on ^{131}Xe the lockin is set to a long time constant and the decay of $\langle I_z \rangle$ probed after pumping. When necessary, the background signal from ^{129}Xe is reduced by applying a gradient rf field at the ^{129}Xe resonance frequency (57 kHz) during the pumping period. In addition, the signal is averaged using

a 2-step phase cycle in which the odd acquisitions are shifted in phase by 180 degrees while the ^{131}Xe magnetization is inverted with an rf pulse prior to acquisition. In this manner, the ^{131}Xe signals are added while the background signals and long-term drift tend to cancel upon successive runs.

2.3 Results and Discussion

A new pointwise acquisition scheme used for ^{129}Xe is described and the results of some typical experiments presented. This technique allows standard NMR pulse experiments to be performed on our apparatus which can only detect the xenon longitudinal magnetization. Compensated nutation sequences are discussed for ^{129}Xe and then ^{131}Xe with emphasis on the results from thin cells. Finally T_1 measurements for ^{131}Xe are mentioned.

2.3.1 Point-by-Point Experiments

Point-by-point acquisition is important in many areas of magnetic resonance including two dimensional NMR [60], zero-field NMR[126, 127], optically-detected ESR [128] and the detection of multiple quantum coherences [129]. In our experiments the evolution of the Zeeman and/or quadrupolar interaction in the transverse direction occurs during the time between two $(\pi / 2)$ rf pulses that initiate and terminate evolution. The evolution time is incremented between successive pump and acquisition cycles of the experiment allowing the time development of the magnetization to be mapped out. In figure 2.7a, the evolution is initiated by a $(\pi / 2)_x$ pulse that converts the z magnetization (enhanced by optical pumping in our case) to x magnetization in the transverse plane. Evolution is later terminated by a $(\pi / 2)_{\bar{x}}$ pulse reconverting the x component of the magnetization in the rotating frame back into z magnetization that is then monitored using optical detection. A $(\pi / 2)_y$ pulse could be used to recover the quadrature component of the magnetization in the rotating frame although this was not necessary in these experiments. Optical detection of the z magnetization is very sensitive in this

experiment because the only time evolution is the very slow T_1 relaxation and thus the lockin time constant can be very long. The magnetization is actually sampled at three points during the experiment, just before the pulse sequence is applied (Mi), just after the pulse sequence (M_f), and after a saturating pulse train is applied to establish a baseline (M_{sat}). The final signal plotted is the relative magnetization, $M(t)=(M_f-M_{sat})/(M_i-M_f)$.

Figures 2.8 and 2.9 show the results from several experiments. The first (Figure 2.8a) is a free induction decay (FID) of ^{129}Xe that shows a decay time of about 0.3 seconds that is caused by the inhomogeneities in the magnetic field (δB_o) inside the pumping cell not averaged by the rapid diffusion of the gas. The second (Figure 2.8b), a Hahn echo sequence showing the characteristic decay due to diffusion in a magnetic field gradient (equation 2.7). In figure 2.9a a Carr-Purcell-Meiboom-Gill (CPMG) sequence [130] was used which is designed to refocus dephasing such as that caused by δB_o, and can be made insensitive to diffusion effects by spacing the refocusing pulses closely together. It shows a much longer decay time that extrapolates to approximately 3 seconds. Here the limitation is due to pulse imperfections and diffusion in the period between the 180° pulses that allow the xenon to dephase well before the rubidium induced T_1 limit. Spin-locking experiments were also performed with this technique (Figure 2.9b), which yielded slightly longer decay times than the CPMG sequences.

These experiments were not optimal for ^{131}Xe, however, because of the limited signal-to-noise ratio resulting from the inferior spin-exchange rate and shorter T_1 as compared to ^{129}Xe [110] as well as our limited laser power (40 mW).

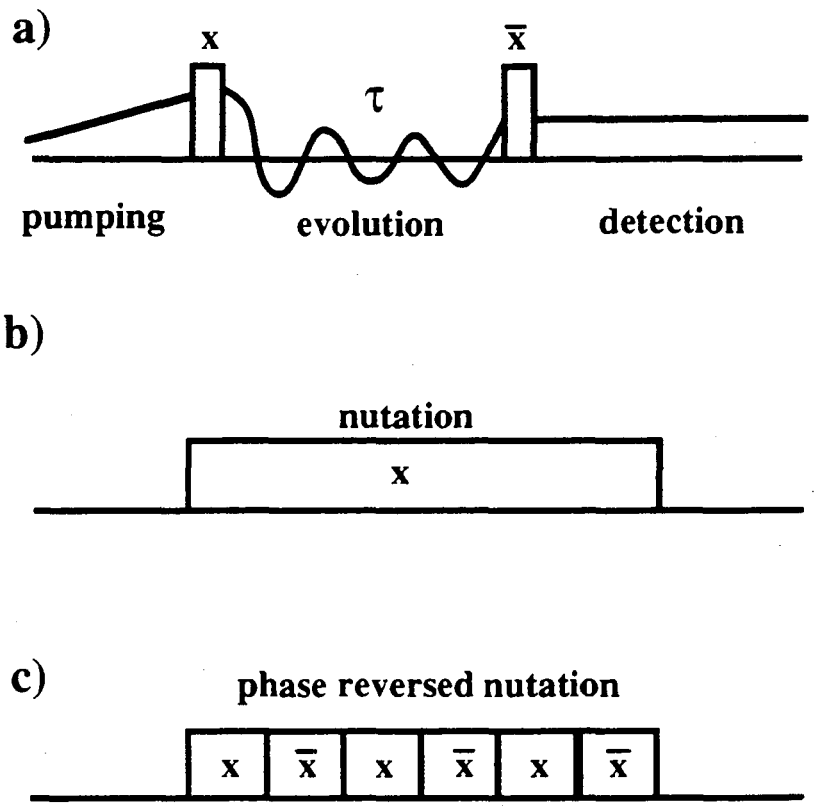

Figure 2.7 Pulse schemes for low field experiments. (a) The point-by-point experiments consist of two $\pi/2$ pulses separated by the desired evolution time τ (during which other pulses may be applied). The nutation experiments consist of either (b) a single long pulse, or (c) an alternating sequence of x and $\bar{x}$ pulses.

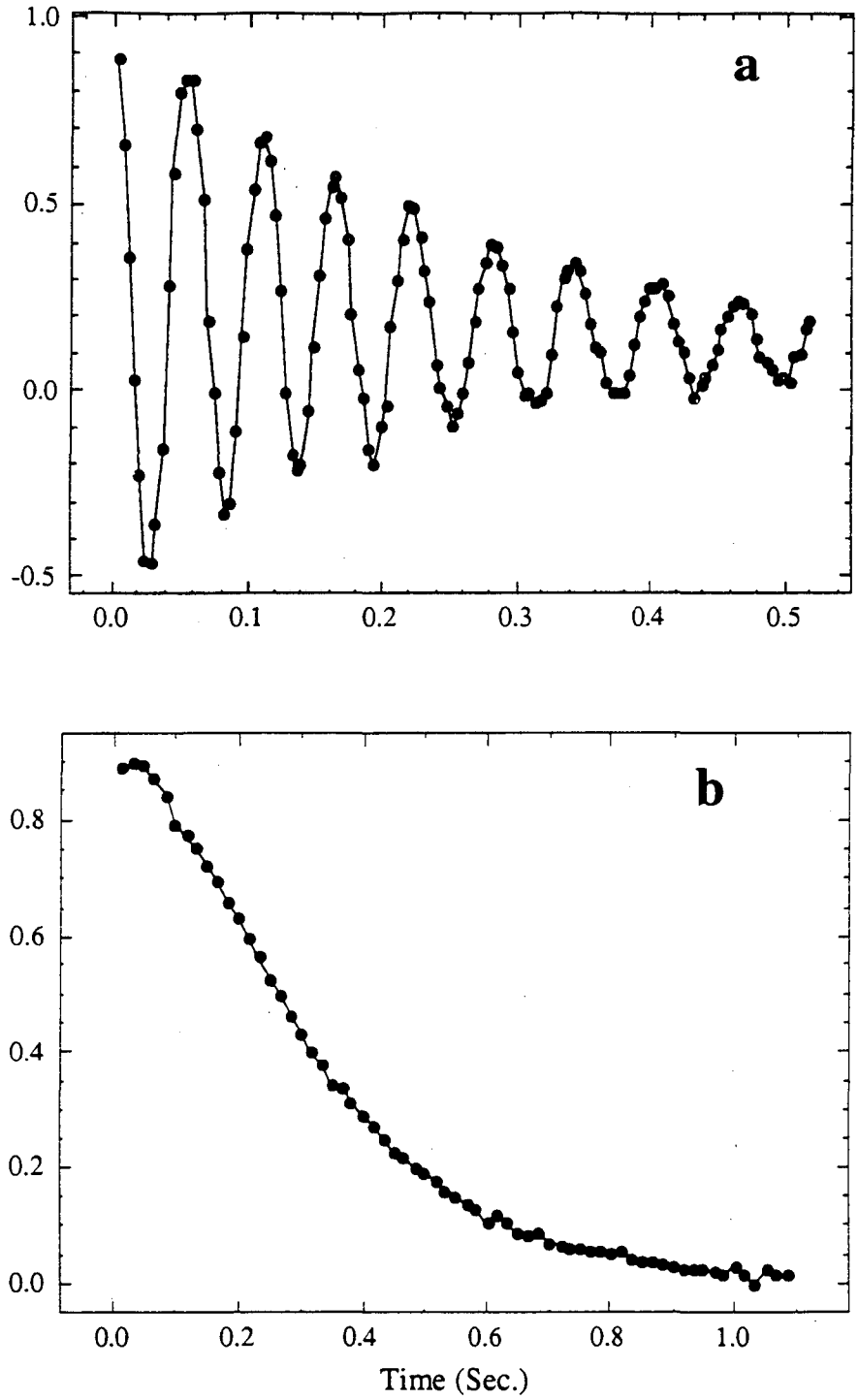

Figure 2.8 Point by point acquisition of optically pumped and detected ^{129}Xe signal. (a) Free induction decay, decay time = 0.3 sec. (b) Hahn echo experiment. Lines connect the points to guide the eye. Vertical scale is relative magnetization.

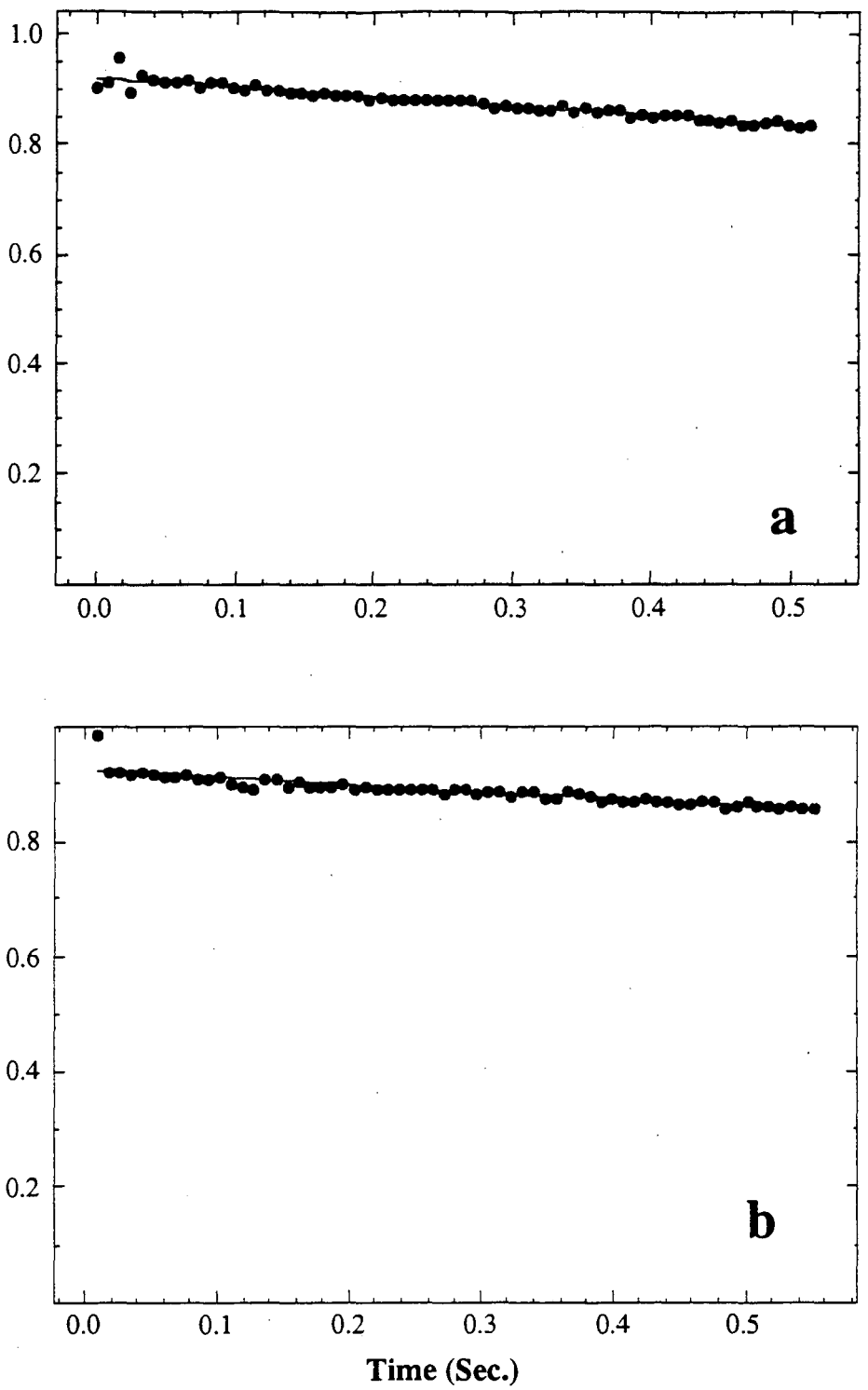

Figure 2.9 Point by point acquisition of optically pumped and detected ^{129}Xe signal. (a) CPMG sequence (see text), decay time = 3 sec. (b) Spin-locking experiment, decay time = 8 sec.

2.3.2 ^{129}Xe Nutation Experiments

Another way to overcome dephasing due to δB_o is a nutation experiment (Figure 2b) with the B_1 (rf) field much stronger than the inhomogeneities. (Although all of the pulses are weak in the sense that the evolution of the xenon magnetization is followed using optical detection during the pulses.) This technique leads to the longer decay ($T_2 \approx$ 1.5 sec.) shown in figure 2.10a, where one is left with the smaller dephasing due to the rf field inhomogeneities δB_1. This can be removed using rotational echoes i.e. reversing the phase of the B_1 field every nutation cycle, or 2π rotation of the xenon magnetization. In principle this can remove the dephasing entirely with rapid enough phase reversals, however this enhanced resolution comes at the expense of signal-to-noise since the lockin amplifier time constant must be set such that

$$\omega_1 << \frac{1}{\tau_{lockin}} \tag{2.10}$$

and thus faster nutation demands a wider bandwidth of the lockin thereby increasing the noise.

Figure 2.10b shows the large improvement one can achieve using the phase-reversed nutation sequence (Fig 2.7c), with a nutation rate of 4 Hz. The decay time increases to approximately 15 seconds and is now dominated by pulse imperfections and residual rf field inhomogeneities not averaged on the timescale of the nutation. Nutation experiments were performed on ^{131}Xe (in symmetrical cells) that decayed at essentially at the $T_1/2$ limit of 50 seconds. Since the rf coils were only being used for excitation there were no constraints involving the filling factor and experiments were done with optimum geometry saddle coils wound on the shim stack that has a diameter of 25 cm. Even with these very large (and therefore very homogeneous) coils it was still advantageous to use the phase reversal technique.

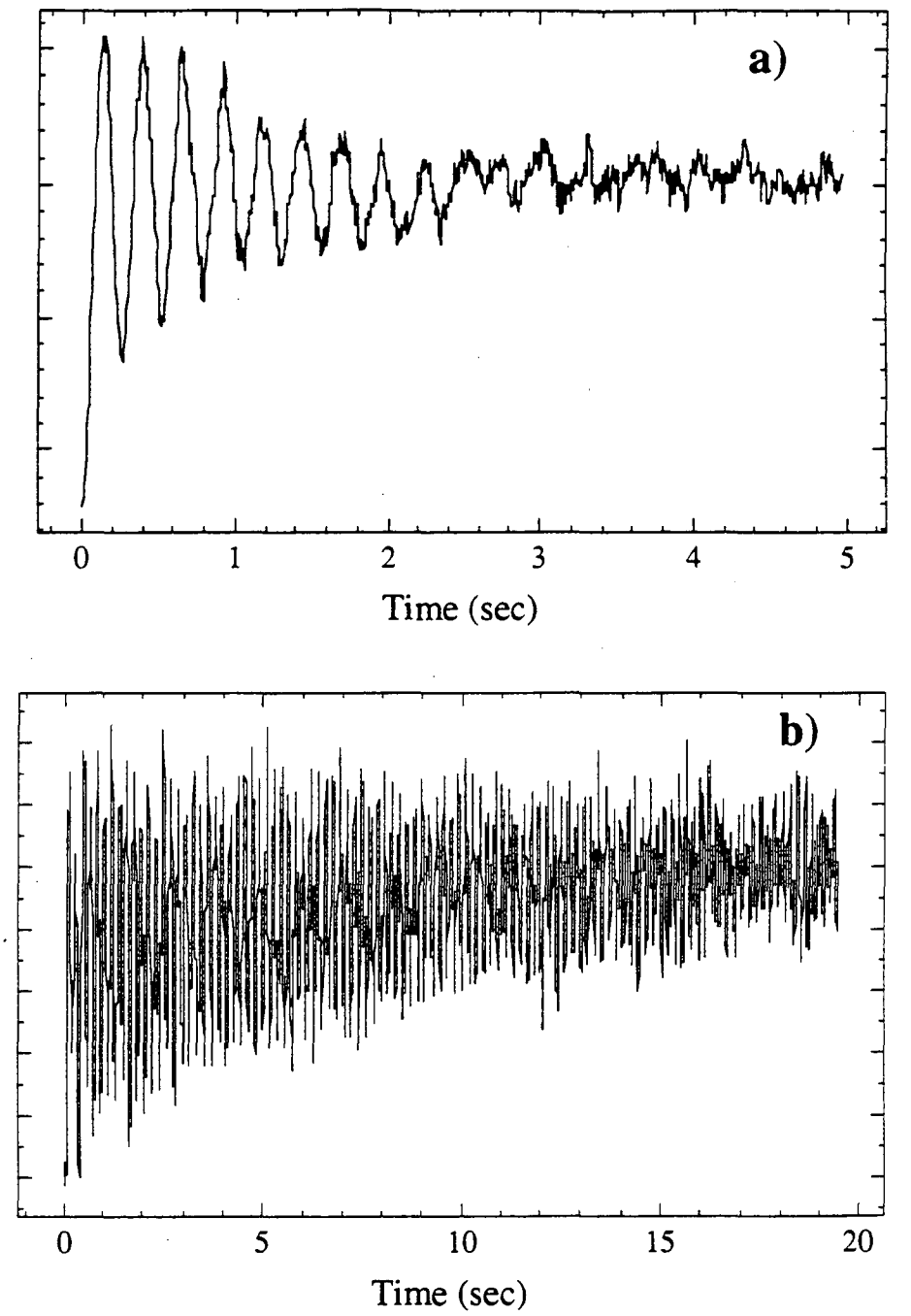

Figure 2.10 Optically-pumped and optically-detected ^{129}Xe nutation experiment. (a) The signal rapidly decays due to magnetic field inhomogeneities. (b) Reversing the rf nutation phase every nutation period refocuses the dephasing and increases the decay time. Notice the different time scales.

Experiments were performed with shorter and longer nutation periods but 360 degrees was found to be optimal. Also, the spectra are more complicated for cycles that are not multiples of 180 degrees due to high frequency harmonics that are introduced by suddenly changing the sign of $\langle I_z \rangle$ which is zero only at 0 and 180 degrees. Higher order corrections to the simple phase-reversed nutation pulse sequence of Figure 2.7c can be made by using standard NMR pulse sequences. For example, the MLEV-16 sequence [131] is an example of an iterated sequence of rotations, R, and phase-reversed rotations, $\overline{R}$ in the following "supercycle",

$$R\overline{R}\overline{R}R \quad \overline{R}R\overline{R}\overline{R} \quad \overline{R}\overline{R}RR \quad R\overline{R}\overline{R}R \tag{2.11}$$

Data from nutation experiments using $R = 2\pi$, 8π rotations and a MLEV-16 sequence all with nutation frequency of about 8 Hz are shown in Figure 2.11 for ^{129}Xe. The more complicated sequences are designed to be insensitive to pulse imperfections, however, from the data, it appears that there is no improvement over simple phase alternation.

2.3.3 ^{131}Xe Nutation Experiments

Figure 2.12 shows the phase reversed nutation data at 120°C for ^{131}Xe in a flat cylindrical cell 3 mm high with added hydrogen. The Fourier transform shows three peaks corresponding to the 3 frequencies of the quadrupole-perturbed Zeeman Hamiltonian [equation (2.8)]. The measured quadrupolar splitting for the hydrogen cell is about three times larger than our results for a bare Pyrex cell, with no added hydrogen under the same experimental conditions. Further experiments are needed to determine the splitting dependence on the cell asymmetry. For bare Pyrex cells the splittings had the predicted inverse dependence on cell height [111]. Splittings comparable to the hydrogen cell were detected in a quartz cell with the same dimensions after extensive (months) curing but the signals were very weak probably due to a short T_1. Quadrupolar splittings of the bare Pyrex cell and cells with added hydrogen were measured at different

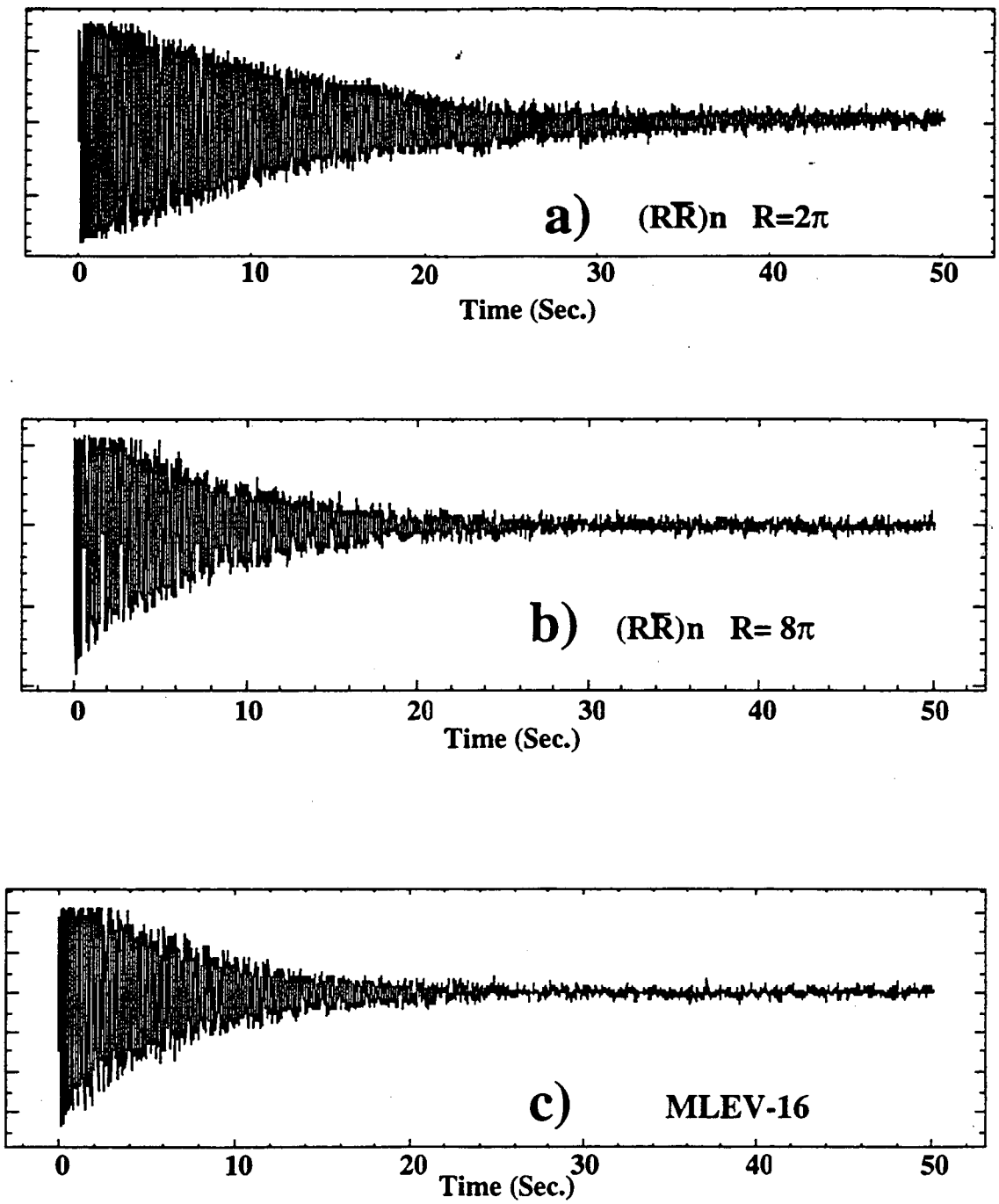

Figure 2.11 (a) Phase reversed nutation at 8 Hz. (b) and (c) Alternative pulse experiments to simple phase reversed nutation. The signals have been slightly clipped by the digitizer.

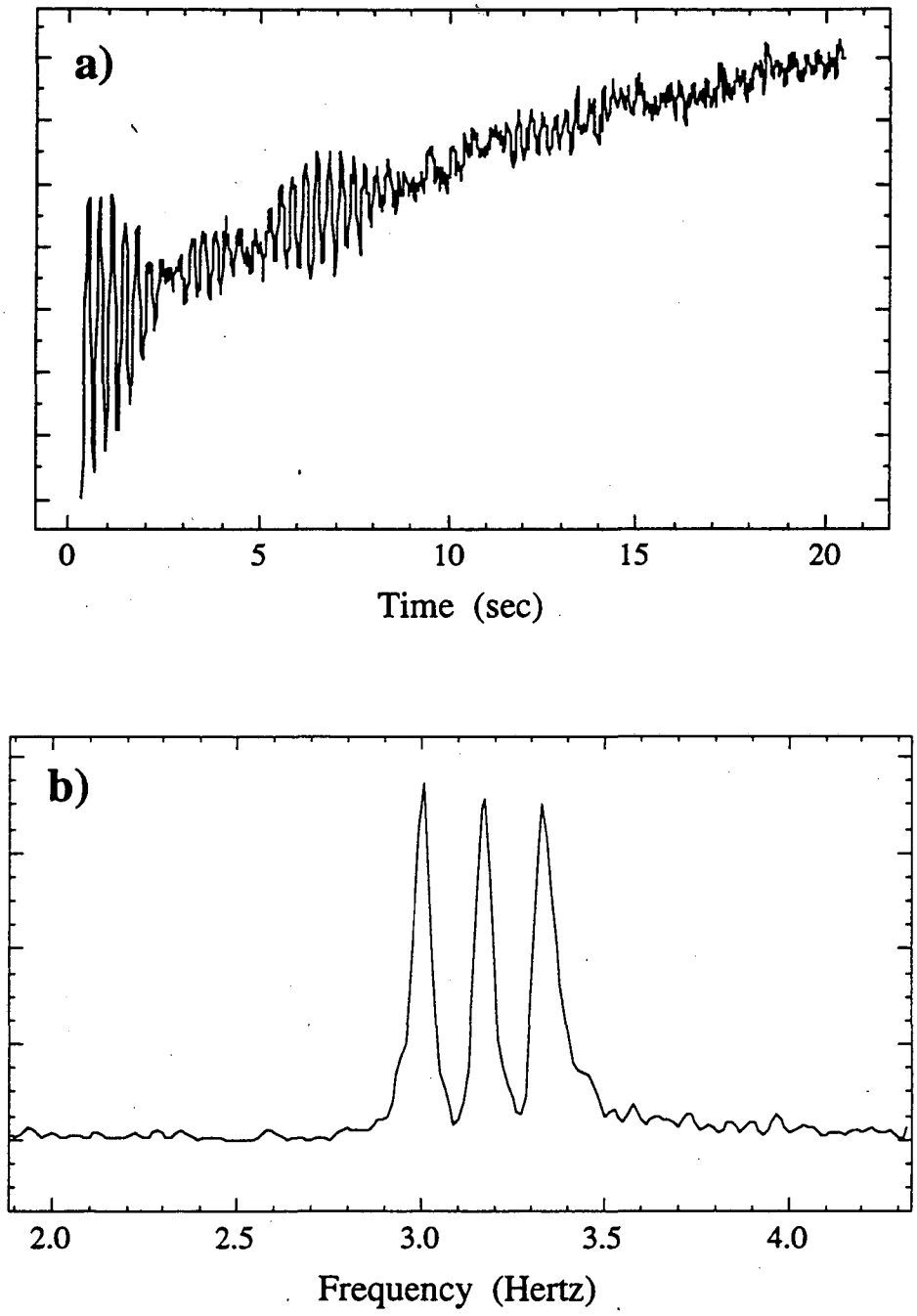

Figure 2.12 (a) ^{131}Xe nutation signal for hydrogen cell 3 mm height and 50 mm diameter at 115°C. ^{129}Xe relaxation causes the background decay. (b) Fourier transformation of (a) shows quadrupolar splitting of 392 mHz.

temperatures, and the data fit to an Arrhenius behavior

$$\omega_Q = \omega_Q^{\circ} e^{-E_a/kT}. \tag{2.12}$$

The activation energies E_a were -0.03 eV for the bare cell, and -0.12 eV for the hydrogen cell, in agreement with results of other workers [110, 112]. The higher activation energy means a longer residence time on the surface that leads to the larger quadrupolar interaction for the hydrogen cells.

2.3.4 T_1 Measurements

Several researchers have reported [110, 112, 132] that H_2 has the effect of lengthening the T_1 of ^{131}Xe in Pyrex glass cells. This probably results from reactions of H_2 with paramagnetic centers (M) on the surface of the glass, including rubidium, to form M-H that reduces the paramagnetic relaxation of xenon at the surface. Nicol [133] reported an increase in the relaxation time for ^{129}Xe in Pyrex cells by adding H_2, although the relaxation time *decreased* in Corning 1720 cells [132]. For ^{129}Xe optical pumping experiments, the largest effect is obtained by coating the cells with Surfrasil which is thought to cause the same shielding mechanism for it also has the effect of substantially lengthening the relaxation time. A typical decay curve and a plot of all the ^{131}Xe T_1 data for a symmetric hydrogen cell is shown in figure 2.13. The fit to the temperature dependence is given by equation (3) and is the same as reported by other workers [134]. Spectra from ^{131}Xe in a Surfrasil coated cell were not observable due to the dramatic reduction in T_1 (<10 sec. [112]).

2.4 Summary

A variety of multiple-pulse experimental schemes were presented in this chapter that are designed to remove the effects of magnetic field inhomogeneities on low field optical pumping experiments. Point-by-point acquisition methods make it possible to implement a wide array of NMR pulse sequences and allow the bandwidths of the

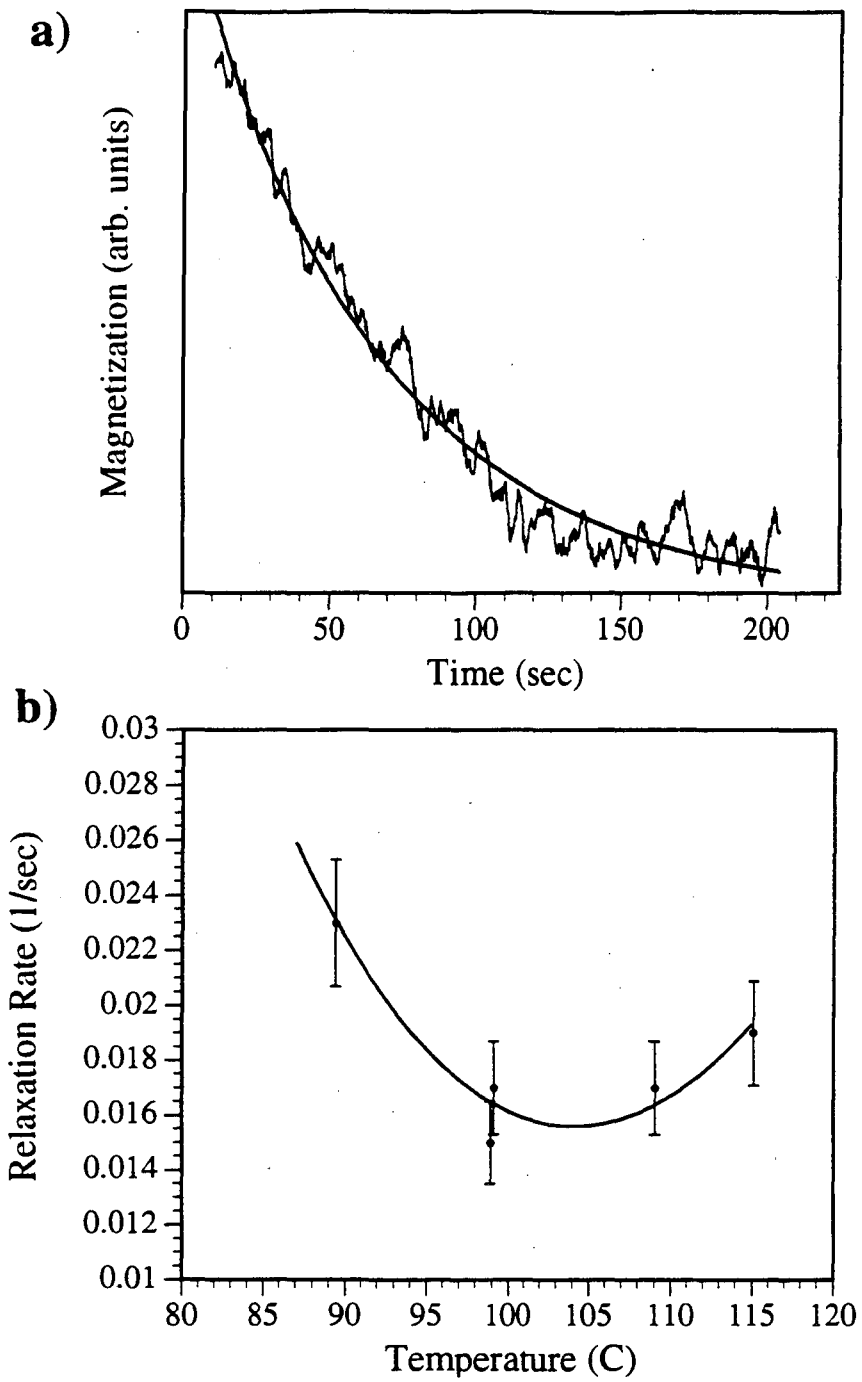

Figure 2.13 (a) Representative T1 decay cure for ^{131}Xe in a hydrogen cell at 99.0°C. (b) T_1 data plotted as a function of temperature and fit to equation (2.5) of the text.

evolution and detection times to be different. Phase-reversed nutation sequences yield much greater resolution than straight nutation experiments. All of the techniques make possible accurate determination of ^{131}Xe quadrupolar interactions at the cell surface. More chemically interesting surfaces may also be investigated with ^{131}Xe and should benefit from these techniques. It should be noted that the nutation experiments that have been used to detect the quadrupolar splittings of ^{131}Xe scale this interaction by a factor of 1/2 on resonance. With point-by-point techniques it should be possible to observe quadrupolar splittings with no scaling as in the nutation experiments, no resonance offset effects, and no magnetic shielding, assuming the signal-to-noise ratio is otherwise sufficient.

Clearly the potential of this technique as a probe of surfaces is severely hampered by the presence of rubidium in the gas phase above the sample. This strictly limits the temperature range that can be investigated and the high chemical reactivity of the alkali metals also posses a great challenge to the surface being investigated. It is partially for these reasons that the separation of xenon from the rubidium was needed to fully exploit its potential as a surface probe. However, to achieve sufficient sensitivity, it was clear that high field NMR detection of the pure xenon was required. The implementation of these ideas is the subject of the next chapter.

CHAPTER 3 Initial High Field Experiments

This chapter describes the experiment involving transport of highly spin polarized xenon to high magnetic field for conventional (Faraday induction) NMR detection. After a description of the NMR probe and the glassware required, a brief discussion is given of possible pump sources. Using a Ti:Sapphire laser (2W) the high field experiment is shown to be capable of producing an enhancement in the xenon gas signal of 54,000 over thermal equilibrium. Various experiments displaying susceptibility effects in solid xenon are discussed in detail. Finally, results of xenon showing adsorption on a wide variety of surfaces is presented showing the strengths and limitations of using spin polarized xenon as a probe of various surfaces.

3.1 Description of the High Field Experiment

The apparatus, shown schematically in Figure 3.1, consists of an optical pumping cell located in the fringe magnetic field (250 gauss) underneath a 4.3 Tesla superconducting magnet and a sample cell located in high field. The two regions are connected by some glassware and are separated by a series of stopcocks. A connection to a vacuum rack allows for evacuation of the sample region, and a pressure gauge permits measurements during the experiment. Natural abundance rubidium is contained in a sidearm connected to

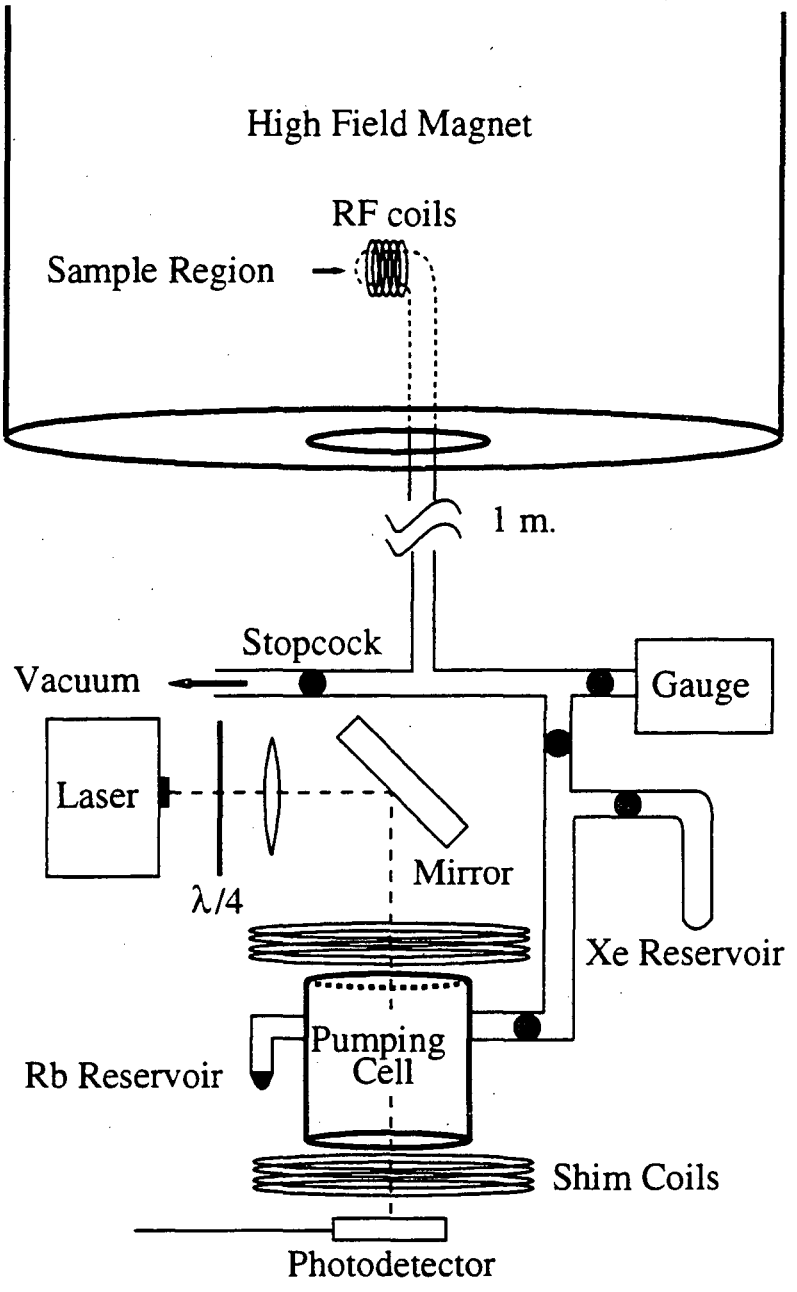

Figure 3.1 Schematic diagram of the high field experimental apparatus. Circularly polarized 794.7 nm laser light is steered through the optical pumping cell. A silicon photo detector is used to detect the rubidium absorption. The oven used to heat the pumping cell, and the nitrogen cooling system for the sample region are not shown.

a pumping cell heated with nitrogen gas. The rubidium is optically pumped to a polarization level approaching 100% using circularly polarized light from either a 40 milliwatt, single-mode semiconductor diode laser (model LT016, Sharp Electronics Corp., Mahwah, NJ) or an argon ion pumped Ti:Sapphire laser (Schwartz Electro-Optics), both operating at 794.7 nm, the rubidium D1 transition. The laser illuminates approximately 2/3 of the cell volume. The absorption is monitored either through the decrease of transmitted light through the cell on resonance or by observing the scattered light through an IR viewer. The entire glass manifold is coated with Surfrasil (Pierce Chemical Co. Rockford, IL) a siliconizing agent that increases the wall-induced relaxation time of ^{129}Xe to greater than 30 minutes as discussed in the previous chapter. The cylindrical optical pumping cell used for most of the optical pumping experiments has a volume of approximately 11 cm^3 and is filled with 60-600 torr of enriched (80%) ^{129}Xe. A Helmholtz pair of shim coils is used in the low pressure experiments to reduce the fringe magnetic field to approximately 50 gauss which has the effect of increasing the spin exchange efficiency. Further details of the pumping region beneath the superconducting magnet are shown in figure 3.2. The experimental procedure followed with this apparatus is outlined in section 4.1.1.

3.1.1 NMR Probe

The NMR probehead (figure 3.3) underwent several stages of modification during the course of these studies and two different probes were built. The sample region consists of the xenon transfer line terminating with a sample cell inside the solenoid coil of a tuned rf circuit. Different glassware configurations are used in the two probes. In the first probe the xenon transfer tube wraps around the coil and has a joint inside the dewar which allows for easy sample changing. At very cold temperatures the xenon has a tendency to freeze out onto the glass tubing walls before reaching the sample and the glass joint within the dewar has a tendency to fail. To compensate for these problems a Teflon enclosure was constructed about the rf coil to limit the coldest part of the dewared region to the immediate sample region. The second probe has a glass joint below the sample region which is

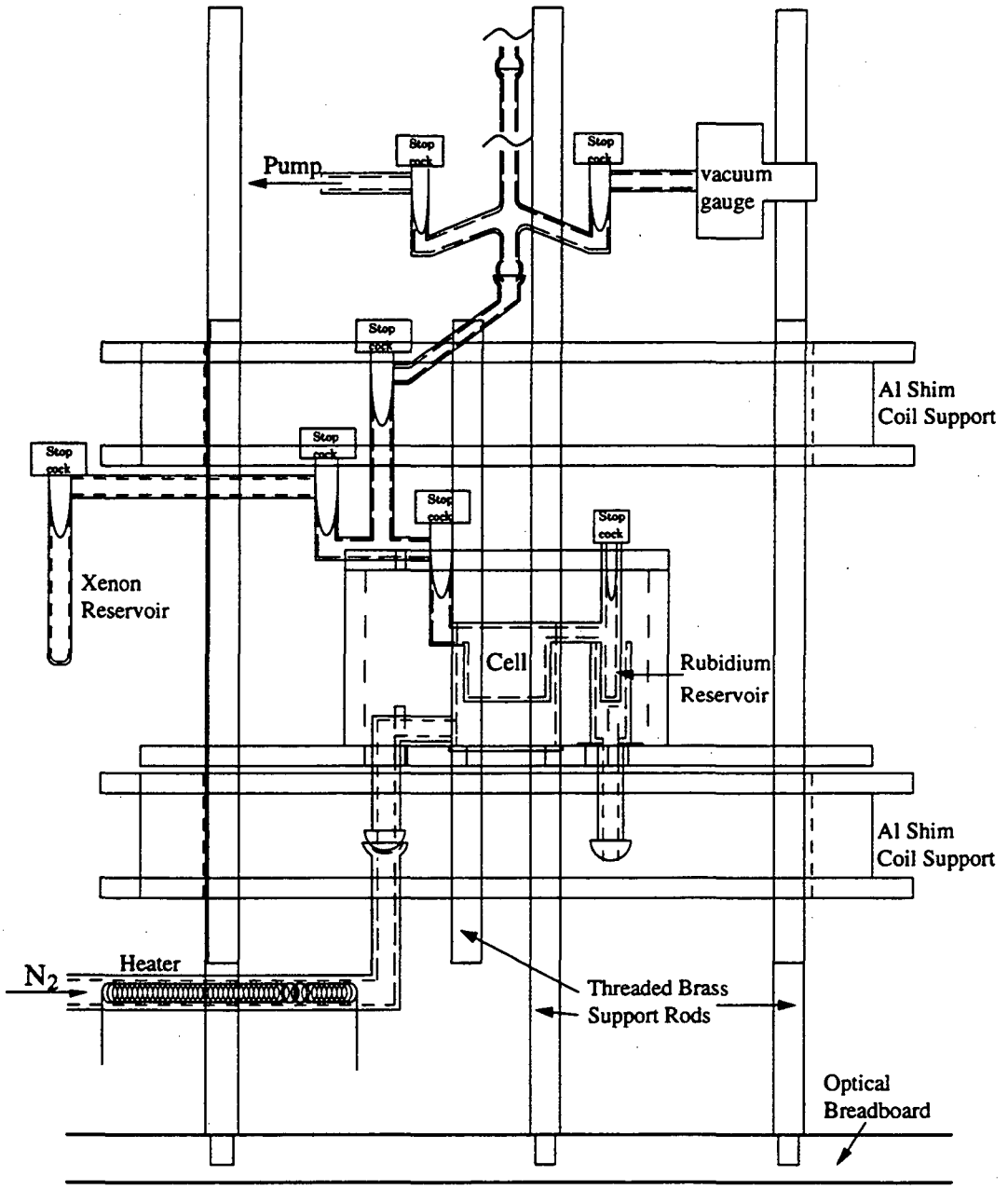

Figure 3.2 Details of the optical pumping setup located below the magnet. The optics for expanding and directing the light beam are not shown.

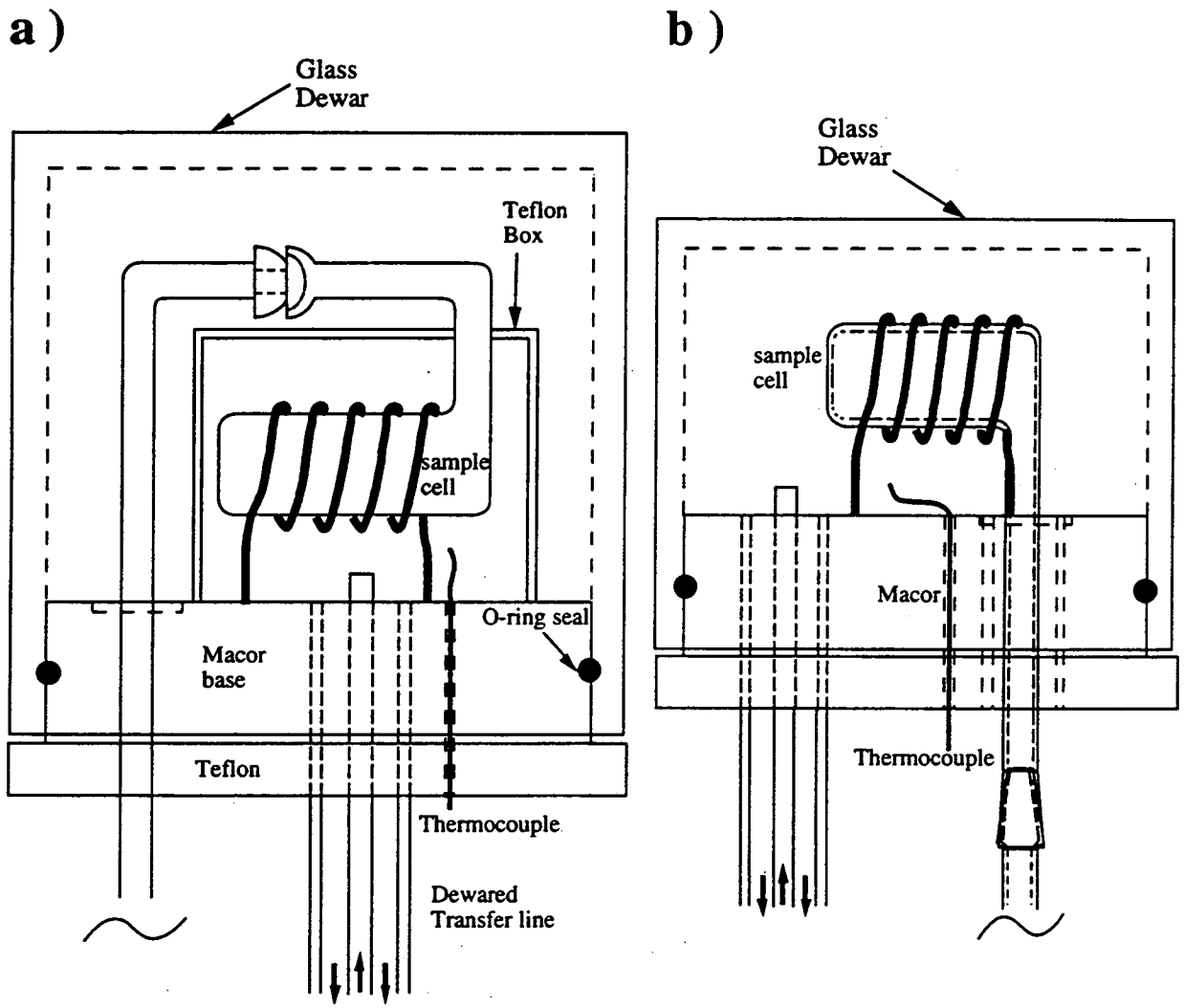

Figure 3.3 Drawing of the sample regions of the probes used for xenon optical pumping experiments in high field. (a) Original 115 mm diameter probe. (b) Standard 89 mm diameter probe.

necessary due to the smaller diameter (89 mm) bore it is designed for. This sample geometry is somewhat inconvenient as the solenoid coil must be unsoldered every time the sample is changed. Both probes are cooled by nitrogen that passes through a heat exchanger and flows up through the center of a dewared stainless steel transfer line. This setup is capable of cooling the sample down to ≈-175°C (98 K). An rf-shielded thermocouple is inserted into the dewar to monitor and control the temperature at the sample. The temperature is maintained constant with an accuracy of ± 1°C using feedback from a commercial temperature controller (Omega). The sample region is insulated by a glass dewar, sealed with a silicon rubber O-ring, and separated from the rest of the probe by a Macor base support. The double resonance rf circuit, based on a design by Doty and co-workers [135], has the advantage of good efficiency at the xenon resonance frequency at 51.4 MHz while allowing for a large sample volume of about 4 cm^3.

3.1.2 Pumping Sources

Two different laser systems were used for the optical pumping experiments. Initially single mode diode lasers (line width ≈20 MHz) were employed as a source of resonant light at 794.7 nm. These lasers have found widespread scientific applications such as in atomic physics [136], as well as many technological applications such as laser printing and (at 5 mW) CD players. Consequently they are mass produced and relatively inexpensive (10 for $800). The diode lasers have several advantages over other lasers being extremely compact and, since they are all solid state, relatively immune to mechanical vibrations. Diode lasers are unique in that they are directly pumped by electrical current, achieving population inversion by electron injection into a cleverly designed heterojunction structure and thus only a constant current source is required to drive them. However, these lasers must be carefully temperature controlled and, as they are only commercially available at 805 nm, must be cooled to about -40°C to tune in the desired frequency range (795 nm). Our diode laser is mounted in a nitrogen filled vacuum enclosure (to avoid condensation) and temperature controlled to within ± 0.01 K using two layers of thermoelectric cooler

elements and temperature controllers (Light Wave Co. Bozeman, MT). It is fine tuned onto the D_1 transition by adjusting the laser drive current. Unfortunately, diode lasers are subject to "mode-hops" — frequency jumps of hundreds of gigahertz — while temperature tuning and thus there are significant gaps in their tuning range. It was found that only about 30-40% of the diode lasers tested could tune stably onto the rubidium transition of interest. Finally, the highest power currently available in single element design is 100 mW, more than an order of magnitude less than what is available from other sources.

Liquid state dye lasers have typically been used for applications requiring tunable, narrow band power in the visible region. The rubidium D_1 transition is far enough in the infra-red that it is beyond the peak power region for most dyes, however, it is exactly at the peak of the gain curve for the Ti:Sapphire solid state dye laser. This is a very homogeneous material that can output high power from 700-1000 nm. A Schwartz Electro-Optics Titan CW is used in a ring configuration with an etalon (line width < 10 MHz). This laser is pumped by a small frame argon ion laser (Innova 310, Coherent Laser Group). With the pump laser putting out 10 watts, 2 watts of power at 795 nm can be obtained. This level of performance demands a fair amount of maintenance in terms of cleaning and alignment, however, even with low maintenance about 800 mW can easily be obtained. Tuning onto the D_1 transition involves coarse tuning of the cavity with a birefringent filter and fine tuning by tilting an intracavity etalon [137]. This laser is also susceptible to "mode-hops", but, due to the longer cavity length, the frequency gaps are only 240 MHz which is less than the Doppler broadening at the temperature used and thus insignificant (cf. figure 2.2). Long term stability is similar to the diode laser, depending on the temperature stability of the cavity [138]. Despite the additional costs and requirements of the Ti:Sapphire system, its performance clearly justifies its use.

It is worth noting that diode laser arrays have recently appeared which combine the high power of the Ti:Sapphire system with some of the advantages of diode lasers. They produce highly divergent and spectrally broad (hundreds of gigahertz) multimode output.

Chupp and co-workers have successfully used these lasers to polarize ^{3}He at high pressures (1-5 atm.) [139]. However, for lower pressures, a narrower bandwidth is desirable and until recently this could only be achieved with a user constructed external optical feedback cavity with an etalon, requiring a delicate optical alignment [140, 141]. This is not a feasible arrangement for xenon optical pumping which demands that the laser rapidly tune to and remain on the transition frequency for the entire pumping period (typically 30 minutes). Very recently however, advances in integrated optics have allowed the construction of *commercial* diode laser arrays that directly output single mode, circular, and diffraction limited light [142]. Although such a laser is not yet available at 800 nm it may become the light source of choice for a dedicated optical pumping system in the future.

3.1.3 Xenon Gas Enhancement

To determine the ^{129}Xe enhancement produced by the apparatus just described, an optically pumped gas signal was directly compared with the signal from a sealed reference sample containing a known number of xenon nuclei (and doped with a small amount of oxygen). In low magnetic field polarimetry [143] or comparison to a large water sample [99] must be used to determine the polarization. The reference was approximately the same volume as the optical pumping sample region and thus the different pressures could be used for a direct comparison. In figure 3.4 one scan of the sealed reference is compared to one scan of optically pumped xenon. The xenon was polarized by 1.3 watts of laser power under optimized conditions (≈25 G field with 44 torr xenon and 70 torr nitrogen, T=83°C). From the ratio of the areas and the known gain/attenuation in the receiver the enhancement is calculated to be 54,000. This translates into a polarization of $\wp = 35\%$; alternatively, using equation (1.3), this can be expressed as a spin temperature of T_S=3mK (the translational degrees of freedom are at ≈300K!). Enhancements obtained under typical, nonoptimized pumping conditions were ≈10,000. By comparison a 40 mW laser diode gives a typical enhancement of 700 [108].

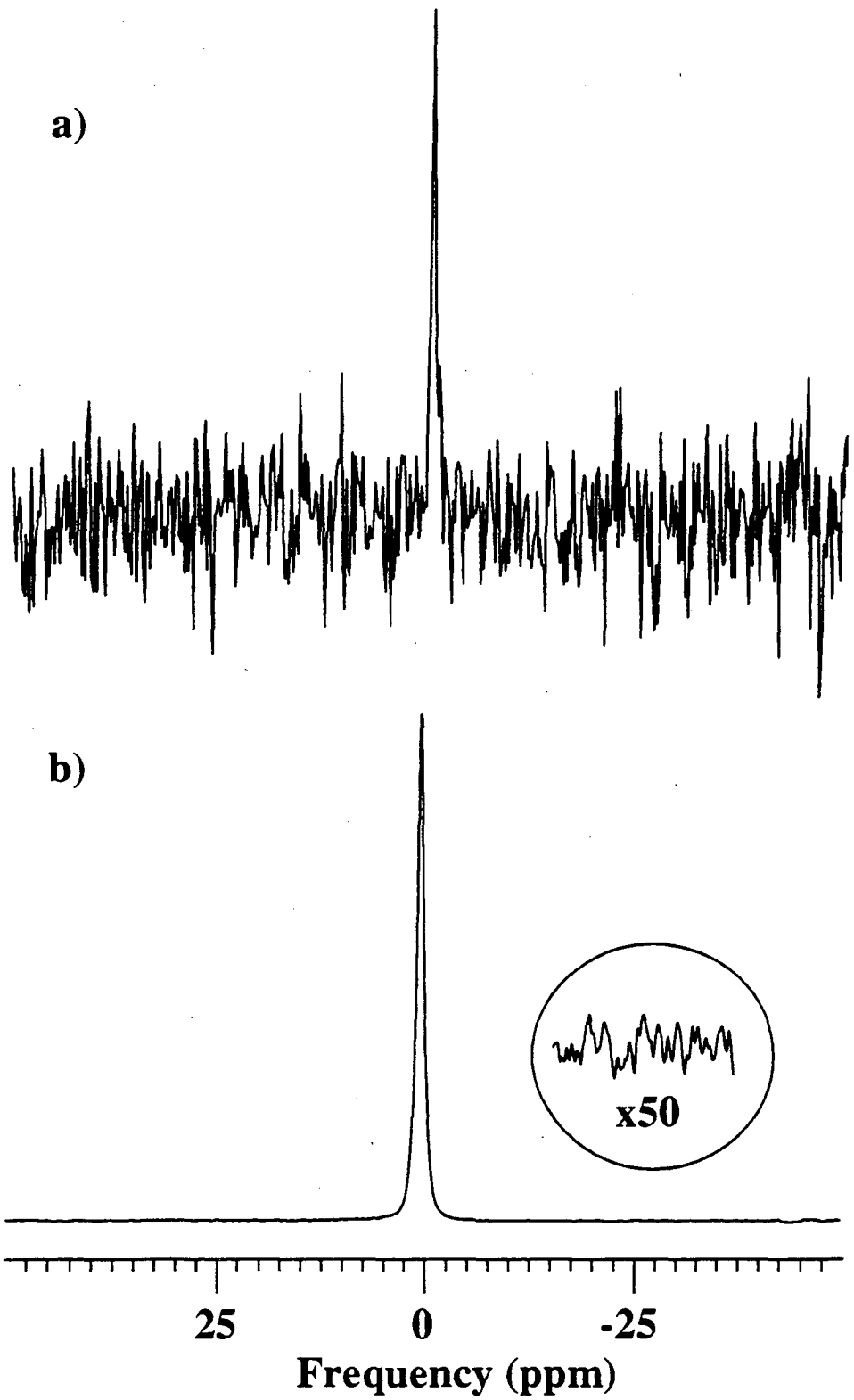

Figure 3.4 Polarization enhancement in xenon gas. (a) Reference sample, 5 x 10^{19} nuclei. S/N=11. (b) Optically polarized spectrum, 2 x 10^{17} nuclei S/N=1300.

3.2 Thin Solid Films [28]

The next step after successfully observing the enhanced gas phase xenon NMR signal was to simply lower the temperature and observe xenon in a condensed phase. The phase diagram for xenon is shown schematically in figure 3.5. The triple point, T_t, occurs at 640 torr and -109 °C, the critical point, T_c, is at 16°C and 56 bar. In the optical pumping experiments the xenon pressure was never high enough to observe the liquid although it could be observed in the sealed reference sample. The liquid has a fairly short T_1 of about 3 seconds. The solid phase was observed along the gas-solid coexistence curve highlighted in figure 3.5 below -118°C for typical pumping pressures (250 torr). Solid xenon was studied by the NMR community in the sixties because of its unusually large temperature dependent chemical shift [144, 145, 146, 147]. The chemical shifts initially measured in our sample cells did not agree with the literature; in fact, one spectra displayed a frequency shift indicative of the solid at ≈20 K [148]!

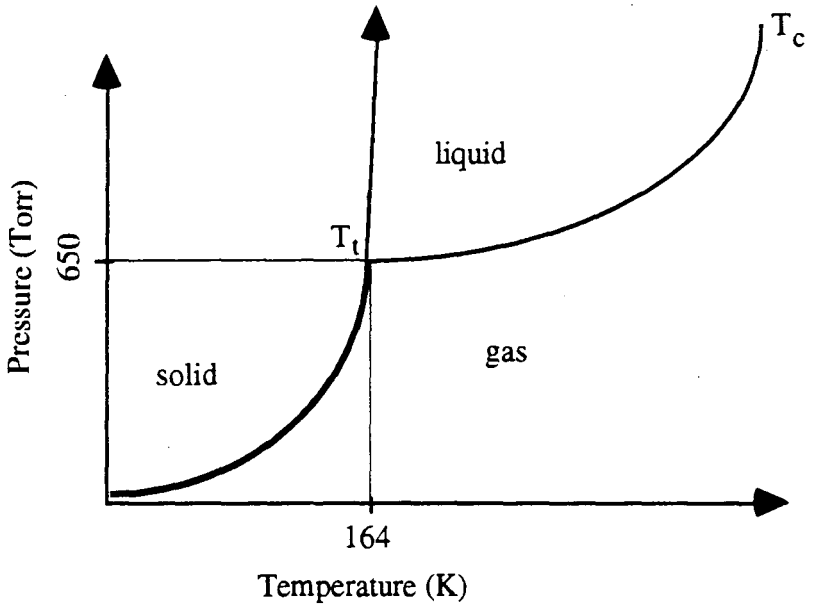

Figure 3.5 Schematic phase diagram of xenon.

The line shape was also not a simple gaussian and was much broader than it should be at higher temperatures where self-diffusion strongly reduces the dipolar line width [148]. These anomalies are explained when the effect of the bulk diamagnetic susceptibility, χ_D, of the solid xenon film geometry is included on the line shape. With this effect taken into account, the spectral line shape and resonance frequency were fully rationalized and brought in agreement with the literature.

Only a few NMR studies of films have been reported [149, 150], and they were performed on high surface-area materials such as graphitized carbon black (Graphon Union Carbide), with a surface area of about 70 m^2/g, or exfoliated graphite (Grafoil). For example, Pettersen and Goodstein attributed the reduction of T_1 relaxation times in thin layers of methane adsorbed on Grafoil [149] to the diffusion of methane molecules to paramagnetic impurities on the surface. They observed some interruption of this mechanism from an intermediate layer of adsorbed xenon. Neue [150] observed three monolayer thick xenon films on Graphon and concluded that diffusion to surface paramagnetic impurities also played an important part in T_1 relaxation. The line shapes were influenced by an inhomogeneous interaction of the xenon film with the large magnetic susceptibility of the graphite.

Thin films of ^3He have been studied by Laloë and co-workers [151] who used optical pumping methods to enhance the polarization of gaseous ^3He which was subsequently condensed at 400mK. Due to interaction of the nucleus with the large, local-dipolar magnetic field of the highly polarized film, the resonance frequency of the film is shifted from that of the gas, depending on its polarization and orientation with respect to the magnetic field. The frequency shift is proportional to $\gamma M_o(3\cos^2\theta - 1)$, where γ is the gyromagnetic ratio, M_0 is the magnetization of the film in Gauss, and θ is the angle between the normal to the film and the static magnetic field.

In this section results are presented on the use of optical pumping to enhance the NMR signal of frozen ^{129}Xe detected in high magnetic field , allowing us to take advantage

of both high sensitivity and high resolution. A variety of effects due to geometry and temperature in thin (≈1 μm) films of xenon are observed that can be understood in terms of bulk diamagnetic susceptibility shifts and motional diffusion in the solid. The observed spectra correspond to model magnetic resonance chemical shift anisotropy (CSA) line shapes observed in powdered solids distributed over 1 or 2 angles of orientation with respect to the magnetic field [29]. In addition to its effects on the spectra of films and bulk samples, bulk diamagnetic susceptibility can play an important role in magnetic resonance imaging experiments where the orientation of otherwise identical structures (e.g. blood vessels) varies and affects the resonance frequencies of those volumes. These shifts have been quantitatively studied in capillary tubes and annular compartments [152].

3.2.1 Theory

The magnetic susceptibility arises from the second-order energy correction for electronic states in a magnetic field, and can be written [22, 153] as

$$\chi = \chi_P + \chi_D = \frac{-e^2}{6mc^2}\sum_i \langle 0|r_i^2|0\rangle + \chi^{HF}. \qquad (3.1)$$

where χ_D and χ_P are the diamagnetic and paramagnetic contributions to the susceptibility, and χ^{HF} are the high frequency terms. In atomic xenon there is no paramagnetic term where, in the usual case, the nucleus is chosen as the origin of the vector potential [22]. The bulk susceptibility is related in form to a more commonly observed resonance shift, the chemical shift, which also has diamagnetic and paramagnetic terms, but whose expectation values are multiplied by a factor of $1/r^3$ [20]. As a result, the chemical shielding is sensitive to shorter-range perturbations of the electron clouds such as chemical bonding.

The susceptibility for a cylindrically-shaped annular sample has been analyzed by Zimmerman and Forster [154]. They considered a sample consisting of concentric layers of materials (sample regions plus glass tubes) with different susceptibilities. The geometry is shown schematically in figure 3.6. The relative change of the magnetic field in a sample

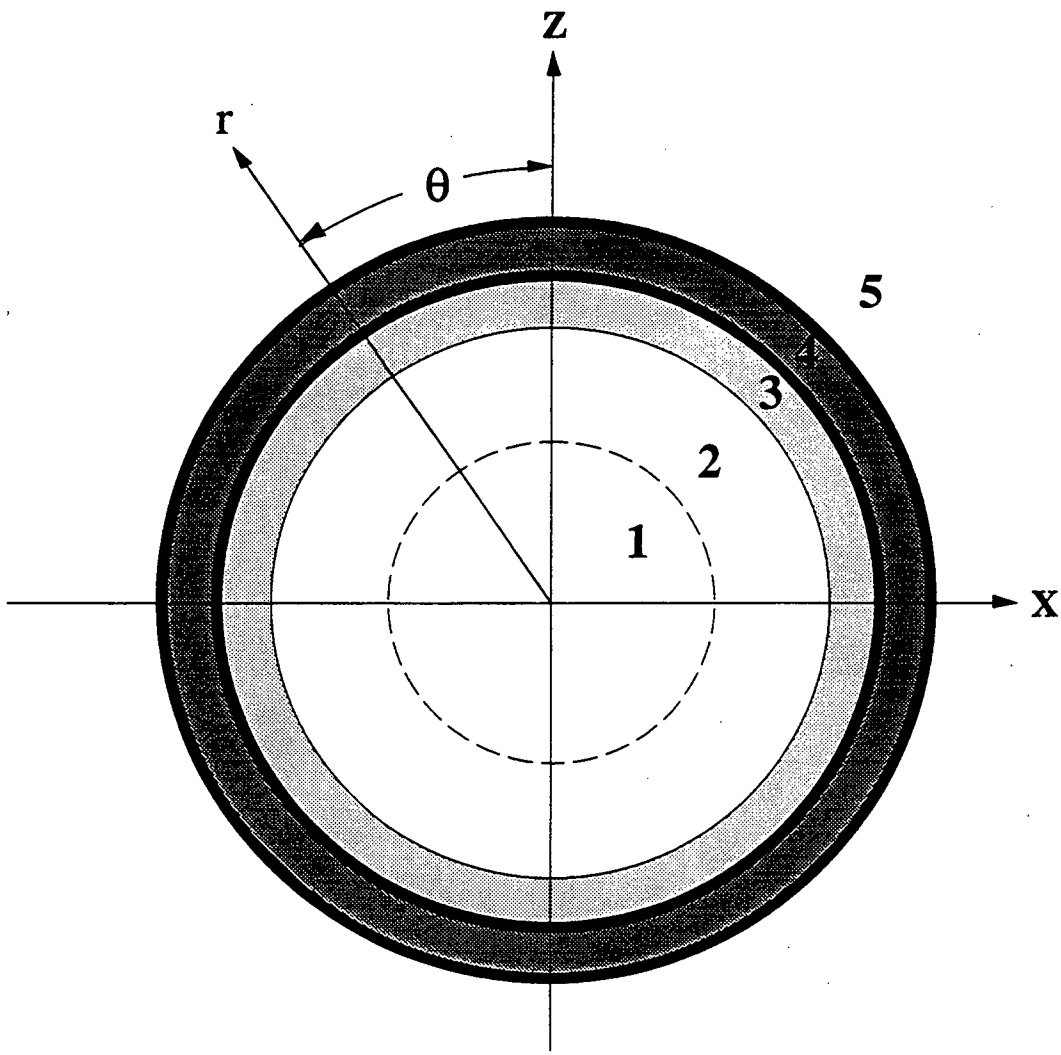

Figure 3.6 Coaxial regions defined by Zimmerman and Forster in the derivation of equation 3.2. The light gray area, region **3**, is the xenon solid. Regions **1** and **2** are low pressure xenon gas and the dark gray area, region **4**, is the glass cell. The magnetic field, $\vec{B}$, is directed along the Z direction.

region i due to the susceptibility is given by the following:

$$H_i/H_\circ = \left[1 - \tfrac{1}{2}(\mu_i - \mu_5)\right] - \tfrac{1}{2}\sum_{j=1}^{j=i-1} a_j^2(\mu_{j+1} - \mu_j)\cos(2\theta)/r^2, \qquad (3.2)$$

where μ_i are the permeabilities of the various regions, a_j is the outer radius of region j, and $\cos(2\theta)$ describes the angular dependence (for a cylindrical annulus) of the anisotropic bulk magnetic susceptibility. For our case, i = 3, $\mu_5 = \mu_{N_2} = 1$ (low pressure Xe gas), and $\mu_5 = \mu_{N_2} = 1$ so

$$H_3/H_\circ = \left[1 - \tfrac{1}{2}(\mu_3 - 1)\right] - \tfrac{1}{2}a_2^2(\mu_3 - 1)\cos(2\theta)/r^2. \qquad (3.3)$$

The first term contains the isotropic susceptibility shift, and the second can be expressed in terms of volume susceptibility (χ_V) using rationalized SI units, $\mu = 1 + \chi_V$. At $r = a_3$ the maximum and minimum values are observed at θ = 0 and 90° respectively, and the difference is just

$$\Delta H_3/H_\circ = \left(a_2/a_3\right)^2 \chi_3 \qquad (3.4)$$

which, for a thin film where $a_3 \approx a_2$, simplifies to χ_3. As the thickness of the film is increased, and

$$\left(a_2/a_3\right)^2 < 1 \qquad (3.5)$$

the outer lines of the spectrum start to show considerable curvature (ref. [154], Fig. 6) that is visible in the spectra of Chu et al. [152] for coaxial water samples.

The related problem of describing the anisotropic chemical shift line shapes for a distribution of molecular crystallites was first considered by Bloembergen and Rowland [155] (see also Mehring [29] and Haeberlen [2]). Haeberlen's derivation [2] of the line shape is adapted to the susceptibility problem as follows. The angular dependence of the magnetic susceptibility can be described by a $\cos(2\theta)$ dependence where θ is the angle between the normal to the plane of the film and the magnetic field. The line shape for an arbitrary sample geometry may be complicated, as in the case of a general ellipsoid with

axes a ≠ b ≠ c. However, for symmetric cases with no radial dependence, the line shapes simplify considerably. The frequency components of the spectrum can be written in terms of the film orientation and the bulk magnetic susceptibility:

$$\Delta\omega = \omega/\omega_{\circ} - \left[1 + \sigma + \delta - \tfrac{1}{2}\chi\cos(2\theta)\right] \tag{3.6}$$

where σ is the chemical shift (which may be temperature dependent, as in the case of solid xenon), δ is the isotropic bulk magnetic susceptibility shift (which from equation 3.3 equals $-\frac{1}{2}\chi$ for a cylinder), and $\omega_{\circ}$ is the reference frequency. The intensity of the spectrum may be written, integrated over all angles, as

$$\int I(\omega)d\omega = \iint dA(\theta,\phi) \tag{3.7}$$

In order to express the area element, dA (which is dθ for a cylindrical distribution with the cylinder axis perpendicular to the magnetic field as in figure 3.6) in terms of the frequency, we want to find dθ in terms of dω [152, 154]. Inverting equation (3.6)

$$\theta = \tfrac{1}{2}\arccos(-2\Delta\omega/\chi) \tag{3.8}$$

where $\Delta\omega = \omega/\omega_{\circ} - \left[1 + \sigma + \delta\right]$, and differentiating,

$$d\theta = \frac{1}{\chi\omega_{\circ}}\frac{d\omega}{\sqrt{1-(2\Delta\omega/\chi)^2}} \tag{3.9}$$

We can see from equation 3.7, that since dA=dθ, this *is* the line shape for the cylindrical cell in figure 3.6. The two singularities are at $\Delta\omega = \pm\frac{1}{2}\chi$ relative to the isotropic susceptibility shift $\delta_{cylinder} = -\frac{1}{2}\chi$. The total width of the spectrum is χ, from equation 3.4. This is the same as the line shape expected for an axially symmetric *two dimensional* chemical shift pattern in a powder (namely, an isotropic distribution of orientations about one axis of rotation (θ) with respect to the magnetic field). This is the case for a polymer sample fully oriented along one axis, but randomly oriented azimuthally [29, 30], as discussed in chapter 1.

For the case of spherical film geometry the elemental area dA is $\sin\theta\, d\theta$ and the frequency dependence of the film's orientation is determined by substituting $-\frac{2}{3}P_2(\cos\theta)+\frac{1}{6}$ for $-\frac{1}{2}\cos(2\theta)$, which partitions the angular dependence into isotropic and anisotropic parts for a spherical distribution. Adding $-\frac{1}{2}\chi$ to $-\frac{1}{2}\chi$ gives the isotropic shift for the sphere, $\delta_{sphere}=-\frac{1}{3}\chi$. Inverting equation (3.8), differentiating, and using equation (3.7) as before yields the well known line shape

$$I(\omega)=\frac{1}{2\chi\omega_o}\frac{1}{\sqrt{\frac{1}{3}-\Delta\omega/\chi}} \qquad (3.10)$$

with a singularity at $\Delta\omega=+\frac{1}{3}\chi$ relative to δ_{sphere}. The width of the spectrum is again χ. Note that although the expressions derived here are similar to those for microscopic chemical shifts (section 1.2), here we are concerned with the *macroscopic* distribution of a film in the magnetic field.

3.2.2 Experimental

The experimental methods and apparatus were described in section 3.1. Briefly, the ^{129}Xe nuclei become polarized via spin-exchange collisions with rubidium atoms. After pumping for about 30 minutes, the polarized xenon is transported to the NMR sample region in high magnetic field and frozen at temperatures below 150K onto the surfaces of NMR sample cells with various geometries. The setup of the highfield sample region was that of figure 3.3a for all of these experiments. The 5 turn solenoid rf coil is approximately 2 cm in length and diameter. The sample region is cooled with cold flowing nitrogen gas and is temperature regulated to within ±1K using a nichrome wire heater. For the spin-echo experiments mentioned below, a Carr-Purcell sequence [156], consisting of evenly-spaced 180° pulses, which refocus the inhomogeneous decay of the magnetization, was applied after a single 90° pulse. In general, spectra were obtained immediately after freezing the xenon into the sample regions. However, in order to perform experiments in the capillary tube the temperature was dropped from 5K above the freezing temperature

(145K for a xenon pressure of 220 Torr) to 10K colder to prevent xenon from freezing outside the sample region.

3.2.3 Results

Spectra are shown in figures 3.7, 3.8, 3.9 for xenon films in several differently shaped NMR sample cells. Schematic figures are shown next to each spectrum illustrating the sample cell geometry: flat rectangular boxes parallel and perpendicular to B_0, cylinder, and sphere. No broadening has been applied to any of the spectra. Figure 3.8 shows the difference in the spectra for a cylindrically shaped thin film (a) versus a bulk cylindrical solid formed in a capillary tube 250 μm in diameter (b). The xenon freezes relatively uniformly throughout the capillary volume, as indicated by the symmetric line shape and uniform shift of $\frac{1}{2}\chi$ (to within experimental error), as expected.

Figure 3.9 shows spectra for spherically-shaped films at 148K and 123K. At the lower temperature, magnetic dipole-dipole interactions cause a homogeneous broadening of the line as seen in Figure 3.9(a). At the higher temperature, the spectral features are very sharp because self diffusion in the solid averages out the dipole-dipole couplings. The isotropic *chemical shift* is also lower as discussed below. Carr-Purcell spin-echo experiments [156] show that the homogeneous line width is only 10 Hz at 148K, in accordance with the results of Yen and Norberg [148] (corrected for isotopic enrichment) who studied the effects of self diffusion on the line width in bulk solid xenon. A fit to equation 3.12 for the spherical film in figure 3.9(b) gives χ = 13.6 ppm and a residual Gaussian broadening of 25 Hz. The value of the molar bulk magnetic susceptibility is -43.9 x 10^6 (cgs) [157], in agreement with *ab initio* calculations [23], that can be converted to a volume susceptibility (in rationalized SI units) by the following expression (in ppm) [152]:

$$\chi_V = 4\pi\chi_M\rho / M \qquad (3.11)$$

where ρ is the density and M is the mass. χ_D for xenon is -14.8 ppm, which is in good

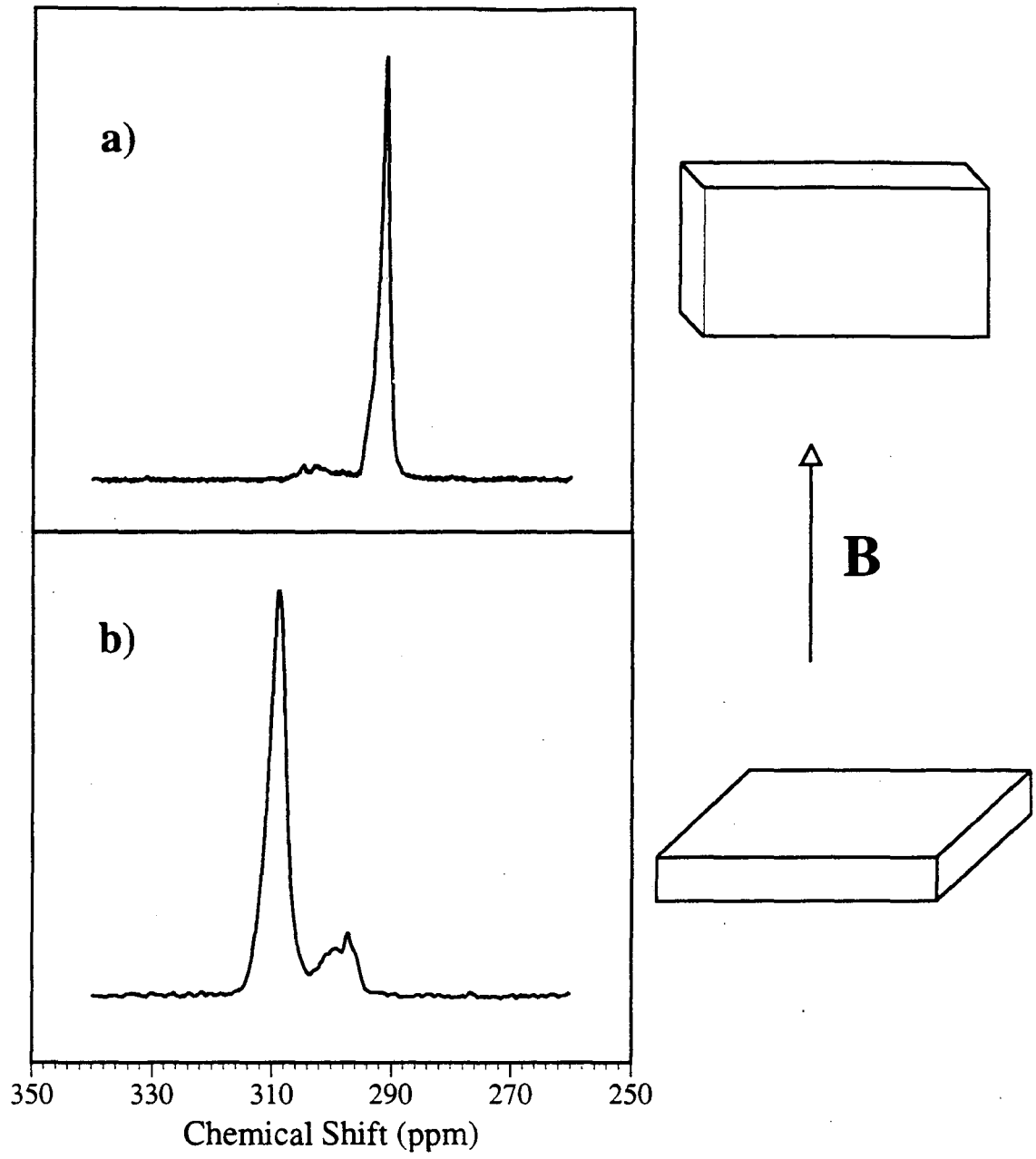

Figure 3.7 ^{129}Xe NMR spectra for xenon thin films frozen on the surfaces of sample cells with different geometries: flat rectangular box (3.0 cm x 1.0 cm x 0.1 cm) with normal (a) parallel and (b) perpendicular to B (oriented as shown in the plane of the paper).

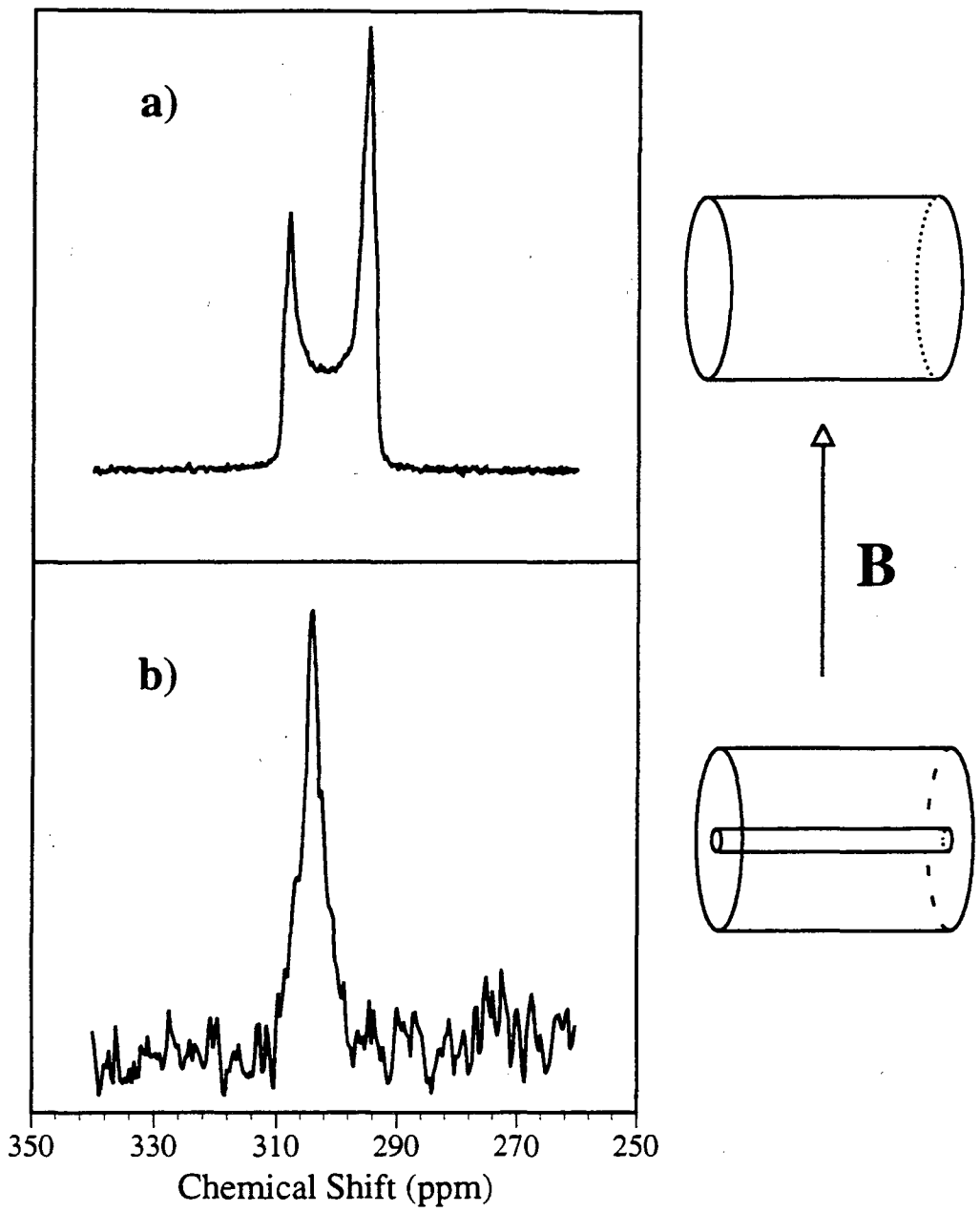

Figure 3.8 The spectrum for the (a) cylindrical (1 cm diameter) thin film shows two sharp singularities while in (b) only the isotropic (average) value is observed in the 250 μm capillary tube. Residual susceptibility effects broaden the line in the capillary by about 150 Hz. The asymmetry in (a) is due to the presence of an additional vertical wall at the end of the sample tube.

agreement with the observed splitting in the cylindrical sample (figure 3.8(a)) of 15.1 ppm. The difference between the two values as well as the difference between the sphere and cylinder probably arises from the susceptibility of the glass.

We also investigated the temperature dependence of the chemical shift of the solid for the flat rectangular sample cell (figure 3.7(a)) to avoid isotropic susceptibility shifts. The temperature dependence is plotted in figure 3.10 with a linear least squares fit with a slope of -0.278 ppm/°C. Converting to density using the data from Packard and Swenson [158], we find the density dependence to be 0.575 ppm/amagat, in agreement with the work of Brinkmann and Carr [144, 159]. Experiments were also performed using the cylindrical sample cell at different temperatures, and no temperature dependence of χ_D was observed, as expected.

3.2.4 Discussion

In Laloë's ^{3}He experiments mentioned earlier, the observed spectrum in a cylindrical container consisted of a gas phase signal and two additional lines due to vertical ($\theta = \pi/2$) and horizontal ($\theta = 0$) films, consistent with the $M_0 P_2(\cos\theta)$) dependence of the film orientation. As the film crept (because of gravity) from the sides of the sample region to the bottom, the intensity of the peak due to the vertical film decreased in favor of the peak for the horizontal film. The line shape for our cells showed a slow time dependence that was probably due to temperature gradients that caused a slow, macroscopic migration of the film towards the coldest part of the sample cells. In the spherical cell, the low field (higher resonance frequency) part of the spectrum was observed to decrease in intensity. In the cylindrical cell, however, the opposite was observed, with the line shape changing to enhance the low field part of the spectrum. These effects could not be due to gravity (as in the case of liquid ^{3}He films) that would cause a drift to higher resonance frequency in all of our samples.

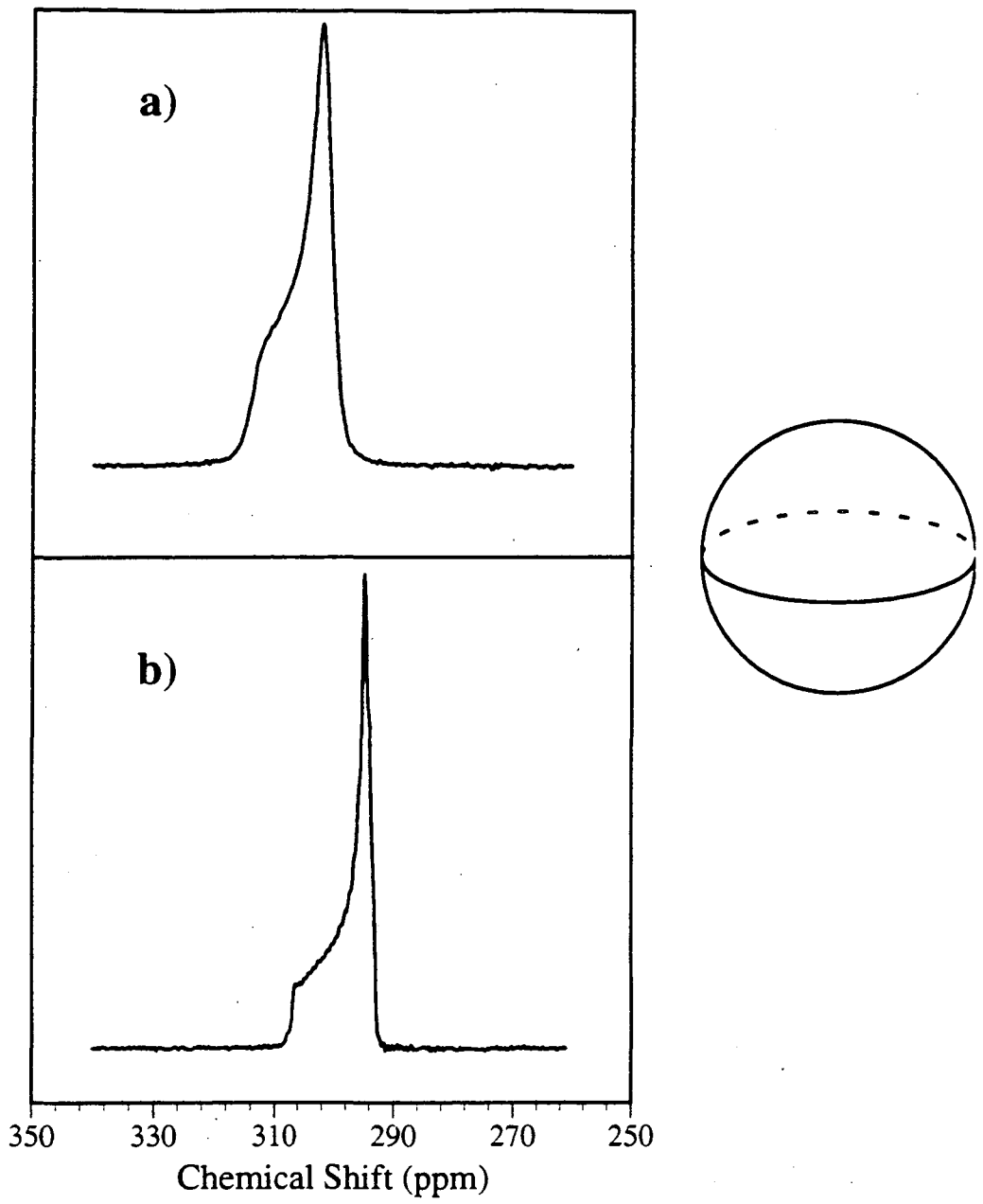

Figure 3.9 Spectra of xenon thin films in the spherical sample cell (0.6 cm radius) at (a) T = 148K, the residual line width is only 25 Hz. The chemical shift of the singularity is 295 ppm. (b) At T = 123K, the residual line width is now 160 Hz and the chemical shift of the singularity is 303 ppm.

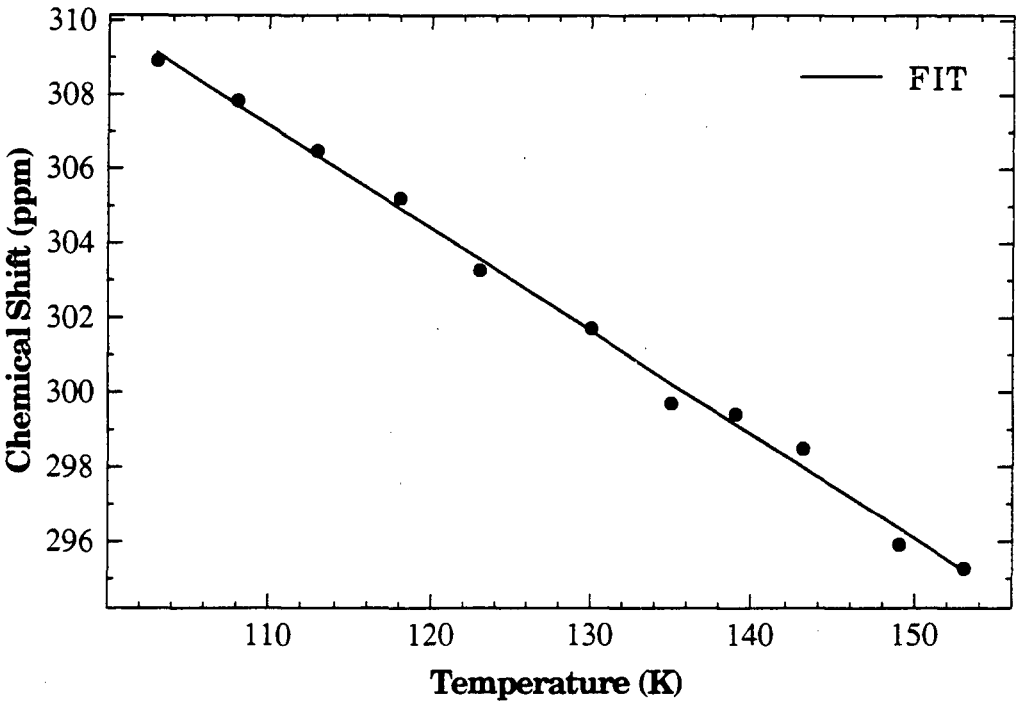

Figure 3.10 Temperature dependence of the chemical shift in xenon solid. The line represents a least squares fit to the data which has a slope -0.278 ppm/K. Errors are on the order of the size of the point.

The residual broadening of the spectrum for the spherical sample at 148K (25 Hz) is somewhat large compared to the expected value from Yen and Norberg [148]. At such temperatures, diffusion is present in the solid which has the effect of narrowing the line width. However, spin echo experiments showed that the observed broadening was inhomogeneous in nature and probably due to residual magnetic field inhomogeneities over the sample volume. The fits to the line shapes also indicated a slightly non-uniform film formation (film thickness is about 5% greater at the equator than at the poles). Residual susceptibility effects can account for the residual line widths in the flat cells and the capillary tube. At lower temperatures (below 118K), the xenon spectrum observed has the expected rigid lattice line width of 576 Hz [148], when corrected for our higher ^{129}Xe isotopic abundance.

In summary, optical pumping techniques allow the observation of ^{129}Xe NMR in xenon thin films with an area of about 10 cm^2 and thickness of 1 μm ($\approx$2000 atomic layers). Bulk diamagnetic susceptibility effects are easily seen and understood in terms of line shapes corresponding to different distributions of orientations of the films with respect to the applied magnetic field. Effects of temperature on the chemical shift and the line broadening are readily observed in the spectra.

3.3 Survey of Surfaces

Spin polarized xenon can be an excellent probe of surfaces using the high field NMR setup described at the beginning of this chapter. This section shows preliminary results from a variety of different materials. No complete analysis is given for any of these spectra, they are meant to illustrate the possibilities and limitations of using spin polarized xenon as a probe of various different types of surfaces.

3.3.1 High Surface Area Materials

Several high surface area materials were investigated to provide a bridge to previous conventional xenon NMR studies briefly discussed in chapter 1. Several of these systems have relatively short T_1 and a multiple pulse/acquisition technique was used to obtain the spectra. In figure 3.11 room temperature spectra are shown of xenon in NaY zeolite and amorphous carbon about 100 msec after adsorption. The chemical shift in the zeolite is 59 ppm consistent with the results of Ito and Fraissard [32] extrapolated to zero pressure. The Thermax (amorphous) carbon can be compared to the work of Ryoo et al. [160] where a several different grades of carbon were studied. It is interesting to note the time dependence which existed in both of these cases. The line width was initially about 600-700 Hz in both cases and became equal to its equilibrium value in ≈100 msec. Activated carbon, with a surface area of >900 m^2/g was also studied briefly and gave a line width three time larger than the equilibrium spectra although the chemical shifts were identical (44 ppm).

Xenon was observed on magnesium oxide and aluminum oxide but the lines were extremely broad and the relaxation times short (< 1 second) and so it is not known if the xenon had fully equilibrated with the surface. Xenon was also studied adsorbed onto Degussa Aerosil 300R (surface area $300m^2/g$) which has methyl capping groups on the silica surface. The line shape of the xenon strongly resembled that of a chemical shift anisotropy. Observing the time development of the signal probed at five second intervals show that the relaxation is very different across the line with the fastest relaxation taking place at the low frequency edge. It is also possible that this effect is due to migration among the distribution of sites on the surface. Further quantitative work is necessary to clarify the situation.

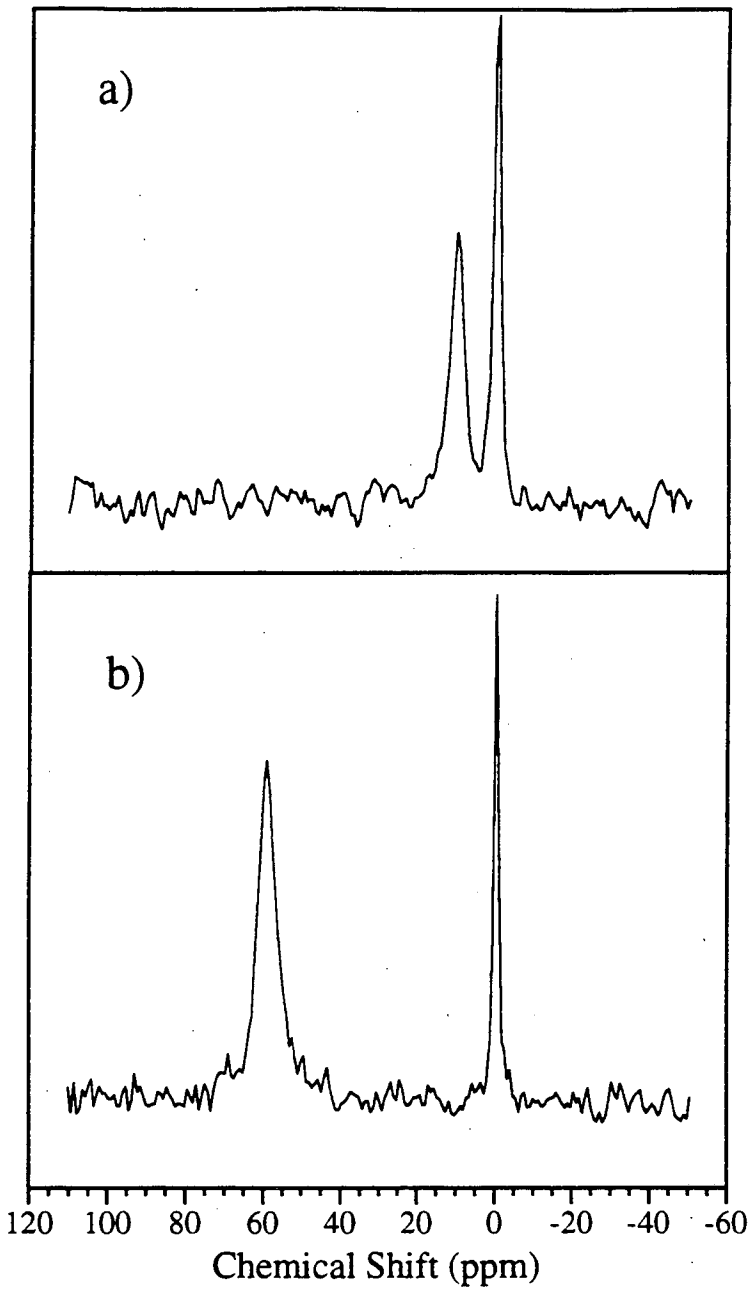

Figure 3.11 Xenon adsorbed on (a) Thermax (δ=10 ppm) and (b) NaY zeolite (δ=59 ppm).

3.3.2 Salts

An attempt was made to study the surfaces of some salts (Figure 3.12) which can have large adsorption energies (6-7 kcal/mol). The adsorbed peaks show signs of interesting substructure but the extremely short T_1 (≈200 msec at -120°C) made observations under equilibrium conditions impossible. Even with ultrahigh purity NaCl (99.9999%, Puratronic Inc., Fe content <0.2 ppm, other metals <0.5 ppm) the relaxation time was quite short (1-2 seconds at -130°C) undoubtedly due to residual paramagnetic impurities at the surface. Neue [161] has derived a theoretical equation to describe the T_1 due to surface diffusion at a fixed distance, z, past paramagnetic sites of density N_e

$$1/T_1 = \frac{2\pi N_e}{5Dz^2}\gamma_{Xe}^2\gamma_e^2\left[\tfrac{1}{3}C(\omega_I-\omega_S)+C(\omega_I)+2C(\omega_I+\omega_S)\right], \qquad (3.12)$$

where the spectral density, $C(\omega)$, is given by a complicated integral numerically evaluated by Neue. Korb et al. [162, 163] have made several detailed studies of relaxation in two dimensions due to dipolar interactions, which have several qualitative differences from the well known features of BPP theory [164]. By relaxation measurements at several fields it may be possible to infer the surface diffusion constant. However, in contrast to the low field system in the previous chapter, it is very difficult to make accurate spin-lattice relaxation measurements with the apparatus described in this chapter. The sample actually occupies only a small fraction of the volume of the glassware containing the xenon and thus fresh spin polarized xenon can continually diffuse up into the sample region (probed by small tipping angle rf pulses) making the T_1 appear longer than it really is.

3.3.3 Molecular Crystals

Several molecular crystals were studied with some success. The areas are typically very low as nonporous crystallites ≈1 micron in size with densities around 1g/cm^3 have surface areas of ≤1m^2/g. The samples could be purified to the extent that the T_1 was quite long (30-60 seconds) allowing a much longer equilibration time than the high surface area materials or salts. These material parameters were practically inaccessible to conventional

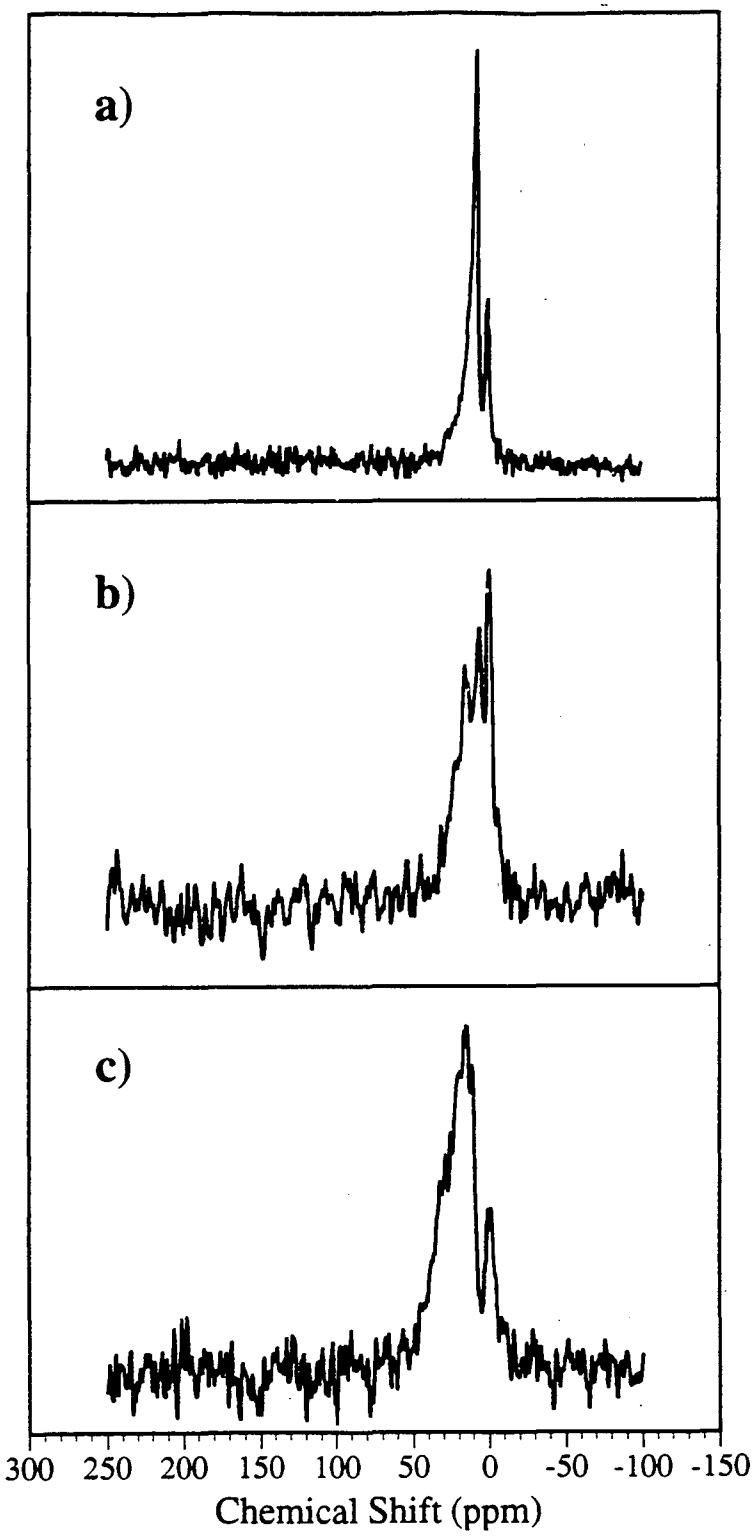

Figure 3.12 Xenon adsorbed on various salts, T≈-120°C. (a) Sodium Chloride (NaCl), (b) Pyridine hydrochloride ($C_5H_5N{\cdot}HCl$), (c) Cesium Iodide (CeI).

xenon NMR, and are thus their study is of considerable interest. In particular interaction between xenon and large aromatic molecules has been studied theoretically recently [165]. Several molecules were studied with polarized xenon with 2,3-benzanthracene being studied in some detail [108]. In figure 3.13 spectra are shown for polarized ^{129}Xe in the presence of 0.96 g of 1,2-benzanthracene (surface area $\approx$0.5 m^2/g as estimated by average particle size from electron micrographs) at several temperatures. Next to each spectra is a schematic picture of the xenon interacting with the surface. At room temperature only a narrow peak due to gas phase ^{129}Xe is observed at the same resonance frequency as the pure optically pumped xenon gas; at this temperature the average surface residence time is so short that the interaction is negligible. When polarized xenon gas is admitted to the sample at lower temperatures, the residence time goes up. At -115°C, xenon adsorbed onto the surface has a resonant frequency which is shifted by 10 ppm compared to the gas peak. At -120°C, the peak associated with adsorbed xenon is observed at 32 ppm relative to the gas and has a somewhat asymmetric line shape. The chemical shift and line width increase with decreasing temperature, indicates a continual increase in the residence time and decrease of the mobility of the adsorbed xenon. The line shape of the adsorbed xenon signal at lower temperatures may arise from a chemical shift anisotropy on the surface of the benzanthracene, but it could not be quantified as the T_1 became shorter at the lowest temperatures before freezing and the signal-to-noise ratio suffered considerably. Below 130K, only the signal of polarized solid xenon is detected. Studies of 1,2-benzanthracene, which due to different crystal packing has a melting point 150 degrees higher, showed slightly different behavior with less broadening at lower temperatures and shorter T_1. Xenon adsorbed on ferrocene showed results similar to the benzanthracene study.

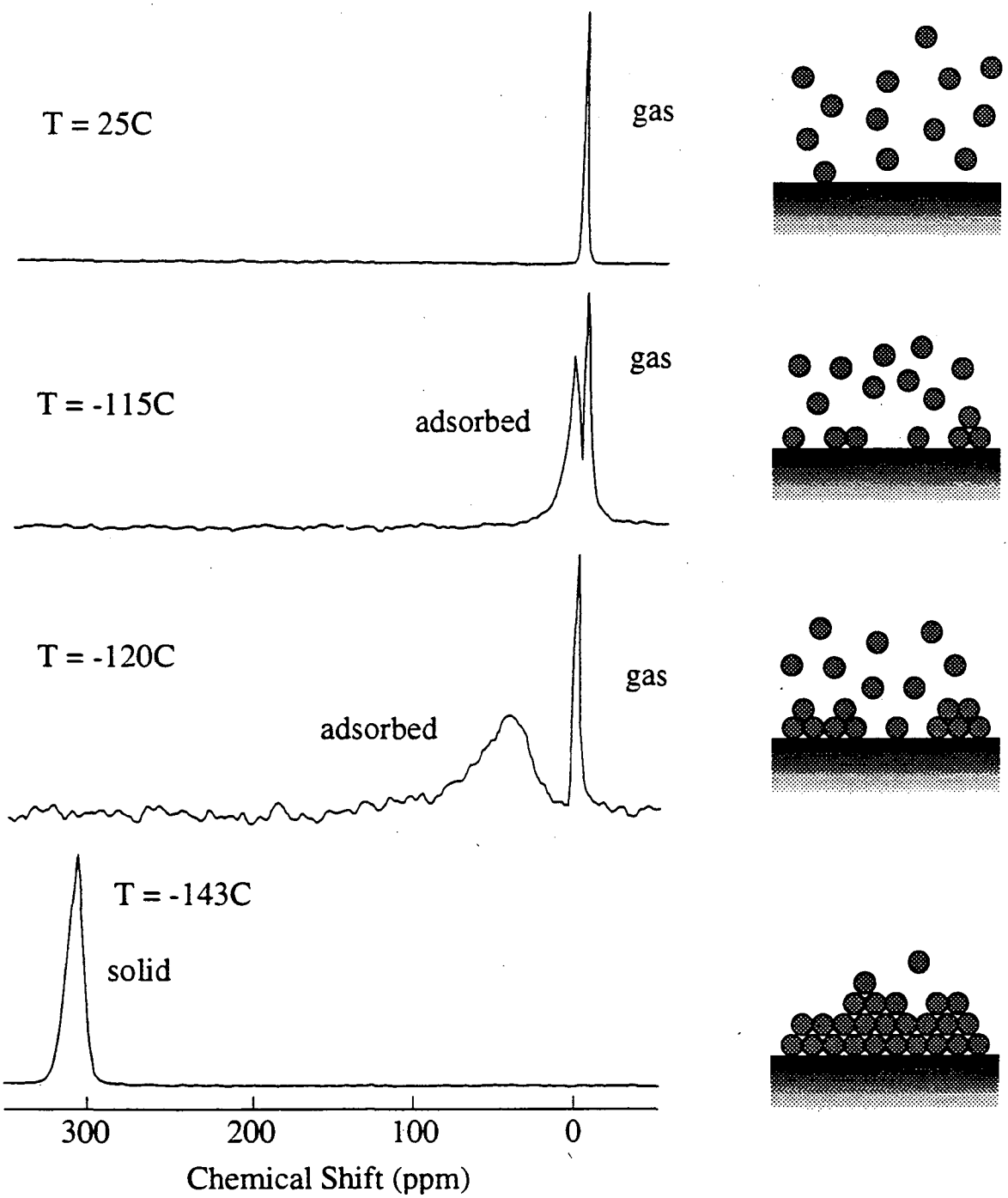

Figure 3.13 Xenon interacting with a typical molecular crystal (2,3-benzanthracene) at various temperatures.

3.3.4 Graphite

Xenon interacting with graphite is of considerable interest as it forms a model 2D incommensurate overlayer [166]. The phase transitions in this system have been the subject of intense study for the past ten years and a detailed picture of the complex phase diagram has emerged [167]. Only two NMR studies of xenon/graphite have appeared in the literature [150, 168]. A considerable experimental complication in this system is the almost bewildering variety of natural and synthetic, grades and modifications of graphite available commercially. Subsequent high temperature annealing can also have a dramatic effect on the typical size of the exposed basal planes and the amount of quasi-free electrons bound within the planes. We studied PP-100 purified natural graphite (Bay Carbon) after heating overnight at 400°C under vacuum ($<10^{-5}$ torr). Degassing at higher temperatures does not help as one sample which had been studied before and after heating under vacuum to 900°C showed a markedly shorter T_1 after heating due to cracking of the basal planes without subsequent reannealing. The EPR spectrum of PP-100 showed and intense narrow peak due to free electrons, but it was smaller than other samples that were studied, and a weak broad ESR line due to a small amount of paramagnetic metals. These were tentatively identified as Cu and Al by electron desorption spectroscopy. The lot analysis which came with the product showed < 1 ppm of all metals tested for (Cu, Co, Fe). The approximate relaxation times for xenon were always >15 seconds giving the xenon time to equilibrate with the surface. A summary of the chemical shifts vs. temperature and pressure data is given in figure 3.14. It will be shown in the next chapter that increasing pressure at constant temperature corresponds to increasing coverage and a theoretical analysis shows that the slopes of these lines depend on the mobility of the xenon. The slopes are quit small until they undergo a sharp increase between -154°C and 134°C indicative of a large increase in mobility. This behavior is in contrast to the polymer data (chapter 4, figure 4.4) where the increase in slopes vs. temperature (figure 4.7) is gradual and continuously

increasing for the entire temperature range studied. Previous studies of the xenon/graphite system have shown that the adsorbed xenon undergoes a solid-fluid phase transition at -125°C (and approximately one monolayer coverage). However more data is needed near the transition temperature to confirm and quantify (especially with regards to the coverage) this change in mobility.

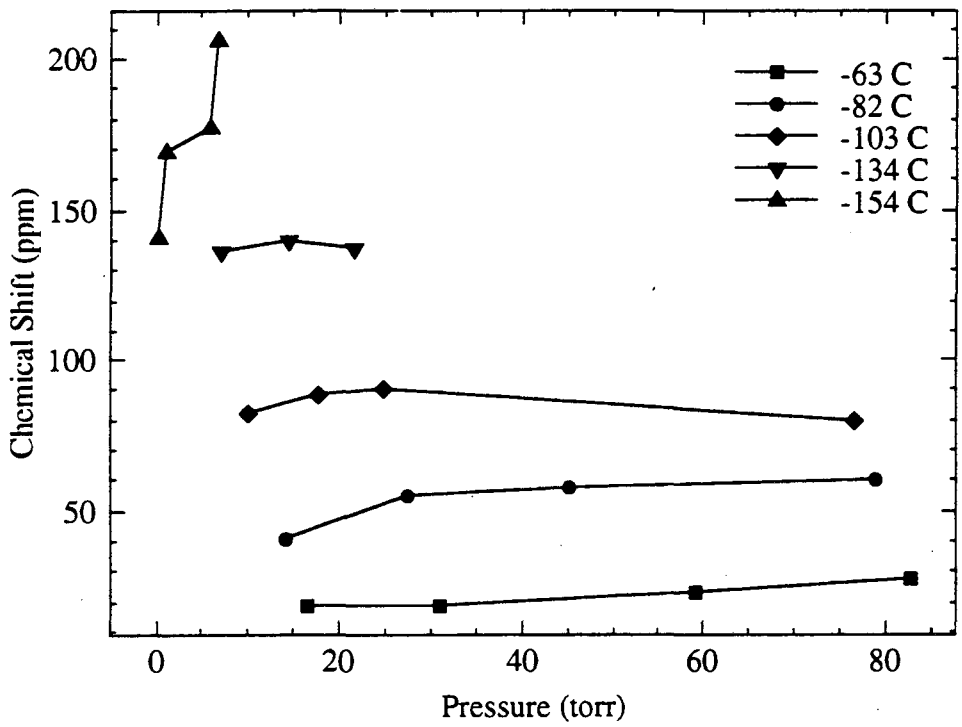

Figure 3.14 Xenon chemical shift on graphite vs. pressure at several temperatures.

3.3.5 Polymers

Figure 3.15 shows spectra of xenon interacting with isotactic polypropylene (Aldrich) at temperatures ranging from 72 degrees above, to 76 degrees below, its glass transition temperature (T_g=-18°C).in addition to the gas peak. When studied at 54°C (3.15a) the xenon peak was narrow (270 Hz) and located at 214.5 ppm; this chemical shift is clearly consistent with xenon which has dissolved into the *bulk* of the polymer (cf. polyethylene in figure 1.1). At room temperature (3.15a) a 470 Hz broad peak showed up at 220 ppm. This trend of decreasing line width with increasing temperature is in agreement with the results of Stengle et al. involving xenon in polyethylene [39].At both of these temperatures the spin-lattice relaxation time was extremely long (minutes) but no strong time dependence could be observed in the spectra. Right at the glass transition temperature (3.15c) for this polymer no adsorbed or dissolved xenon was observed, only pure gas. At -92°C (3.15d) a strong peak appeared which was 580 Hz broad and shifted by 19.8 ppm. This xenon has a much weaker interaction with the polymer and is identified with xenon which is rapidly exchanging with the gas, while the peak at zero ppm is from xenon gas that does not exchange with the surface on the time scale of the FID. The only other polymer which was studied above its glass transition temperature was poly(vinylidene fluoride) (T_g=-39°C) at 50°C which showed no dissolved xenon. It is not known what governs the transport of xenon into the bulk of certain polymers over others.

In summary optically polarized xenon can be observed with large sensitivity enhancements on a wide range of materials. Some are difficult to study accurately due to a short spin-lattice relaxation time, others await a more thorough analysis. The next chapter will examine the adsorption phenomenon displayed in 3.15d in great detail. Data set is acquired much like that obtained with graphite (chemical shift vs. temperature *and* pressure). This data is then quantitatively analyzed by determining the degree of surface coverage (θ) at each data point and interpreting the results with a simple model of adsorption and diffusion on the polymer surface.

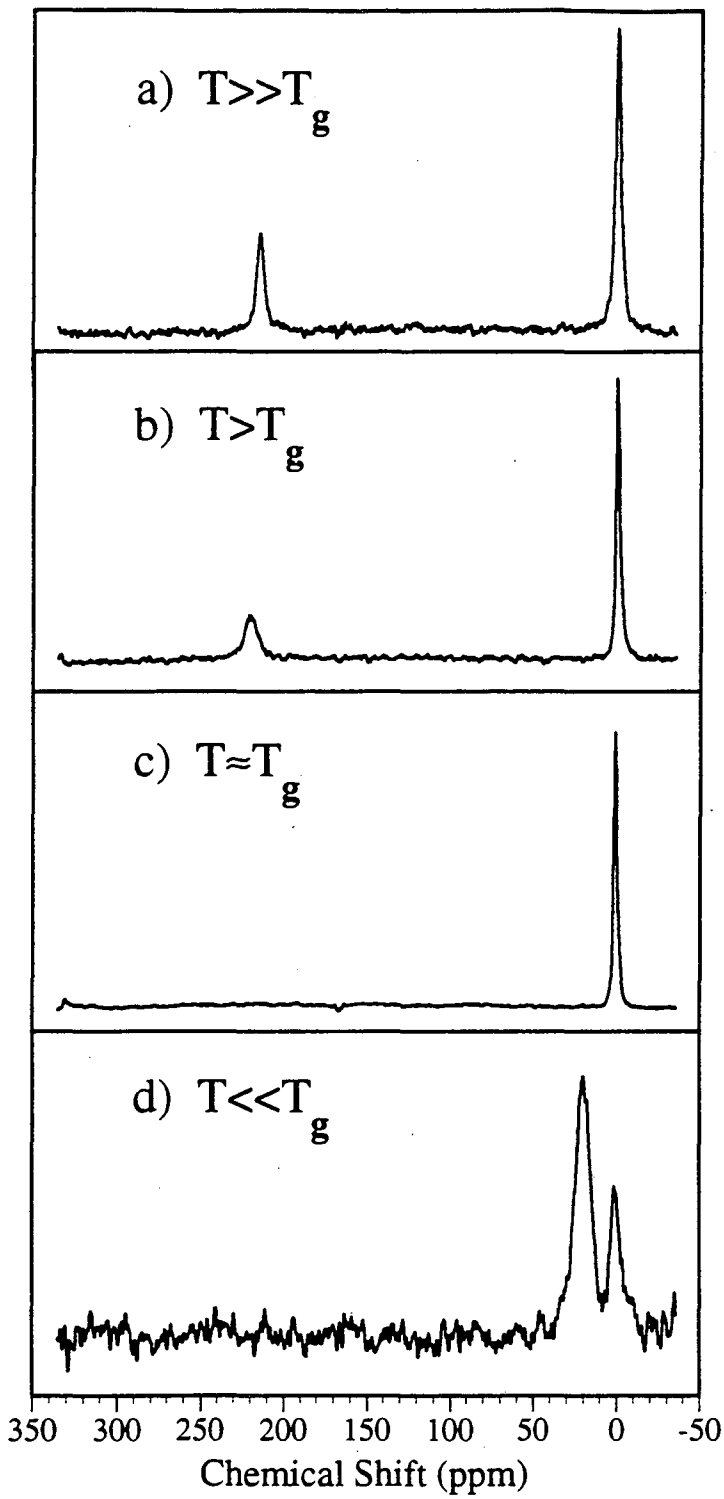

Figure 3.15 Xenon interacting with polypropylene at different temperatures. (a) T=54°C (b) T =25°C (c) T=-19°C (d) T=-92°C. P≈155 torr for all temperatures.

CHAPTER 4 Applications to Polymer Surfaces

4.1 Introduction

In this chapter the techniques and methods of the previous chapter are applied to several polymers. In these systems the structure is not as simple as graphite or salts and unique considerations such as the surface morphology and solubility of the xenon become extremely important. The morphology of the surface is extremely difficult to determine by any means and is unknown in almost all cases. The hope for xenon NMR is that, under the appropriate conditions, it will be able to probe the chemical functionality's exposed on the polymer surface. Powdered, amorphous polymers typically have a moderate surface area ($<15\ m^2/g$) and xenon has both a relatively long relaxation time and significant surface interaction on many. The results of the previous chapter have shown the dramatic effects of both temperature and pressure on the chemical shift of the adsorbed xenon. Here the chemical shift of adsorbed xenon as a function of temperature and pressure is shown to yield information about the xenon-surface interaction and the diffusion of xenon over the polymer surface. The magnitude of the xenon-surface interaction is measured by the temperature dependence of the chemical shift extrapolated to zero xenon pressure. This allows the extraction of a single chemical shift value characteristic of the surface. From the pressure dependence of the chemical shift, a rough estimate can be made of the diffusion coefficient of xenon at monolayer coverage. Several polymers have been studied but a complete analysis has only been carried through for poly(acrylic acid) (PAA) and

poly(acrylonitrile) (PAN). Preliminary results are summarized for a homologous series of polymers with the structure —$(CH_2CHX)_n$—. In the last section a completely different polymer is studied by xenon NMR with and without optical pumping.

4.2 Experimental Methods

4.2.1 Procedure.

Rubidium vapor, with xenon gas added, is optically pumped for approximately 30 minutes at temperatures between 80 °C and 120 °C, so that the adsorption of incident pumping light is between 50% to 100%. After pumping, the cell is cooled to approximately 40 °C to reduce the vapor pressure of rubidium in the pumping cell. The spin polarized xenon does not relax appreciably during this cooling period (≈1 minute). The stopcock is then opened and polarized xenon flows (in less than 1 second) up to the sample region where it can adsorb onto the sample. To allow the xenon to reach equilibrium after adsorption onto the sample, there is typically a delay of 30-60 seconds before acquiring data. Spectra are recorded by Fourier transformation of the signal following a short (typically 45°) rf pulse.

The equilibration of xenon with the surface was checked in separate experiments by applying small tipping angle pulses at 10 second intervals and observing spectra that are time independent after several scans. This also allows us to estimate the relaxation time of ≈30 seconds at low temperatures. The xenon equilibration was independently checked with a sealed sample of treated (see below) poly(acrylic acid) filled with ≈3 atmospheres of enriched (80%) ^{129}Xe and ≈100 torr of oxygen to reduce the T_1 to <5 seconds. This sample was slowly cooled and brought to thermal equilibration at several temperatures that were used in the optical pumping experiments. The spectra showed line widths identical with optical pumping spectra on the treated polymer. It was shown with several samples (e.g. zeolites, carbon black) in the last chapter that when xenon does not reach equilibrium with a surface the line width is time dependent and larger than when it is in equilibrium.

With the diode laser used for most of these studies, spectra for optically pumped xenon gas were obtained with typical signal-to-noise enhancements of about 800 over a conventional high-field NMR spectrum. Conventional experiments, with signal averaging one shot every T_1 for our pumping period, would achieve an increase in signal-to-noise of only 8 and thus would be unable to observe the adsorbed xenon under the conditions of this experiment. Adding oxygen as was done in the sealed sample mentioned above would increase the rate of signal accumulation, however, it would introduce a contact shift that would be difficult to assess on a surface.

After the data acquisition, the sample is allowed to warm and the xenon is recycled by freezing it back into the xenon reservoir (see Figures 3.1 and 3.2) with liquid nitrogen. Since the xenon sometimes becomes slightly contaminated during the experiment, the xenon is purified before being returned to the pumping cell by first heating it with a small amount of rubidium metal in the xenon reservoir. Water and other contaminants react very quickly with the rubidium vapor. The xenon must be very pure since the rubidium concentration in the pumping cell is only ~10^{-5} torr and a very small amount of contaminant will greatly diminish the pumping efficiency.

4.2.2 Sample Treatment.

The preparation of a clean surface is a main concern in surface studies. Although with powdered, organic materials it is impossible to use the pretreatments employed in conventional surface science techniques (annealing, polishing or sputtering), it was attempted to treat the samples in a manner consistent with other studies of powdered materials. This consisted of evacuation at room temperature or higher to eliminate as much as possible, physisorbed molecules such as water or oxygen. Powdered poly(acrylic acid) (Aldrich, Milwaukee, WI) was treated overnight under vacuum at 80 °C since water adsorbs strongly on this polymer. As discussed below, the surface treatment strongly affected the NMR spectra of xenon adsorbed on poly(acrylic acid). The sample was then

loaded into the probe in a nitrogen filled glove bag and then immediately evacuated to below 10^{-5} torr and stored under vacuum until the xenon gas was introduced.

4.2.3 Isotherms

Nitrogen and xenon isotherms were carried out in order to measure the surface area and adsorption energy of xenon on poly(acrylic acid) and the BET (Brunauer, Emmet, Teller) isotherm [169] gave an excellent fit to the data. The BET isotherm has been analyzed and derived from statistical mechanics [170] where it was shown that several of the assumptions underlying it are rather implausible. However, experimantally it compares favorably to several alternative isotherms [171]. The equation for a BET isotherm is

$$V = \frac{V_{mon}cx}{(1-x)[1+x(c-1)]} \qquad (4.1)$$

where V is the volume of adsorbed gas at STP, $x=p/p_o$ is the reduced pressure and V_{mon} is the volume that would be occupied at STP by the amount of gas needed to form a monolayer on 1 gram of sample. The quantity c is related to the surface adsorption energy by the relation

$$\ln c = (\Delta H_{ads} - \Delta H_l)/RT, \qquad (4.2)$$

where ΔH_l is the heat of liquefaction of the adsorbate. Isotherm data were collected on a glass vacuum rack using a silicone oil diffusion pump capable of pressures below 10^{-5} torr. For the xenon isotherms conducted at low temperatures, cold temperature baths, such as liquid nitrogen/acetone were used. For accuracy, the dead volume measurements using helium gas were made at each temperature an isotherm was carried out. A final temperature correction to STP was made once V_{mon} was calculated.

As seen in Figure 4.1, the xenon isotherms on poly(acrylic acid) at 144, 148, and 166 K show characteristic BET behavior. The parameters for the xenon and nitrogen isotherms are listed in Table 4.1. Although the surface areas derived from the xenon isotherms are slightly larger than those from the nitrogen surface area measurement, the adsorption energies for xenon are relatively constant. In order to use the isotherm parameters

to analyze our chemical shift data for ^{129}Xe on poly(acrylic acid), the values of the surface areas were averaged for the three isotherms to determine V_{mon} and a value for c was calculated using equation (4.2) for each of the temperatures used in the NMR experiments giving ΔH_{ads} to be 4.2 kcal/mol. Knowing p_o from saturated vapor pressure measurements [172], equation (4.1) was used to calculate the coverage θ, which is equal to V/V_{mon}. Therefore the xenon coverage could be estimated relatively accurately without having to do an isotherm at each of the experimental temperatures by assuming ΔH_{ads} to be constant.

gas	Temp (K)	ΔH_{ads}(kcal/mol)	area (m^2/g)
xenon	166	4.22	17.2
xenon	148	4.23	16.7
xenon	144	4.21	15.7
nitrogen	77	2.28	14.4

Table 4.1 Summary of isotherm data for poly(acrylic acid)

4.3 Results for Poly(acrylic acid) [40]

As in the case of zeolites, the line shape and chemical shift of adsorbed xenon is extremely sensitive to the presence of water on the polymer surface. The large affinity of poly(acrylic acid) for water is evident from the spectra shown in Figure 4.2 of xenon adsorbed onto samples which received different pretreatments. Figure 4.2a shows the spectrum of xenon adsorbed onto a sample that had been evacuated at room temperature for two hours. The line width is very large, over 100 ppm, indicating that the xenon experiences a variety of environments on the surface that are not averaged over the NMR timescale (~ 10^{-6} s). In contrast, a relatively narrow resonance is observed for a poly(acrylic acid) sample which had been heated under vacuum at 80 °C overnight. This

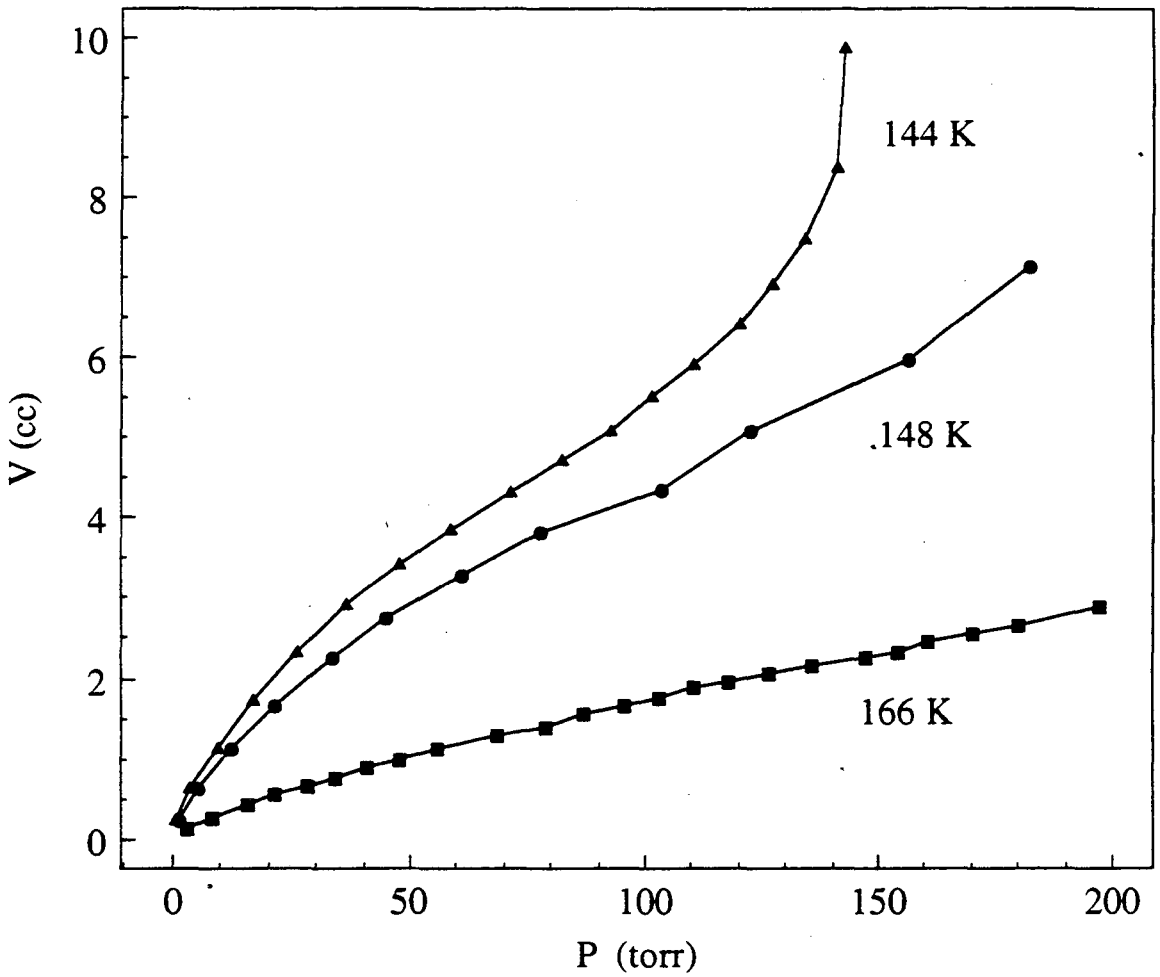

Figure 4.1 BET isotherms of xenon on poly(acrylic acid) at 144K, 148K, and 166 K. Lines connect the points to guide the eye.

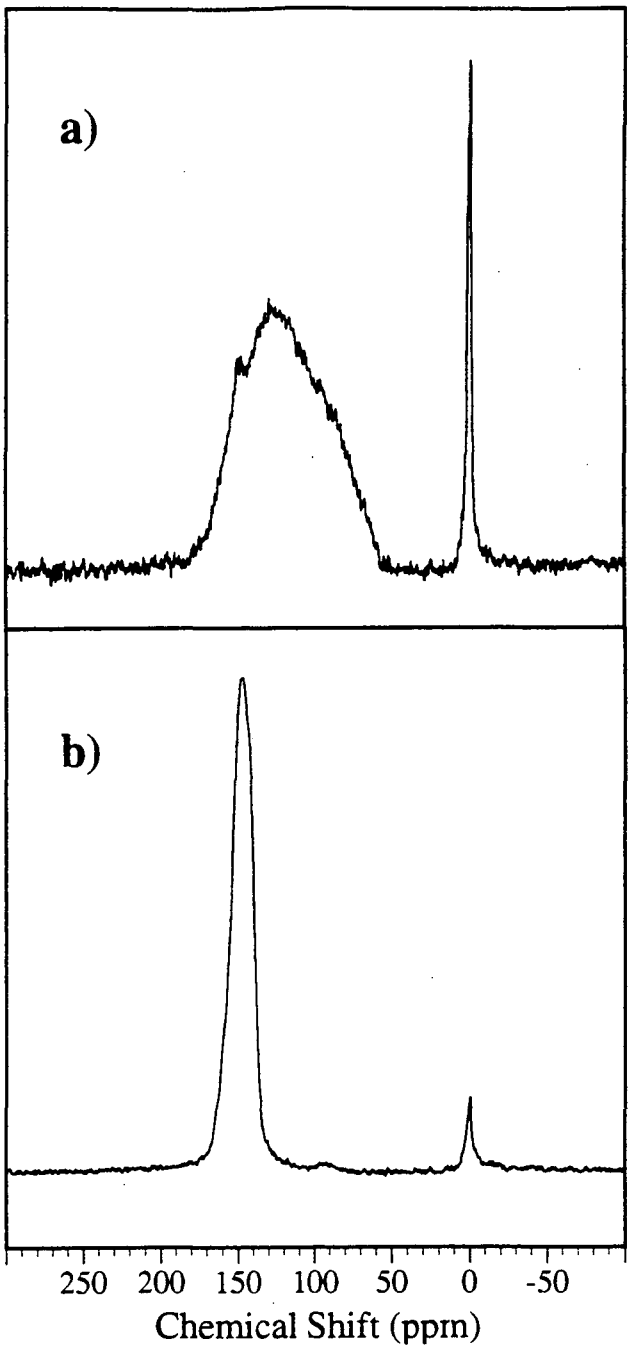

Figure 4.2 ^{129}Xe NMR spectra of xenon adsorbed at -140 C onto poly(acrylic acid) that had been evacuated previously (a) at room temperature for several hours and (b) overnight at 80 °C.

treatment produces a much more homogeneous surface as evidenced by the xenon line shape. In Figure 4.2b, the chemical shift of xenon on the heat treated polymer is 136 ppm, which corresponds to the high frequency edge of the broad resonance on the sample evacuated at room temperature. This distribution of lower chemical shifts probably results from a mediation of the xenon-surface interaction by the surface water. It is also observed that the xenon relaxation time is considerably shorter on the hydrated surface, which makes the experiment difficult to perform under equilibrium conditions. The increase in the xenon relaxation rates may be due to additional fluctuating proton-xenon dipolar interactions with mobile surface water. This trend is in contrast to that of xenon adsorbed into NaY zeolite in which the relaxation rate is found to decrease with increasing water content [173].

In Figure 4.3, the NMR spectra of optically pumped ^{129}Xe adsorbed onto poly(acrylic acid) at different temperatures show a peak at 0 ppm due to xenon gas and peaks at higher chemical shifts due to adsorbed xenon. The spectra are quite different from those of an earlier study of xenon adsorbed on benzanthracene [108] in two ways. First, at room temperature, there is already a distinct peak at 3 ppm for adsorbed xenon which is not observed in the case of benzanthracene. This is due to both the higher surface area of the poly(acrylic acid) (~15 m^2/g) over that of benzanthracene (~0.5 m^2/g) which increases the probability of finding xenon at the surface, and to a stronger xenon-surface interaction as manifested by the larger chemical shifts observed on poly(acrylic acid) at low temperatures. Second, the line widths of the spectra are narrower than for xenon on benzanthracene, due either to a higher surface mobility, or to a more homogeneous surface.

The full data set for the chemical shift of xenon adsorbed on poly(acrylic acid) is given in Figure 4.4 as a function of temperature and pressure. As the temperature is lowered, the chemical shift of the adsorbed xenon increases fairly rapidly. The variation of the pressure dependence of the adsorbed xenon shift with temperature is even more pronounced, as seen by the sharp increase of the chemical shift slopes at the lower temperatures.

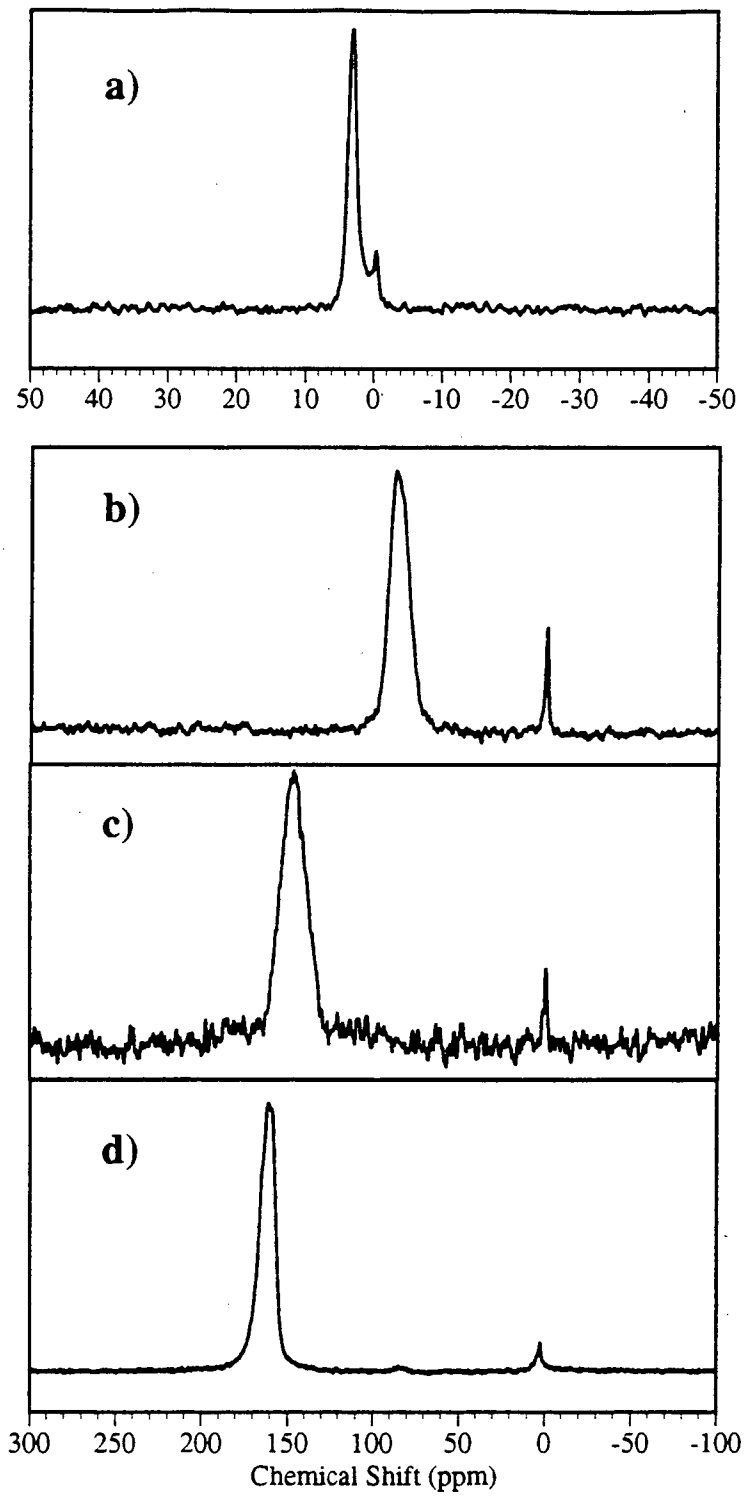

Figure 4.3 Representative NMR spectra of xenon adsorbed onto poly(acrylic acid) at various temperatures and pressures: (a) T = 299 K, P = 30 torr; (b) T = 173 K, P = 20 torr; (c) T = 153 K, P = 10 torr; and (d) T = 123 K, P = 2 torr.

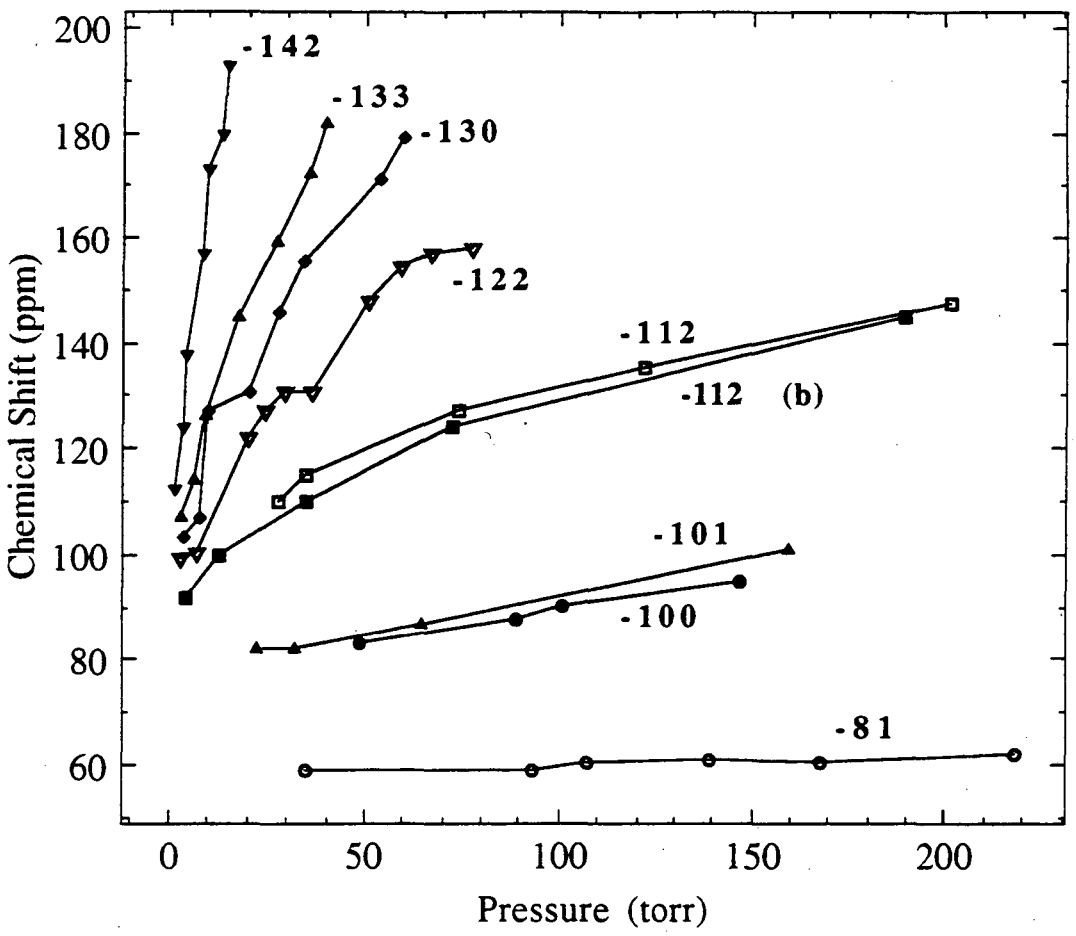

Figure 4.4 ^{129}Xe chemical shifts (ppm) of xenon adsorbed on poly(acrylic acid) as a function of pressure at the different equilibrium temperatures measured. The shifts are referenced to xenon gas at zero pressure. Lines connect the points at each temperature to guide the eye.

4.4 Theoretical Discussion

The large temperature and pressure dependence of the adsorbed xenon can be understood in terms of the xenon sticking time and diffusion on the polymer surface. Since the gas peak does not shift appreciably with temperature, the two observed resonance's do not represent xenon simply exchanging between a pure gas phase and an adsorbed phase. Instead, the xenon resonances reflect the two different regions which are present in the sample volume. First, there is the relatively isolated xenon in the gas phase with a chemical shift of 0 ppm. At room temperature, this is a sizable fraction of the xenon, but as the temperature is lowered, this fraction diminishes until about 130 K where the gas signal is no longer observed. The other fraction of xenon is in contact with the sample and is rapidly exchanging between the gas phase and the surface-adsorbed phase so that its chemical shift reflects an averaging of the xenon over the different environments.

The chemical shift of dilute xenon gas is given [174] by a virial-type expansion

$$\delta(T,\rho) = \sigma_0(T) + \sigma_1(T)\rho + \sigma_2(T)\rho^2 + \ldots \qquad (4.3)$$

where the $\sigma(T)$ are the virial coefficients of the nuclear shielding. Likewise, the chemical shift of xenon in contact with the polymer surface can be written in terms of a pure xenon-surface term, $\sigma_{0s}(T)$, and a *surface* xenon-xenon interaction, $\sigma_{1s}(T)$

$$\delta(T,\theta) = P_s\sigma_{0s}(T) + (P_s)^2\sigma_{1s}(T)\theta + (P_s)^3\sigma_{2s}(T)\theta^2 + \ldots \qquad (4.4)$$

where P_s is the probability of finding xenon at the surface and θ is the coverage in monolayers. The $(P_s)^2\sigma_{1s}\theta$ term is due to the xenon-xenon collisions which occur at or near the surface and gives rise to the observed slope of the chemical shift as a function of pressure or coverage. Fraissard has shown that the large adsorption energy in zeolites leads to an effective pressure of xenon that is quite high, resulting in many xenon-xenon collisions [32] and observes a linear dependence of chemical shift on pressure in NaX

zeolite. In our experiments the xenon chemical shift on poly(acrylic acid) also appears to be a *linear* function of the pressure at all temperatures. Therefore only the binary collisions appear to be important at the xenon coverages studied and the σ_{2s} and higher order terms can be neglected. In addition, the pressure dependence of the xenon chemical shift on poly(acrylic acid) increases dramatically at lower temperatures.

To analyze the latter effect, xenon isotherms were used to convert the temperature and pressure data to xenon coverage's. The chemical shift as a function of the coverage, θ, covers a range from 0.03 monolayers to about 1.5 monolayers of xenon on the polymer surface and is displayed in Figure 4.5. The chemical shift is found to be a linear function of coverage, although the slopes increase more modestly than in the pressure dependent plot. The slopes range from 11 ppm/monolayer at -81 °C, to about 70 ppm/monolayer at -142 °C. The slopes and intercepts of the data in Figure 8 can be analyzed in terms of a surface residence probability and the xenon-xenon chemical shift temperature dependence, as derived by Jameson and co-workers [174] and extrapolated to our experimental conditions.

The chemical shift intercepts of the adsorbed xenon resonances (that is, excluding xenon-xenon interactions) can be modeled as a chemical exchange problem such that the chemical shift consists of surface and gas (δ_g) contributions, which are weighed by the probabilities, P_s and P_g, of finding xenon in each phase,

$$\delta = \sigma_{os}P_s + \delta_g P_g \tag{4.5}$$

where $P_s + P_g = 1$. However, δ_g is our reference defined to be zero, so,

$$\delta = \sigma_{os}P_s \tag{4.6}$$

The probability of finding a xenon atom at the surface is given by,

$$P_s = \frac{\tau_s}{\tau_s+\tau_v} \tag{4.7}$$

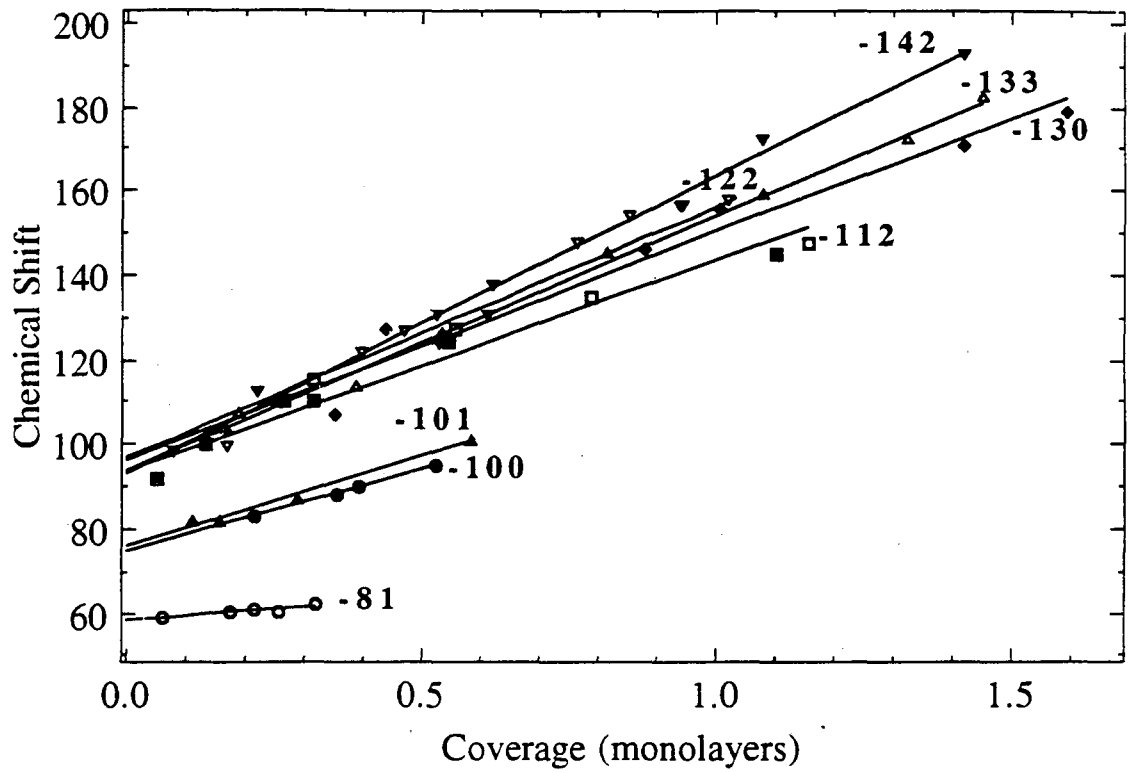

Figure 4.5 ^{129}Xe chemical shifts (ppm) as a function of the equilibrium temperature and coverage (in monolayers). Lines represent linear least squares fits to the data at each temperature.

where τ_s is the sticking time, and τ_v is the reciprocal of the collision rate with the surface. The average sticking time at the surface is given by

$$\tau_s = \tau_o e^{\Delta H_{ads}/kT} \tag{4.8}$$

where τ_o is the pre-exponential factor which is taken to be 10^{-12} sec [175] and ΔH_{ads} is the energy of adsorption. Using the adsorption energy calculated from the xenon isotherms, 4.2 Kcal/mole, it is calculated that the sticking times range from $\approx 10^{-9}$ s at room temperature to $\approx 10^{-5}$ s at 130 K. The chemical shift extrapolated to zero pressure can thus be fit to a function of the form of equation (6) where P_s is given by

$$P_s = \frac{\tau_o e^{\Delta H_{ads}/kT}}{\tau_v + \tau_o e^{\Delta H_{ads}/kT}} \tag{4.9}$$

by substituting equation (4.8) into equation (4.7). Although it is not possible to separate the variables τ_o and τ_v in the fit, with $\Delta H_{ads} = 4.2$ Kcal/mole and choosing $\tau_o = 10^{-12}$, it is determined that $\delta_s = 95$ ppm and $\tau_v = 3 \times 10^{-8}$ s. The chemical shift intercept data fitted to equation (4.9) are given in Figure 4.6. The contribution to the chemical shift due to the xenon-surface interaction is therefore 95 ppm, a value somewhat larger than 86 ppm measured for xenon in NaY zeolite at 144 K.[176] In view of the much smaller heat of adsorption of xenon on the polymer as compared to a zeolite, this large value for δ_s is surprising. However for NaY δ_s increases from 58 ppm at room temperature, to 86 ppm at 144 K, the only low temperature measured, so it may increase further at even lower temperatures. In addition, it is difficult to compare our results for the xenon/polymer system to the small body of low temperature xenon shift data which has been measured for porous materials since the xenon shift is also highly sensitive to the morphology of the sample. Several studies have shown that a large value for δ_s on a sample with a small heat of adsorption can be due to the surface structure. For example, Cheung found that although the adsorption sites in the amorphous silica-alumina mixtures [177] are much weaker than in NaY zeolite, the zero pressure xenon shifts are much larger, greater than 120 ppm at

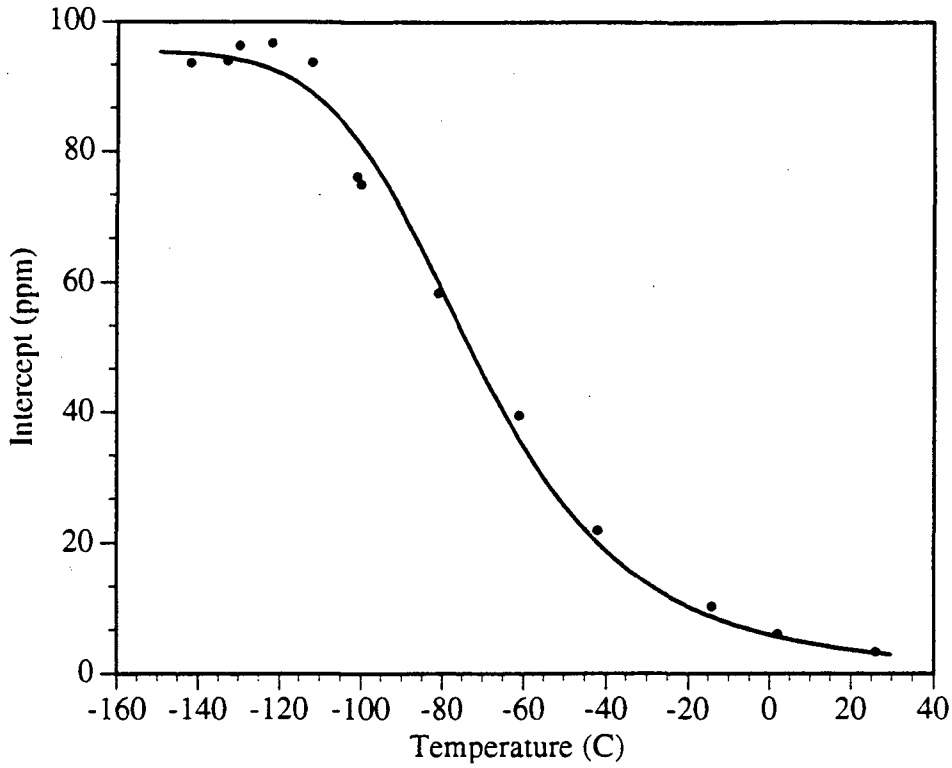

Figure 4.6 ^{129}Xe chemical shift intercepts, δ_S (ppm) versus temperature. The solid line is the fit to the data using equation (4.9) described in the text.

144K. This behavior may be due to a broad distribution of micropores in these amorphous samples and the fact that the ^{129}Xe chemical shift is inversely proportional to the pore size. Fraissard and co-workers obtained similarly large xenon shifts for a material consisting of agglomerated silica spheres [178] although the pores sizes are an order of magnitude larger than those in zeolites. In this case, the large chemical shifts are attributed to rapid exchange between the inter-porous xenon atoms and xenon adsorbed into confined spaces at the points of contact between the silica spheres. From the observed BET behavior of the xenon isotherms on poly(acrylic acid), it is surmised that this polycrystalline polymer is not microporous like amorphous silica. Thus the chemical shift is due to xenon interacting with surface functional groups, however, the possible existence of some type of surface microstructure cannot be completely ruled out as responsible for the relatively large xenon shift at low coverages.

The ^{129}Xe NMR data also contains information about diffusion of xenon on the surface. This is extracted from the coverage dependence of the adsorbed xenon chemical shift which arises from the xenon-xenon interactions at the polymer surface as given by the second term in the virial expansion (4.4). Taking the derivative of equation (4.4) gives

$$\frac{d\delta}{d\theta} = P_S^2 \sigma_{1s}(T), \tag{4.10}$$

which is the slope of our chemical shift data (Figure 4.5). As an approximation, $\sigma_{1S}(T)$ can be related to the second viral coefficient of the nuclear shielding, $\sigma_1(T)$, as defined by Jameson, [174] which determines the contribution to the gas phase shift due to Xe-Xe collisions. For all gases, $\sigma_1(T)$ has been found to have the same sign since the gas phase intermolecular interactions always result in a net deshielding of the nucleus. In xenon, however, this parameter is unusually large, ranging from 0.75 to 0.1665 ppm/amagat between 240 K and 440 K. These values must be extrapolated down to our temperature range, about 130 K. In order to relate the gas phase Xe-Xe interactions to a surface interaction, it will be assumed that the nature of the pair-wise collisions is not greatly

changed by the presence of a surface. This of course is not strictly correct (in fact, the possibility of forming Xe-Xe bonds on a strongly adsorbing surface, palladium metal, has even been explored theoretically) but it is reasonable to assume that a weakly adsorbing surface such as a polymer will not greatly perturb the xenon-xenon interactions. However, the contribution to the shift due to the xenon-xenon interactions also depends on the collision *rate*, which will be very different on a surface. In the gas phase, the collision rate is given by

$$\frac{1}{\tau_c} = [\mathrm{Xe}]\sigma_{\mathrm{Xe}}\bar{v}_g = \frac{\bar{v}_g^{\,2}}{3D_g} \tag{4.11}$$

where [Xe] is the xenon concentration, $\bar{v}_g$ is the average relative velocity, σ_{Xe} is the binary collision cross section (23 Å^2 for xenon), and D_g is the gas diffusion constant. The average relative velocity is $\bar{v}_g = \sqrt{16kT/\pi m}$. On a surface, a similar expression is given for the collision rate

$$\frac{1}{\tau_{sc}} = \theta\sigma_s\bar{v}_s = \frac{\bar{v}_s^{\,2}}{2D_s} \tag{4.12}$$

where θ is the coverage, D_S is the surface diffusion constant, $\bar{v}_s^2$ is the surface velocity, and the units of θ and σ_s are now cm^{-2} and cm. Since at monolayer coverages there will be two-dimensional diffusion on the surface, the constant is 1/2 instead of 1/3 in the expression for $1/\tau_{sc}$. With the assumption that the xenon-xenon interactions only differ due to the collision rates in the two phases, the known gas phase coefficient is scaled by the ratio of the two rates

$$\sigma_{1s}(T) = \sigma_1(T)\frac{\tau_c}{\tau_{sc}} \tag{4.13}$$

The equation for the coverage dependence of the adsorbed xenon chemical shift can now be rewritten using equations (11) and (12) for the collision rates

$$\frac{d\delta}{d\theta} = P_S^2\sigma_{1s}(T) = P_S^2\sigma_1(T)\frac{2\theta^2\sigma_s^2D_s}{[\mathrm{Xe}]\sigma_{\mathrm{Xe}}\bar{v}_g}. \tag{4.14}$$

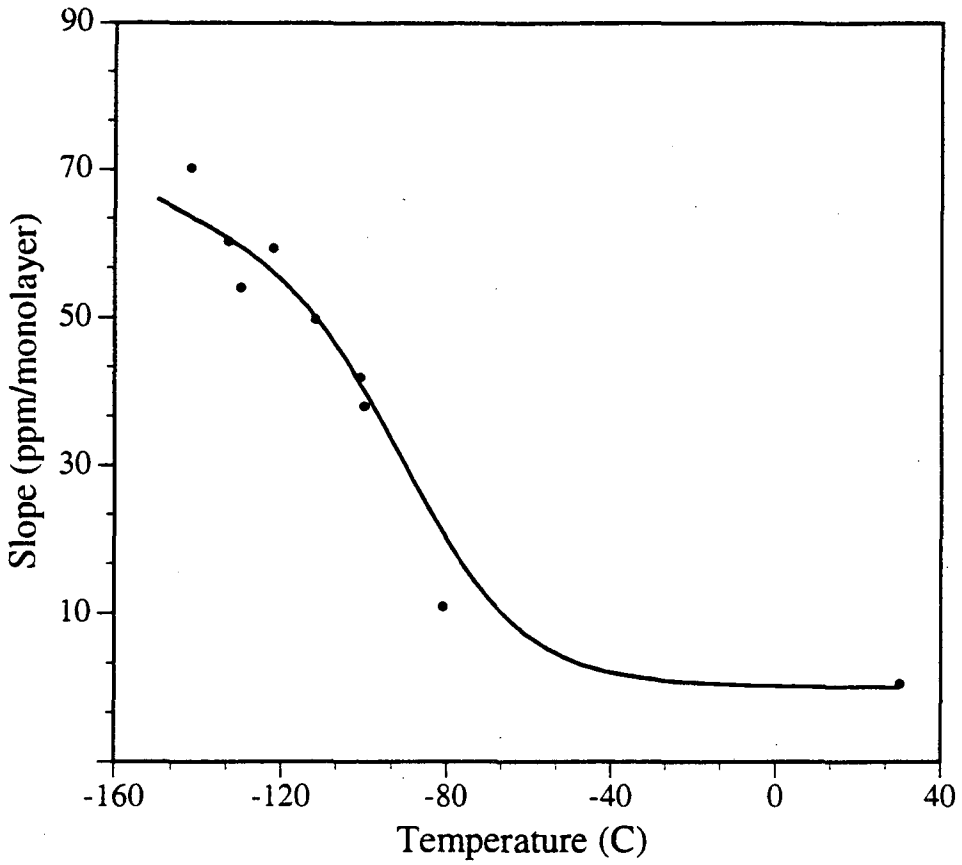

Figure 4.7 ^{129}Xe chemical shift slope (ppm/monolayer) versus temperature fitted to the data using equation (4.14).

The chemical shift slope data of Figure 4.5 can be fit to this expression in order to extract a value for the diffusion coefficient. The coverage, θ, on the right side of equation (4.14) is a constant, not a variable since $\sigma_1(T)$ is determined at a constant pressure. D_S will be evaluated at a coverage of 1 monolayer, so that $\theta = 1/23$ Å^2. All of the parameters in equation (14) are known, with the exception of P_S, which is found from a fit to the chemical shift intercepts in Figure 4.6, and $\sigma_1(T)$ which is extrapolated from the gas phase data in reference [174], and D_S which is to be determined.

The xenon chemical shift slopes fit to equation (4.14) are presented in figure 4.7. Although there is some scatter, it is apparent that a simple linear fit would be inadequate to describe the data. The pressure dependence should tend to zero at the higher temperatures where the xenon spends little time at the polymer surface and the slope should be merely the room temperature value of the second viral coefficient, 0.548 ppm/amagat. By substituting in values for σ_S (8.8 Å) and θ (1/23 Å^2), the value of D_S is found to be 3.3 x 10^{-5} cm^{2}s^{-1}.

By including a second parameter into the fit, an Arrhenius form,

$$D(T) = D_0 e^{(-E_{diff}/kT)} \qquad (4.15)$$

the temperature dependent diffusion coefficient could be determined. However, the quality of the fits did not allow us to determine E_{diff}. This probably due both to the fact that there was already an exponential temperature dependence in the fit of the chemical shift slopes as well as an underestimate of the second viral coefficient of the nuclear shielding, at lower temperatures where the data of Jameson et al. had to be extrapolated more than 100 °C. In light of the small energy of adsorption for xenon on the polymer, however, the temperature dependence of the diffusion may be relatively small. In general E_{diff} is expected to be 10-20 % of the adsorption energy, [175] which is 4.2 Kcal/mol for xenon on poly(acrylic acid) and would lead to a decrease of the diffusion constant only by a factor of two over the temperature range studied. It is also worth noting that the value of D_S calculated from this

method is comparable to the diffusion coefficients of methane and neopentane on graphitized carbon measured by pulsed linear field gradient methods [179]. For example, at a coverage of one monolayer at 85 K , $D_S = 5 \pm 2 \times 10^{-5}$ cm^2/s for methane on graphitized carbon black and $D_S = 3.0 \pm 0.5 \times 10^{-5}$ cm^2/s at 228 K for neopentane at a coverage of 1.25 monolayer on the same substrate [180].

4.5 Summary

The chemical shift extrapolated to zero coverage indicates a surprisingly strong interaction between xenon and poly(acrylic acid), which may be due to the polar carboxylic acid functional groups at the polymer surface. These chemical shifts are less than those observed for xenon occluded into polymers such as polyethylene (198 ppm) [39] or in polymer blends (192 - 215 ppm) [181]. The dynamical parameters extracted from our analysis of the chemical shift behavior of xenon in contact with poly(acrylic acid) indicate that the xenon is still highly mobile on the polymer surface at the lowest temperatures measured. The diffusion constant estimated for xenon on poly(acrylic acid) is similar to that of small molecules on graphite. From the value of the diffusion coefficient and assuming Fick's law, the translational correlation time τ_t is of the order $\approx 10^{-10}$ sec. The efficiency of cross polarization deteriorates with increasing molecular motion. In a theoretical study of the effect of molecular motion on ^1H - ^{13}C cross polarization, Schulze et al. [182] found that the efficiency of magnetization transfer decreases dramatically for motional correlation times shorter than ~ 10^{-5} sec. Thus the data indicates that lower temperatures will be necessary before cross polarization experiments between the polarized xenon and the surface spins can be attempted on this system.

4.6 PAN and other Polymers

Experiments analogous to those for poly(acrylic acid) were carried out on poly(acrylonitrile), which has a very polar sidegroup. The surface area of the powdered polymer obtained by nitrogen BET isotherm analysis is 6.9 m^2/g, but after sieving through a 300 mesh (0.0018" opening) sieve, it increased to 18.2 m^2/g. The heat of adsorption for xenon was 3.96 kcal/mole, similar to poly(acrylic acid). The results of the chemical shift versus temperature study are shown in figure 4.8a. Transforming from pressure to coverage through the use of BET isotherm data leads to the plot in figure 4.8b. The results are quite intriguing - the intrinsic chemical shift is much larger than poly(acrylic acid), 120 ppm vs. 95 ppm. On the assumption that the morphology of the surface is similar in these two systems (admittedly, a completely untested assumption) the larger chemical shift could be due to the much larger polarity of the cyano group vs. the carboxylic acid functional group.

Further partial studies of poly(vinyl chloride), poly(vinylidene fluoride), polypropylene, and Teflon were also undertaken. The intrinsic chemical shift of the xenon on the surface could be determined from the pressure data and no further analysis was done. Some of this data is shown in figure 4.9 and the chemical shift results are summarized in table 4.2.

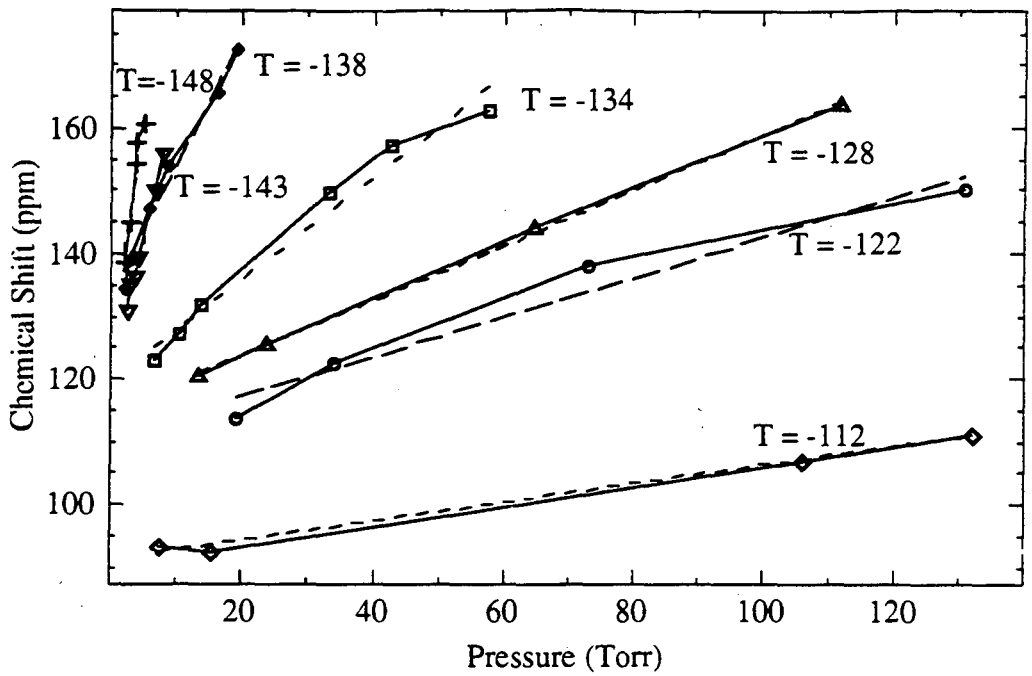

a)

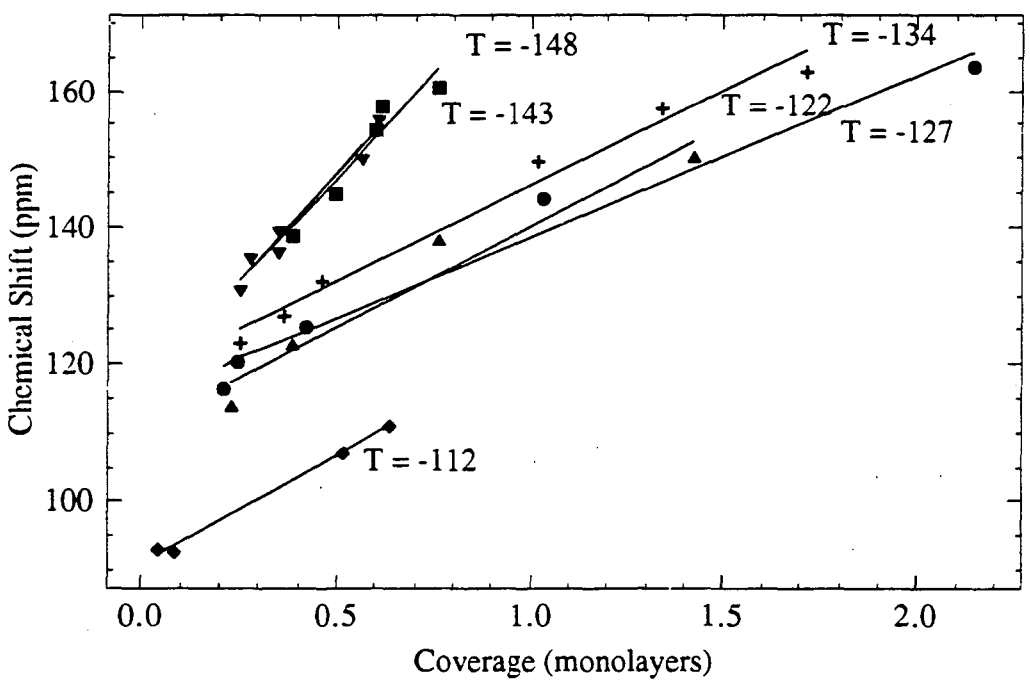

b)

Figure 4.8 Summary of chemical shift study of xenon on poly(acrylonitrile). (a) Chemical shift as a function of the measured parameters. (b) Chemical shift vs. coverage. Both show least squares fits to the data.

a)

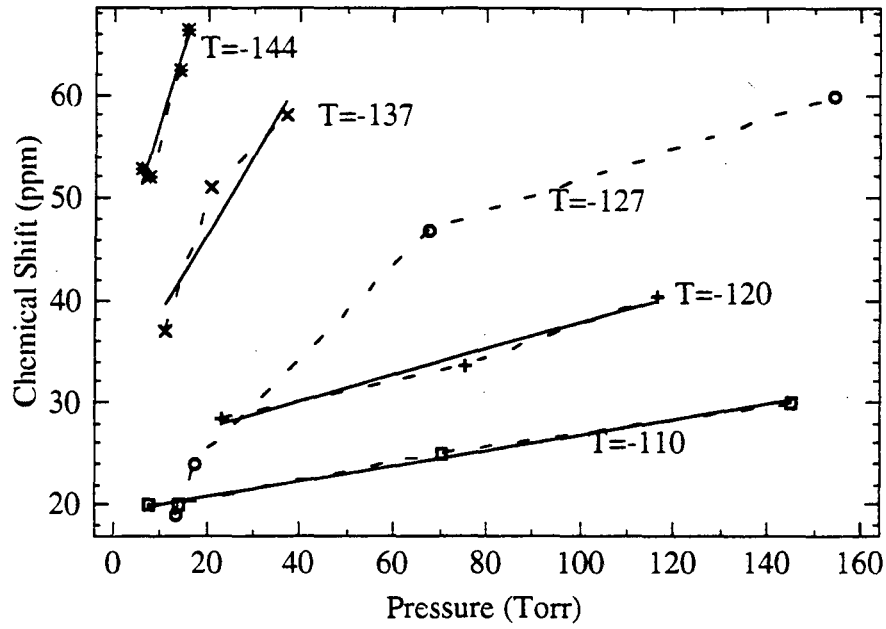

b)

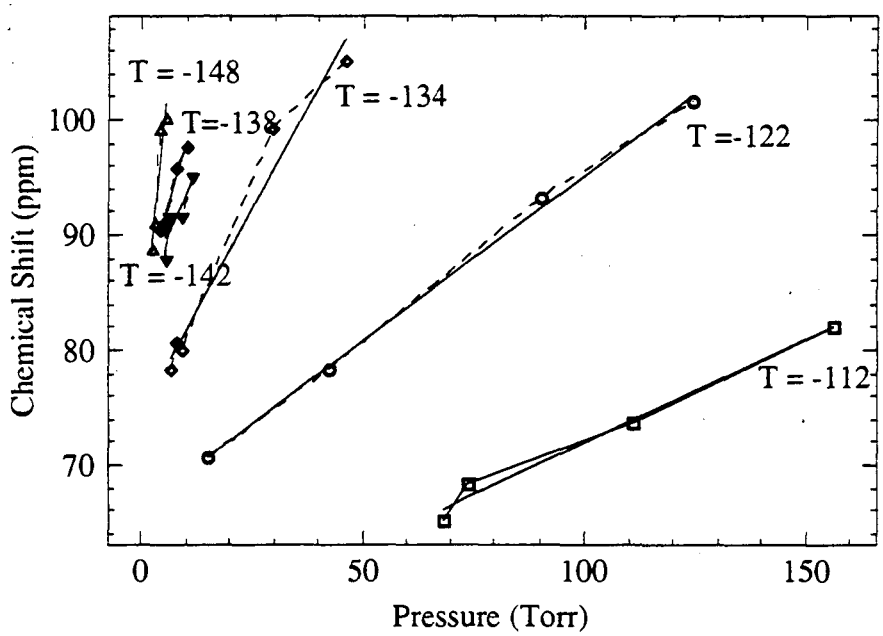

Figure 4.9 Summary of chemical shift study of xenon on a) Teflon {poly(tetrafluoro ethylene)} and b) poly(vinylidene fluoride).

Polymer	BET Surface Area (m^2/g)	Chemical Shift (ppm)
poly(acrylic acid) PAA	16.0	95
poly(acrylonitrile) PAN	18.2	120
poly(vinyl chloride) PVC	6	25
poly(vinylidene fluoride)	15.4	78
Teflon	8*	>50

*DuPont product information

Table 4.2 Summary of xenon chemical shifts on selected polymers

Several polymers with simple structures such as polyethylene could not be studied due to short xenon spin-lattice relaxation times or the inability to obtain the polymer in finely powdered form. The results are sketchy, however, this work represents the first tenuous step towards being able to empirically correlate the chemical shift of adsorbed xenon with the chemical entities exposed on polymer surfaces.

4.7 Studies of Poly(triarylcarbinol) "White Carbon Black"

This polymer was recently synthesized at DuPont by Owen Webster and co-workers [183]. It has the amazing property of possessing a surface area around 1000 m^2/g which is unprecedented in an organic system. As it is characteristically white in appearance and yet has the surface area of carbon black (activated charcoal), it has been referred to by its synthesizers as "White Carbon Black" (WCB). The chemical structure is shown in figure 4.10. It is a rigid-rod polymer that is hypercrosslinked (one cross link for every monomer unit). While it is microporous like a zeolite, it is amorphous and thus has a broad distribution of pore sizes, with an average of ≈30Å as determined by mercury porisometry

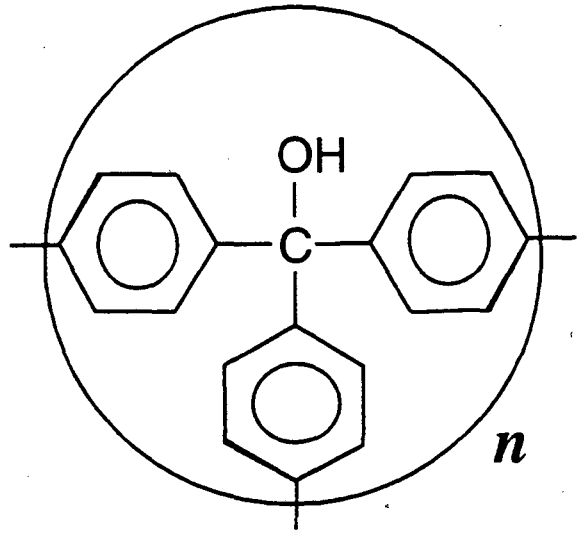

Poly(triarylcarbinol)

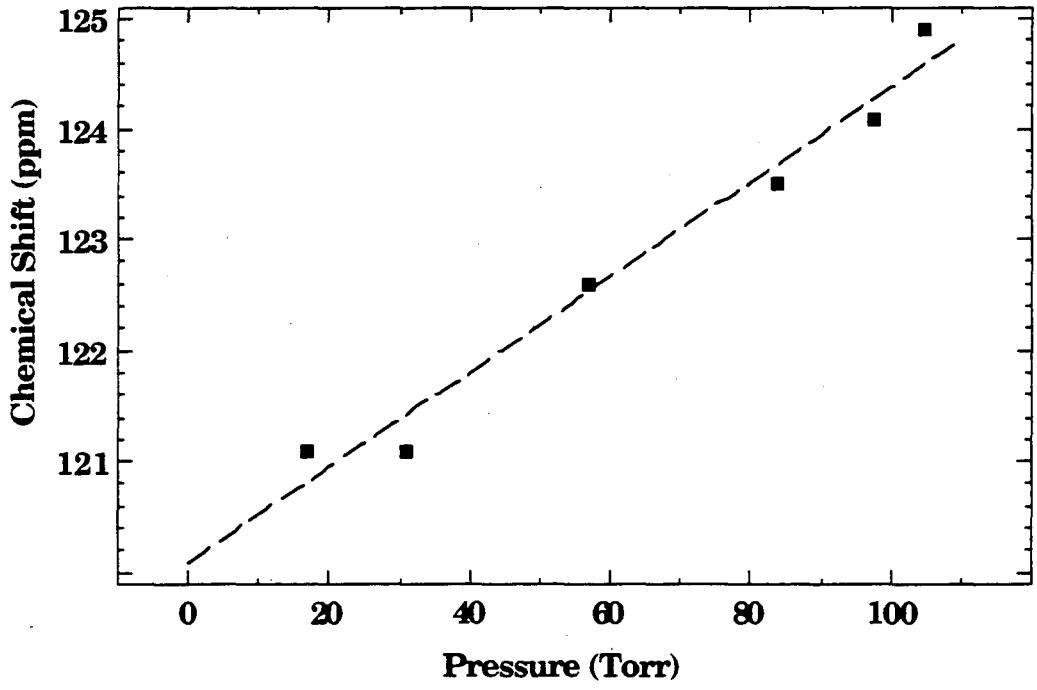

Figure 4.10 Structure and xenon chemical shift in poly(triarylcarbinol).

(F. Gentry personal communication). Xenon is much more sensitive than porisometry measurements to small pores. A simple pressure vs. chemical shift experiment was done at room temperature which is shown in figure 4.10. The intercept is 120.1 ppm, indicative of fairly small cages according to empirical correlations which have been developed, although one must be very cautious in using these types of correlations [184]. The pressure dependence is linear up to about 600 torr where it begins to show some curvature, in contrast to the strictly linear behavior seen in most zeolites (with monovalent cations).

In a sealed sample with about 2 atmospheres of xenon the line width at room temperature is only 300 Hz, showing the xenon to be highly mobile. Upon cooling the chemical shift varies only slightly increasing to 149 ppm at 95K, but the line width increases dramatically below -130°C reaching 4.5 kHz at 95K (figure 4.11). Here the motion of the xenon is clearly being quenched. In this regime it is clear that the xenon is not rapidly averaging over many cages and thus may be expected to have a non zero average coupling with the protons in the pore where it is trapped. Decoupling experiments showed no apparent narrowing of the line width and so much of the broadening is due to a distribution of chemical shifts. Nonetheless proton to xenon cross polarization experiments were successful. The cross polarized xenon spectra showed the characteristic exponential growth due to polarization transfer followed by the exponential decay due to spin-lattice relaxation of protons in the rotating frame (figure 4.12). The optimum transfer time was determined to be 5 msec at -168°C.

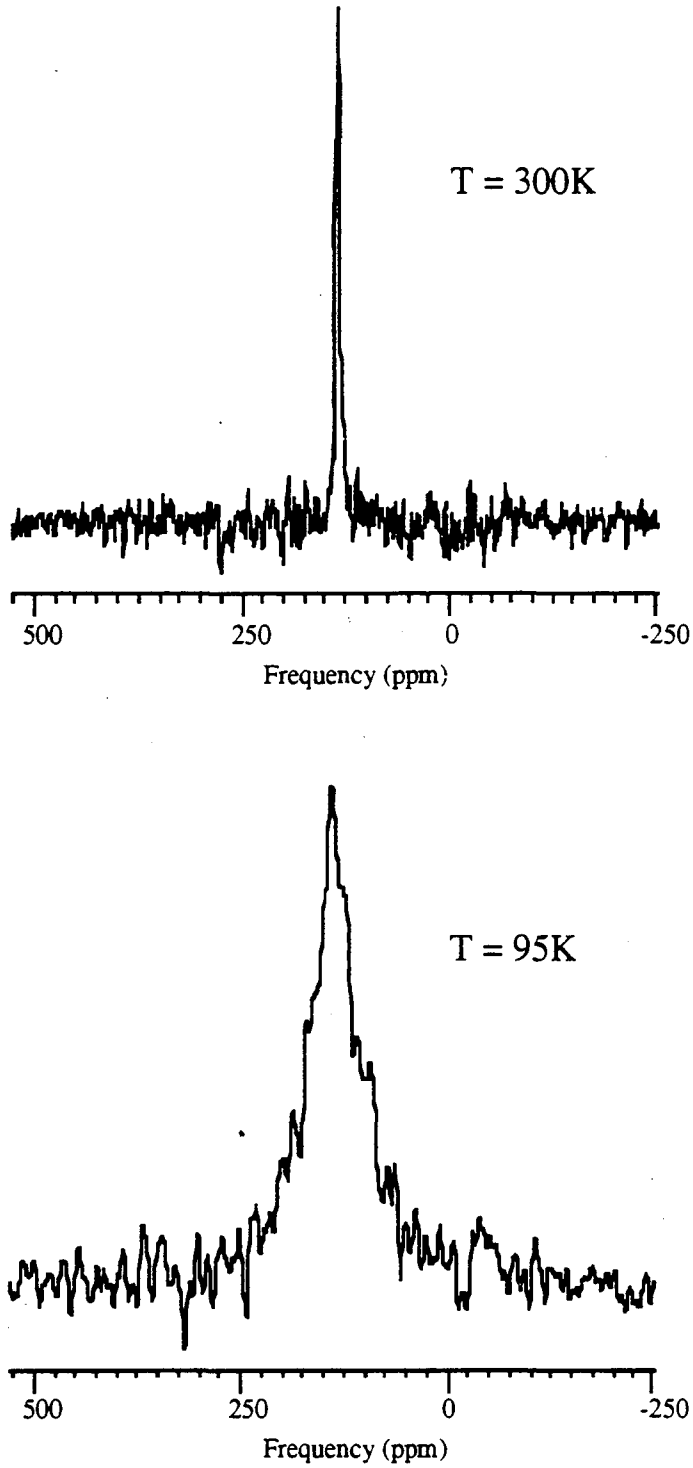

Figure 4.11 Xenon spectra in a sealed sample of WCB at (a) 300K (Line width=300Hz) and (b) 95K (Line width=4500 Hz).

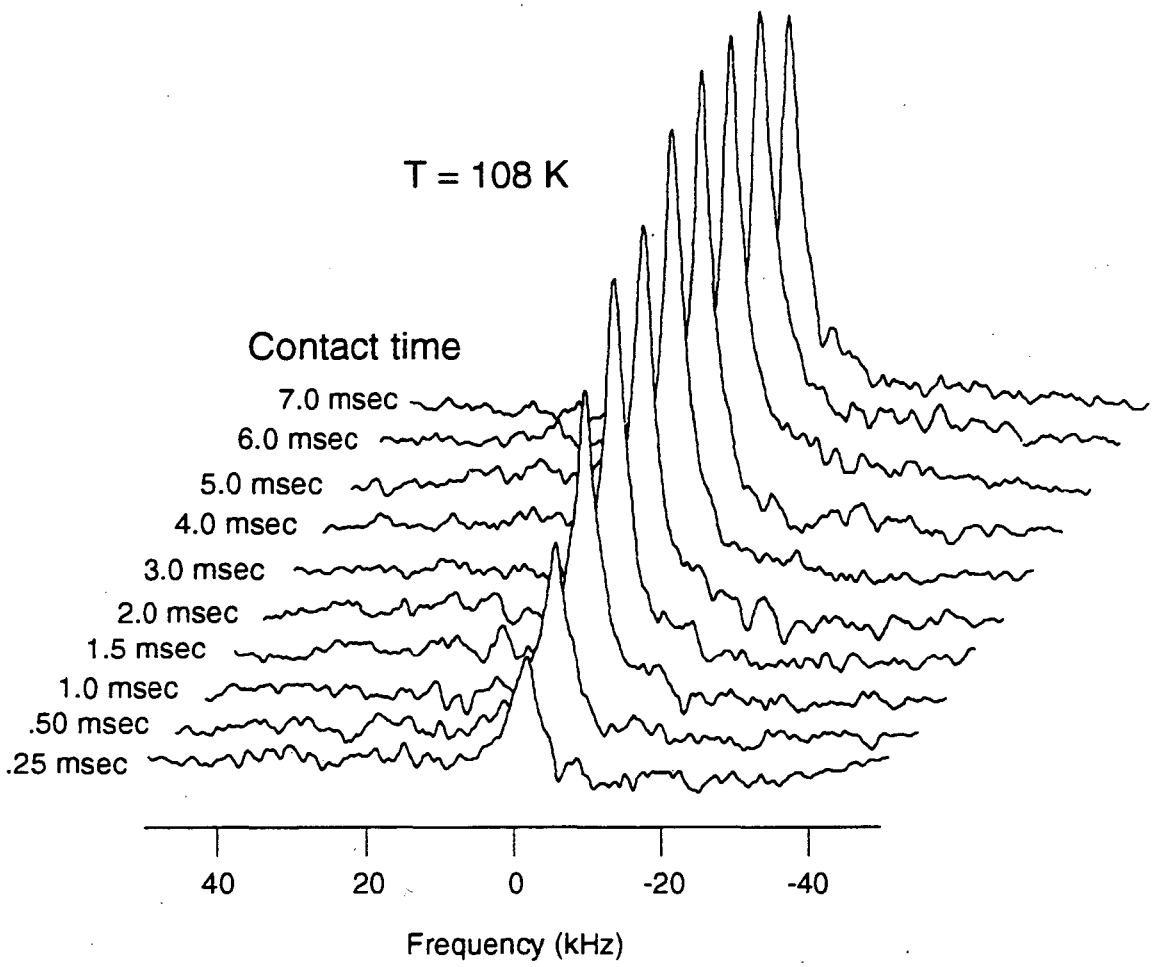

Figure 4.12 Xenon cross polarization spectra in WCB (sealed sample) as a function of contact time.

The sealed sample in all of the above studies was slowly cooled in the probe (typical cooling rates were 0.2°/second below -100°C) and allowed to equilibrate for 5 minutes or more at the final temperature. When optical pumping experiments were started on this material the xenon was introduced quickly at the final temperature and the spectra acquired a few seconds later. The first such experiments showed a line with a chemical shift much larger than that shown in figure 4.13 below. Eventually a procedure was adopted of loading some xenon at room temperature and adding the rest at the final temperature before performing conventional xenon NMR experiments. This lead to spectra with *two* peaks, one around 150 ppm (the "equilibrium sites") and another at a higher, temperature dependent, chemical shift,(the "nonequilibrium sites"). When the xenon was added at the coldest temperature and allowed to warm slowly, the high frequency peak moved over to eventually coalesce with the low frequency peak at -120°C as shown in figure 4.13. This coalescence was found to be *irreversible*, i.e. recooling the sample did not result in the return of a second peak.

It was found that both peaks could be cross polarized from the protons with the optimum contact time the same for the two sites. Thus the average dipolar coupling must be the same if the proton $T_{1\rho}$ is assumed to be homogeneous within the sample. The T_1 data for the xenon, however, showed a very distinct difference (figure 4.14). A quantitative fit to the integrated areas of the peaks (figure 4.15) shows that the low frequency (equilibrium) peak relaxes with a time constant almost twice as long (24.0 s) as the high frequency (equilibrium) peak (12.5 s). From the fact that the optimum contact times with protons are the same one is lead to believe that the heteronuclear dipolar coupling is not the primary cause of relaxation, leaving fluctuating chemical shift anisotropy as the most likely source.

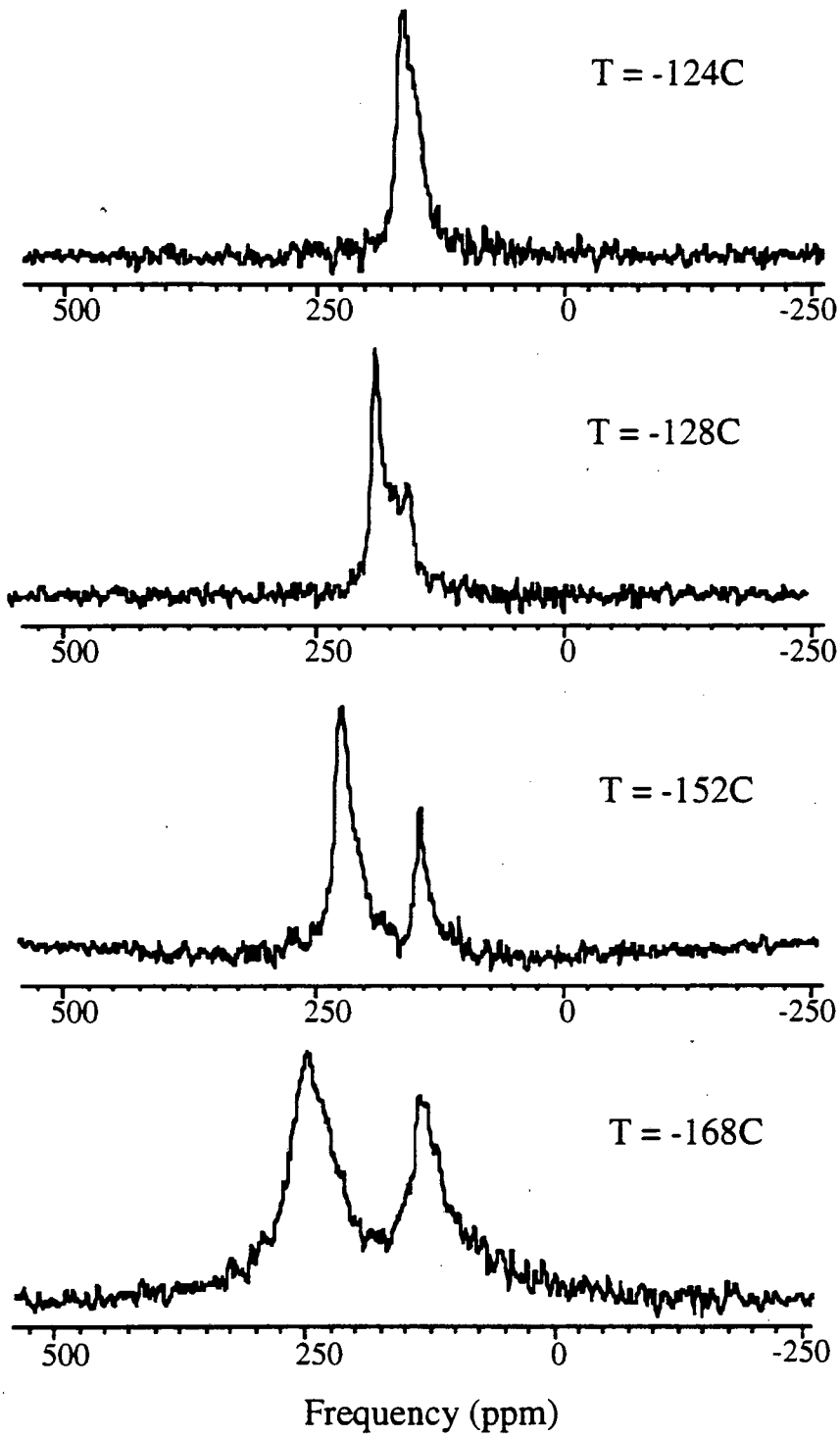

Figure 4.13 Two-site xenon spectra in WCB at various temperatures.

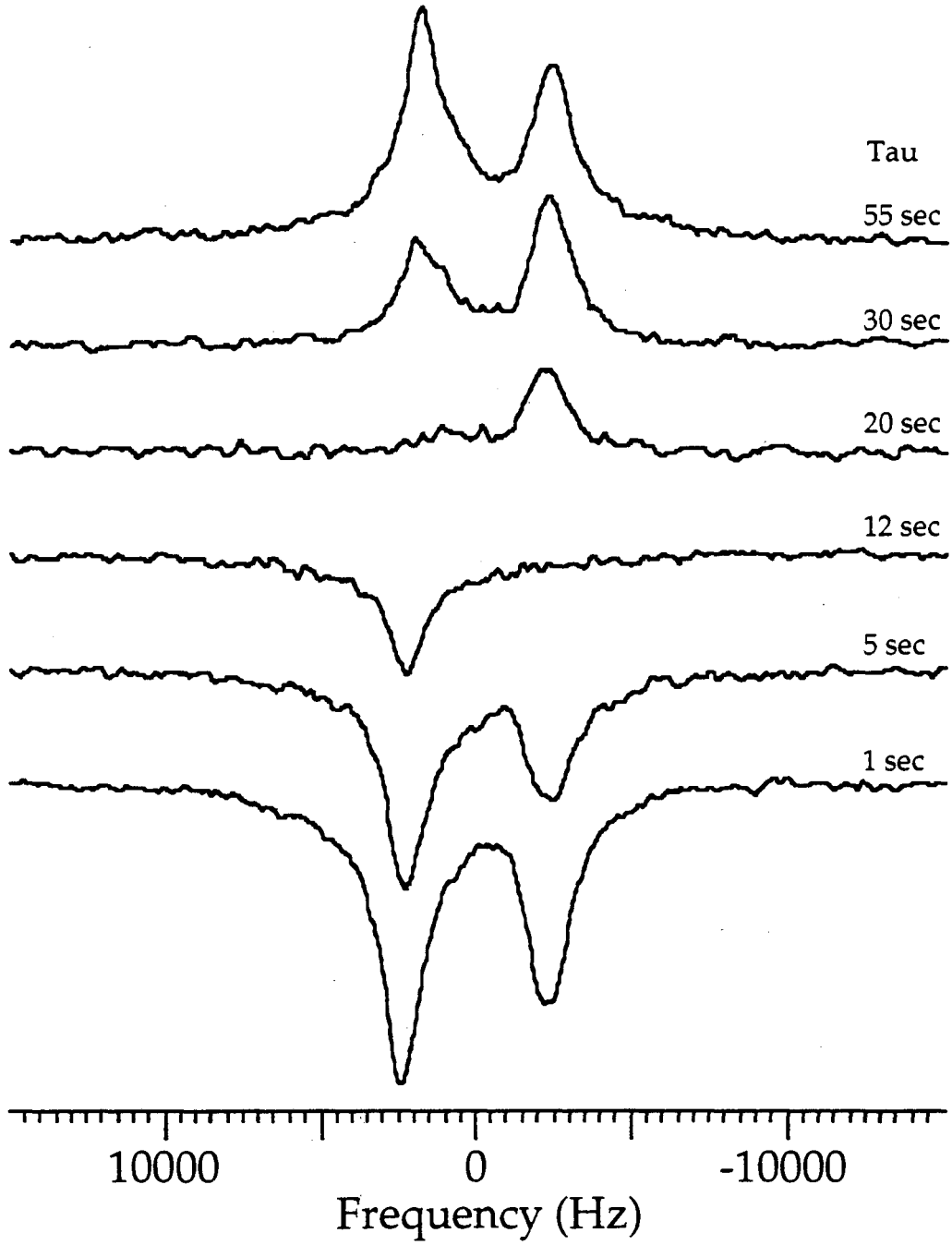

Figure 4.14 Representative spectra of inversion-recovery xenon T_1 measurement in WCB at -168 °C.

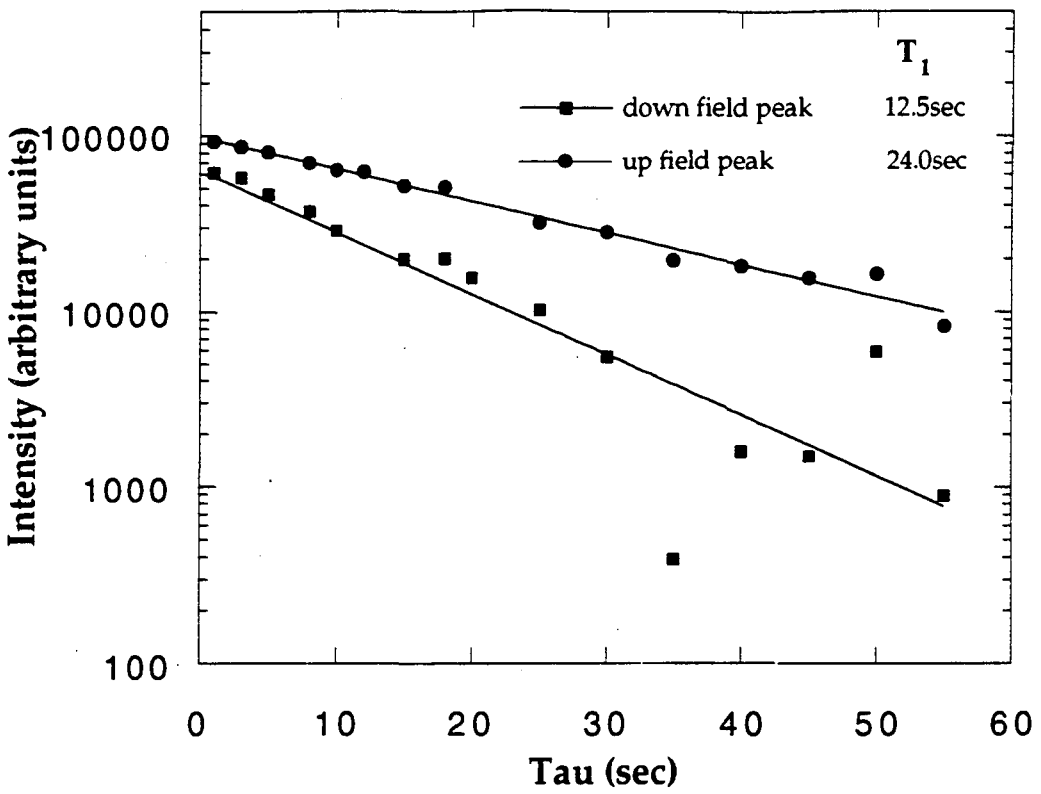

Figure 4.15 Fits to the xenon inversion-recovery measurements.

A tentative model of the WCB to consistent with all of this behavior is now presented. A distribution of pore sizes undoubtedly exist inside this material. Within a given material it is clear that the chemical shift of xenon is inversely proportional to pore size and thus the high frequency peak corresponds to smaller pores. Since it appears that these are not the thermodynamically favored binding sites the xenon apparently becomes kinetically trapped at these sites when introduced to the polymer at low temperatures. This may indicate a high proportion of small pores near the surface of the particles. As the polymer is warmed the increasing thermal energy of the xenon allows it to diffuse slowly through a series of quasi-equilibrium sites of gradually larger pore size until it reaches the equilibrium sites. Why the distribution should remain sharp during this process is not at all clear and this question can only be addressed through further studies involving well characterized changes in the structure of the polymer itself. A study such as this with

different surface areas of WCB, or structural modifications, would be the most straightforward way to accomplish this.

Finally, the experimental fact that the xenon is in dipolar contact with the protons even when it is introduced rapidly at low temperatures is quite useful. These are the conditions under which the optical pumping experiments are done. By the principle of microscopic reversibility, if the polarization can transfer in one direction it can transfer in the other direction -- if the temperatures of the two spin systems are appropriate. Since the laser polarized xenon is at a spin temperature of about 3mK (as shown in chapter 3) it can enhance the polarization of any nucleus that it can exchange energy with under normal conditions. This idea will be explored in detail in the next chapter.

CHAPTER 5 Polarization Transfer Experiments using Laser Polarized Xenon

5.1 Introduction

Polarization transfer is ubiquitous in NMR. From pulsed coherence transfer sequences in liquids to low temperature dynamic nuclear polarization, techniques that involve a transfer of spin order have benefited NMR in many ways. A simple yet powerful demonstration of sensitivity improvement involving proton to xenon magnetization transfer is shown in figure 5.1. This clathrate compound was originally studied using ^{129}Xe NMR by Ripmeester [33]. Figure 5.1a shows the simple ^{129}Xe pulse-acquire spectrum that must be recycled at the T_1 of xenon, which is 12 minutes in this compound at room temperature. A dramatic enhancement is apparent in figure 5.1b, obtained with an adiabatic cross polarization sequence and ^1H decoupling. This spectrum shows higher signal-to-noise after much *less* acquisition time (8 minutes vs. 8 hours!) since it is recycled at the T_1 of the proton spins (1 minute). Clearly a great advantage exists when the spin species of interest has a long spin-lattice relaxation time or a low concentration.

There is another important feature of polarization transfer experiments. If the polarization can be transferred from one species to another there must exist a coupling between the two species, and therefore they must be in close spatial proximity on a molecular level. This fact has been exploited by several workers studying surfaces and

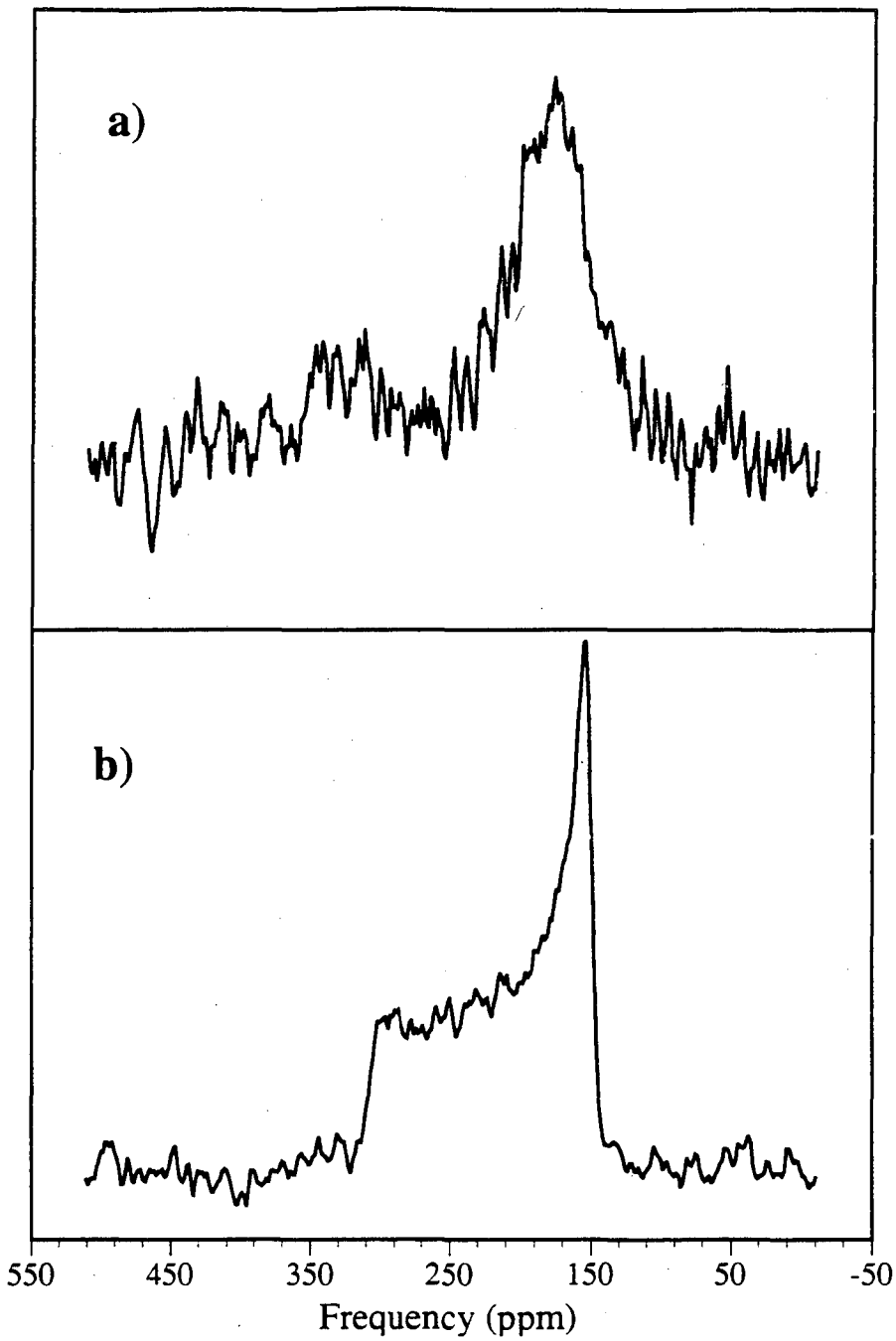

Figure 5.1 (a) Repetitive pulse-acquire ^{129}Xe spectra of Xe/β-quinol clathrate. NA=40, PD=12 min. (b) Adiabatic cross polarization spectrum of xenon with proton decoupling. NA=8, PD=1 min.

interfaces to discriminate against bulk nuclei. Maciel and co-workers have used surface hydroxyls on various Aerosils to cross polarize selectively to ^{29}Si at the surface [185]; in combination with magic angle spinning several sites have been identified that are distinct from the bulk. Walters, Turner and Oldfield [186] have studied surface hydroxyls performing cross polarization to ^{17}O and measuring strength of the quadrupolar interaction. Zumbulyadis and O'Reilley have examined a polymer-silica sol-gel interface by measuring the dynamics of polarization transfer from ^{1}H on poly(vinyl alcohol) to ^{29}Si nuclei [187]. Dynamic nuclear polarization has also been used to selectively enhance nuclei at polymer interfaces [188].

Several transfer schemes will be discussed in this chapter with an emphasis on their potential utility with laser polarized xenon. There are several complications that the optical pumping experiment imposes since xenon is polarized in the gas phase and must be subsequently brought into contact with the sample. Although a single monolayer of adsorbed xenon formed in the polymer experiments in the last chapter (cf. figure 4.5), the xenon was highly mobile on those surfaces at the temperatures studied. Simply lowering the temperature resulted in the formation of bulk frozen xenon where most of the spins are not in close contact with the surface. Several schemes were attempted involving buffer gases and/or rapid temperature jumps to induce the xenon into an immobile state on the surface, but were unsuccessful. At present this is the most severe limitation on using laser polarized xenon as a magnetization source. The actual experimental results discussed below represent particular systems where his problem could be overcome.

Assuming the appropriate coupling is present, one must then match the energy levels of xenon with the target nucleus to allow rapid equilibration of the two spin systems. This is not a requirement for all experiments (such as polarization transfer through the dipolar reservoir which only requires adiabatic demagnetization/remagnetization), however, it provides a convenient framework for the following discussion of polarization transfer experiments.

5.2 Thermal Mixing in Low Field

The simplest possible scheme for matching the energy levels of xenon with another nucleus is simply to remove the external magnetic field. In this state the Zeeman interaction that differentiates between the spins is absent and all the spins can mix via the dipolar interaction and will reach a common spin temperature [13, 189]. If the external field can be reapplied before spin-lattice relaxation destroys the polarization, the spins coupled to the xenon will be observed with high sensitivity. This section will demonstrate the use of this effect using ^{13}C labeled carbon dioxide occluded in frozen laser polarized xenon.

5.2.1 Theory

The theory can be described using a simple density matrix treatment following Goldman [13]. Initially the ^{129}Xe (the I spin) and the ^{13}C (the S spin) are at a field strength much larger than the local dipolar field and the density matrix of the system is given by

$$\rho_{initial} = \alpha\omega_I I_Z + \delta\omega_S S_Z. \tag{5.1}$$

Here the two spin systems are initially at different (inverse) spin temperatures, α and δ, since the CO_2 is at the lattice temperature and the xenon is prepared by optical pumping at a spin temperature of a few millikelvin (cf. section 3.1.1). The dipolar couplings have been neglected in the density matrix since the polarization transfer can occur at a field strength much larger than the local fields (demonstrated below) where the heat capacity of the dipolar couplings can be neglected compared to the heat capacity of the Zeeman terms [189]. During the time that the external field is low enough for overlap of the resonance lines of the two spin systems, they evolve towards a common spin temperature. The system reaches a final density matrix of the form βH:

$$\rho_{final} = \beta(\omega_I I_Z + \omega_S S_Z). \tag{5.2}$$

β is determined by conservation of energy. The system evolves at constant energy (assuming the time is short compared to the relevant T_1's) which may be expressed as

$$Tr(\rho_{initial}H) = Tr(\rho_{final}H) = \beta Tr(H^2). \tag{5.3}$$

Solving this for β results in

$$\beta = \frac{Tr(\rho_{initial}H)}{Tr(H^2)} = \frac{\alpha\omega_I^2 N_I I(I+1) + \delta\omega_S^2 N_S S(S+1)}{\omega_I^2 N_I I(I+1) + \omega_S^2 N_S S(S+1)}. \tag{5.4}$$

(The traces are easily evaluated by noting that all traces linear in either I_Z or S_Z are zero.) This can be concisely rewritten by dividing through by the first term in the denominator leaving an expression involving only the initial spin temperatures of the two systems and the ratio

$$\mu = \gamma_S^2 N_S S(S+1) / \gamma_I^2 N_I I(I+1), \tag{5.5}$$

which is the ratio of the heat capacities of the two spin systems. The final spin temperature is therefore

$$\beta = \frac{\alpha + \delta\mu}{1+\mu}. \tag{5.6}$$

In the current experiment the initial condition of the S spins (^{13}C) was essentially zero polarization (infinite spin temperature), δ=0, and the ratio of heat capacities is μ=1.2 for a solid mixture containing equal numbers of ^{129}Xe and ^{13}C nuclei in dipolar contact. Thus equation 5.6 predicts β≈α/2.2, or that the final magnetization of the ^{13}C spins is related to the initial ^{129}Xe magnetization by just $M_C^f = M_{Xe}^i / 2.2$.

5.2.2 Experimental

The low field glassware described in section 3.1 is mounted on a laser table in the same room as the superconducting magnet. It is slightly modified by connecting it to an L-shaped NMR sample tube located inside a pair of Helmholtz coils. The experimental timing sequence is shown in figure 5.2. Approximately 2000 torr cc of enriched (80%) xenon gas

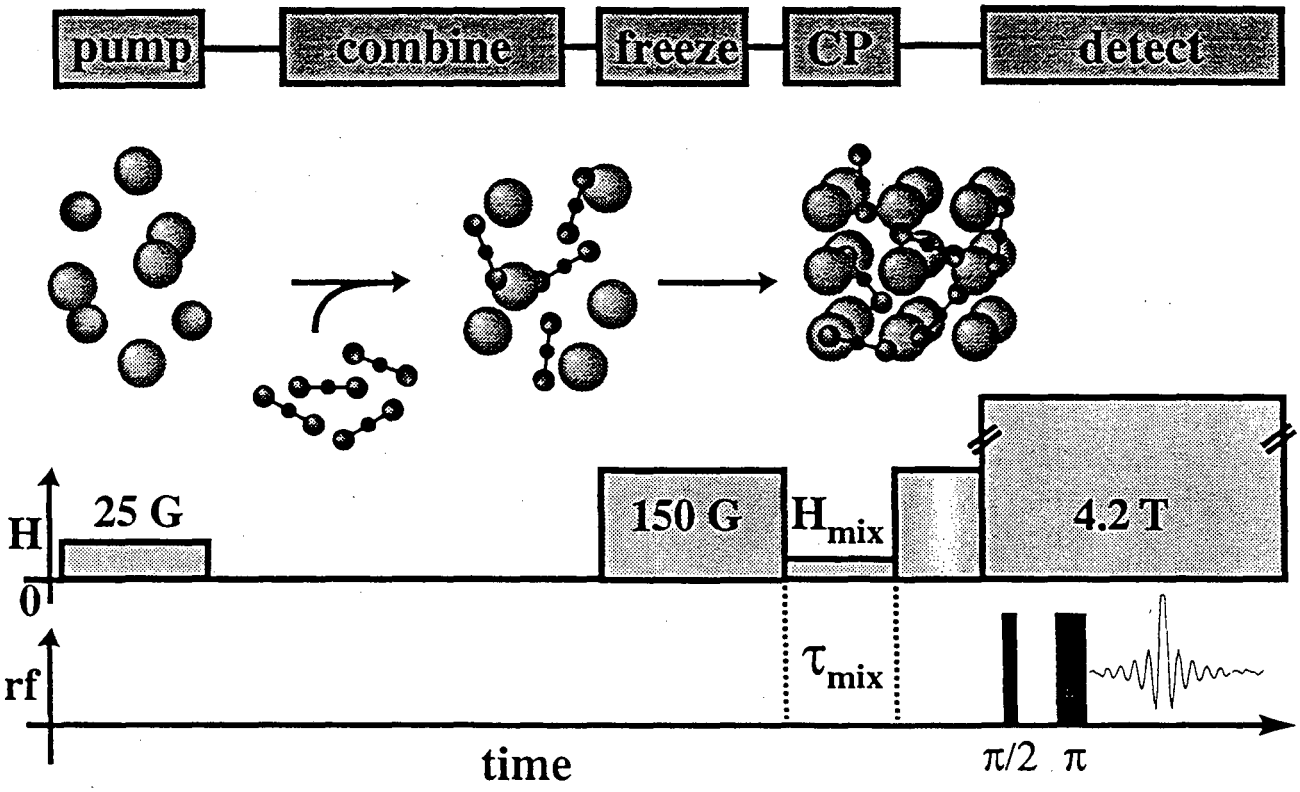

Figure 5.2 Timing diagram for low field mixing experiment.

is pumped at 105 °C in a magnetic field of 25 G. The enriched gas is especially important in this experiment as it contains only 1.3% ^{131}Xe. Cross relaxation from ^{131}Xe has been shown to be the dominant relaxation mechanism for ^{129}Xe at low temperature below 1000 G [190]. The polarized xenon is then combined at room temperature with 500 torr·cc (approximately 10^{19} molecules) of 99% enriched $^{13}CO_2$ (Isotec Inc.). After mixing for about 45 seconds the mixture is rapidly frozen into the sample tube, which is immersed in liquid nitrogen. During the freezing process, a static field of 150 G is applied to lengthen the spin-lattice relaxation time of the ^{129}Xe (which was estimated to be 15 seconds in zero field). The cross relaxation is accomplished by rapidly switching the field to a value B_{mix} for a duration τ_{mix} and then returning to 150 G. The sample is then removed from the liquid nitrogen bath and immediately transported to a field of 4.2 T for conventional high field ^{13}C NMR detection using a chemical shift echo sequence. Similar enhancement results are obtained for values of (B_{mix}, τ_{mix}) = (0.1 G, 200 ms), (10 G, ≈1 s), (35 G, ≈10 s) and Xe:$^{13}CO_2$ ratios of 6:1, 4:1, 1:1, and 1:4.

5.2.3 Results [191]

The enhanced spectrum of the 4:1 solid mixture is shown in figure 5.3a obtained with right circularly polarized light. As a frequency and sensitivity reference, the conventional NMR spectrum of gaseous $^{13}CO_2$ at 300K for a similar number (≈$5x10^{18}$) of molecules is shown in figure 5.3c. The chemical shift of 124.6 ppm is referenced to an external standard of liquid TMS. The measured values of the chemical shift tensor are $\sigma_\perp = 232.8 \pm 2.3$ and $\sigma_\parallel = -82.5 \pm 2.3$ ppm, extracted from the fit to the spectrum with the best signal-to-noise ratio, differ slightly from the values $\sigma_\perp = 245$ and $\sigma_\parallel = -90$ ppm reported by Beeler et al. [192] for CO_2 in a methane doped argon matrix at 20 K. The smaller anisotropy in the xenon matrix is almost certainly due to greater motion of the CO_2 at the higher temperature in the low field mixing experiment.

By comparing the integrated intensity of the laser-enhanced signal with the reference, an estimated enhancement factor of 250 is obtained in the best signal achieved, when corrected for differences in the number of spins. Since the xenon enhancement is approximately 18,000, which corresponds to a xenon polarization of 10%, equation 5.6 predicts a magnetization of about one half the xenon magnetization or ≈ 8,000. However the enhancement estimate does not account for the possibility that only a fraction of the of the total number of CO_2 molecules are in contact with the polarized xenon. This raises the question of the degree of dispersion of the CO_2 in the frozen xenon. The solid mixtures were prepared by opening a stopcock separating the two gases waiting about half a minute and allowing them to expand into the precooled sample region. No special measures were taken to confirm that a homogeneous matrix had been formed.

The spectrum in figure 5.3b demonstrates the inversion of the NMR signal occurring when the helicity of the pumping light is reversed. The population inversion may be interpreted as a reversal in the sign of the spin temperature and absolutely confirms that the magnetization source of the ^{13}C is the xenon (whose magnetization source is the rubidium electron, polarized by the light). Negative spin temperatures correspond to emissive NMR signals as illustrated in figure 5.3b.

It was attempted to study some other small molecules such as acetylene and trichloroethylene, with no success, probably due to the short T_1 of protons in low field. Low field mixing experiments with labeled carbon monoxide also did not work because it freezes out at ≈95K and did not condense fast enough in the liquid nitrogen to occlude in the rapidly freezing xenon. Thus, while attractive in its experimental simplicity, low field mixing appears to be rather limited in applicability.

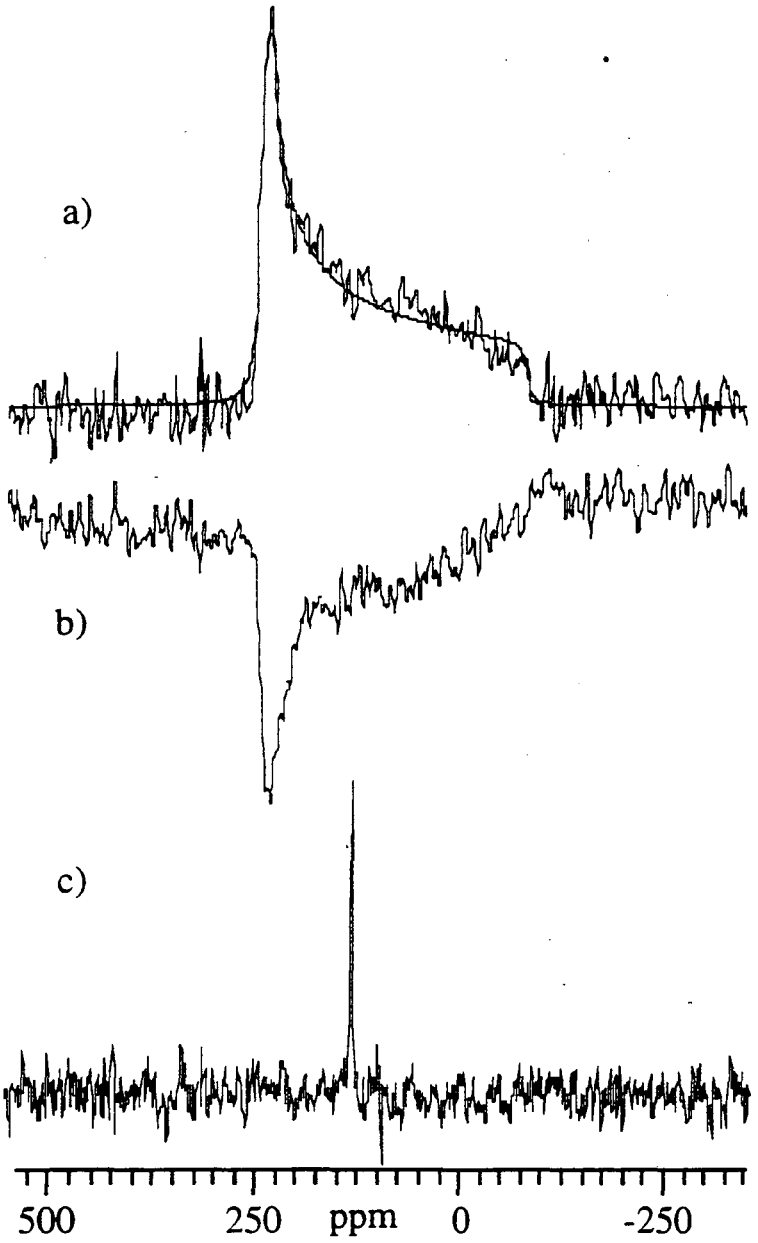

Figure 5.3 High field NMR spectra of $^{13}CO_2$. (a) σ^+ pumping light (b) σ^- pumping light (c) reference spectrum of $^{13}CO_2$ gas.

5.3 High Field Cross Polarization

The existence of cross relaxation and some of its implications were first discovered by Bloembergen and Pershan [193, 194] in 1959. However it was not until the pioneering paper of Hartmann and Hahn [10] that the possibilities for sensitivity enhancement in NMR were first realized. They made the fundamental discovery that matching energy levels of any two nuclei can be done in high magnetic field where the Zeeman splittings can be vastly different. It is done in the "doubly-rotating frame" with two resonant rf fields whose magnitudes are determined by the matching condition

$$\gamma_I H_I = \gamma_S H_S . \tag{5.7}$$

In the original experiment the resonance of an insensitive nucleus I (either due to a low gamma or low isotopic abundance) was detected by its effect on an abundant and easily observed nucleus S. Namely the magnetization of the abundant species was reduced when the appropriate matching field was applied to the other nucleus. This leads to high sensitivity but it is a very slow experiment as the spectrum must be mapped out point by point in the frequency domain. An improvement over this was discovered by Pines et al. [11] who introduced the idea of directly observing the insensitive nucleus in the time domain, a technique which is now called "cross polarization" or CP for short. This experiment allows all the advantages of fourier spectroscopy [60, 195] to be exploited as the entire spectrum is obtained in one shot. The signal to noise per unit time that can be achieved is a very significant improvement over direct signal averaging since the experiment can be recycled at the T_1 of the abundant species, usually much faster than a rare isotope. The matching field of the protons can also be left on to achieve decoupling during the acquisition phase leading to resolution enhancement. The actual dynamics underlying the transfer at the quantum mechanical level are quite complicated [196, 197] and will not be discussed here. It is sufficient to note that an equilibrium is typically

approached exponentially in a time on the order of the inverse dipolar coupling. There are many possible variations on this experiment, for example, if the $T_{1\rho}$ is long enough, the contact can be reestablished immediately after signal acquisition for another cross polarization period (see figure 5.4). Instead of cross polarizing directly to the rare spins, the dipolar reservoirs may be utilized to perform an adiabatic transfer of polarization, the most efficient transfer theoretically possible. (Recently slightly more stringent quantum limits have been suggested for the cross polarization transfer [129], however this is of no concern in the xenon experiments to be discussed.)

Another important implication of the cross polarization experiment mentioned in the introduction is the discrimination that it allows between nuclei in the sample. Only nuclei near the spins that serve as the magnetization source become polarized and are detected. This is because the magnetic dipole-dipole interaction is short range ($\alpha 1/r^3$) and is the basis of the polarization transfer. The properties of high field cross polarization are clearly of great utility in the application of laser-polarized xenon to the study of surfaces. After the xenon is adsorbed on a surface the polarization can be transferred with isotopic selectivity to any nucleus on the surface subject to purely technical constraints.

5.3.1 Results for Poly(triarylcarbinol) [198]

The ^{129}Xe NMR spectrum of xenon adsorbed on poly(triarylcarbinol) at -160°C is shown in figure 5.4a. Cross polarization *from* protons *to* xenon was previously investigated in this system in the previous chapter and dipolar contact exists below about -140°C (cf. figure 4.12). Xenon in both adsorption sites has an optimal contact time with the protons of 5 msec. In figure 5.4b the pulse sequence used for the ^{129}Xe to ^{1}H cross polarization experiment is shown. After the xenon is adsorbed the proton resonance is saturated by a train of 45° pulses to destroy any thermal polarization present before the magnetization transfer. The xenon is then spin-locked and a matching field applied to the protons. After a 5 msec contact period the matching fields are turned off and the proton magnetization is refocused using a dipolar echo to reduce the effects of the spectrometer

a)

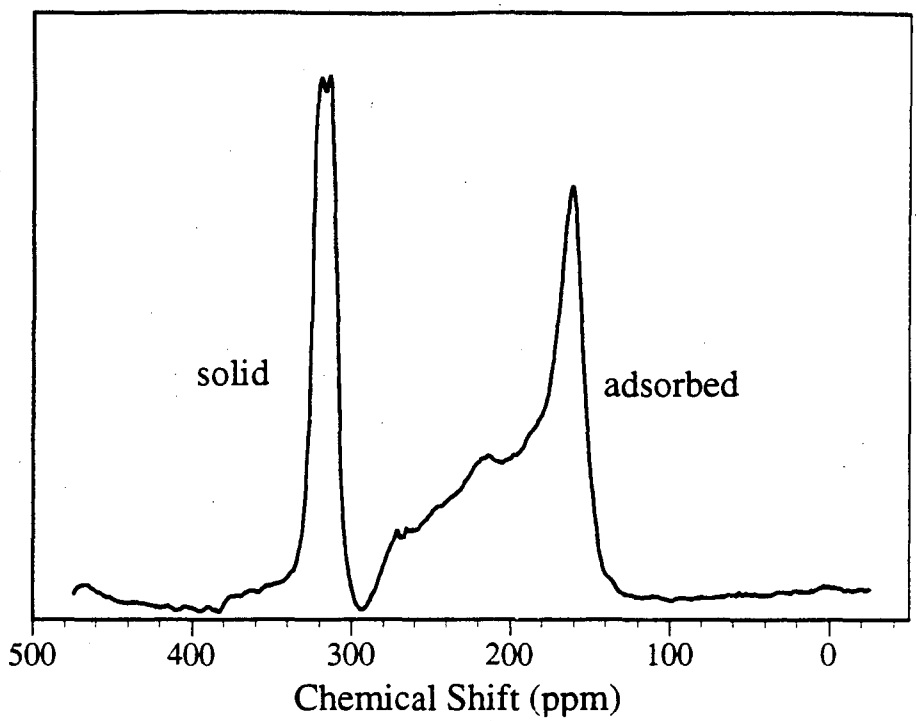

b)

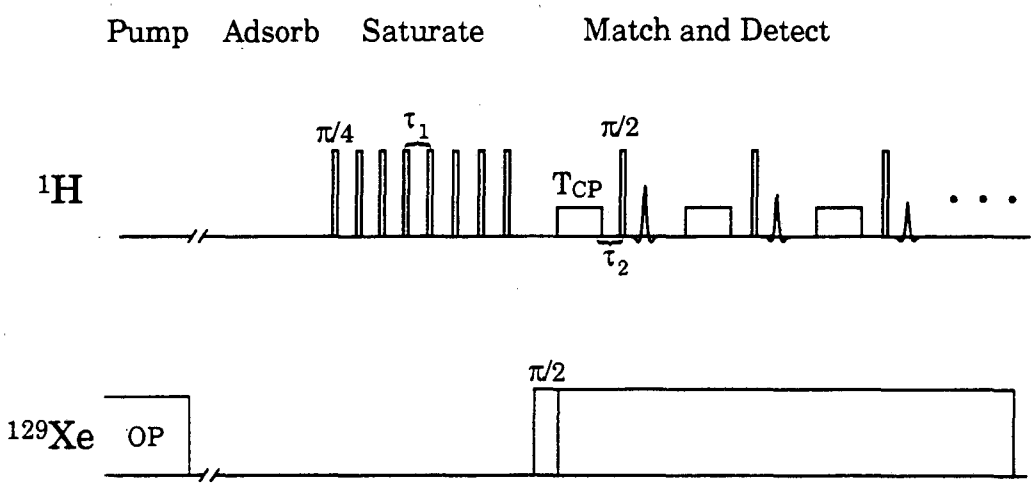

Figure 5.4 (a) Spectrum of adsorbed xenon. (b) Pulse sequence used in high field cross polarization experiment.

dead time. The resulting ^{1}H spectra are showed in figure 5.5a,b. The proton spectrum at these low temperatures is a 36 kHz broad gaussian due to the strong homonuclear dipole-dipole couplings. In figure 5.5b the helicity of the pumping light has been reversed resulting in an emissive spectra confirming that the polarization source for the protons is indeed the adsorbed xenon (as was shown previously for $^{13}CO_2$). No signal was obtained when the sequence was run immediately before the xenon was added or when the matching field amplitudes were deliberately misset. The sharp feature slightly out of phase in the center of the spectrum is due to the probe background; note that it is removed in the difference spectrum (figure 5.5c). Cross polarization by an adiabatic transfer method was also attempted, but was unsuccessful, probably due to the short $T_{1\rho}$ ($\approx$15 msec) of the adsorbed xenon on this polymer.

The ^{1}H signal was studied at several matching times, using a single contact experiment, and found to be consistent with the expected exponential dependence on ^{129}Xe-^{1}H contact time. At short times ($\leq$ 0.5 msec), the signal was very weak but could be enhanced by employing the multiple contact sequence of figure 5.4b. Figure 5.6 shows a comparison of the longest and shortest contact times used. The spectrum at the shortest contact time (0.2 msec, figure 5.6a) was perceptibly broader (43 kHz) than the equilibrium spectrum obtained by a simple echo sequence (36 kHz). At longer contact times (figure 5.6b) the line width approached the bulk equilibrium value, due to proton spin diffusion, consistent with a spin diffusion coefficient estimated to be $\approx$0.6 nm^2/msec. The difference in proton signals may be due to the morphology of the sample. Webster et al have speculated based on the swelling characteristics of this polymer that it could be made up of tightly cross linked kernels held together by loose strands [183]. It is plausible that these kernels have a slightly stronger dipolar coupling than the polymer as a whole, which would show up as a larger line width at short contact times if the xenon is in direct contact with these tightly cross linked regions.

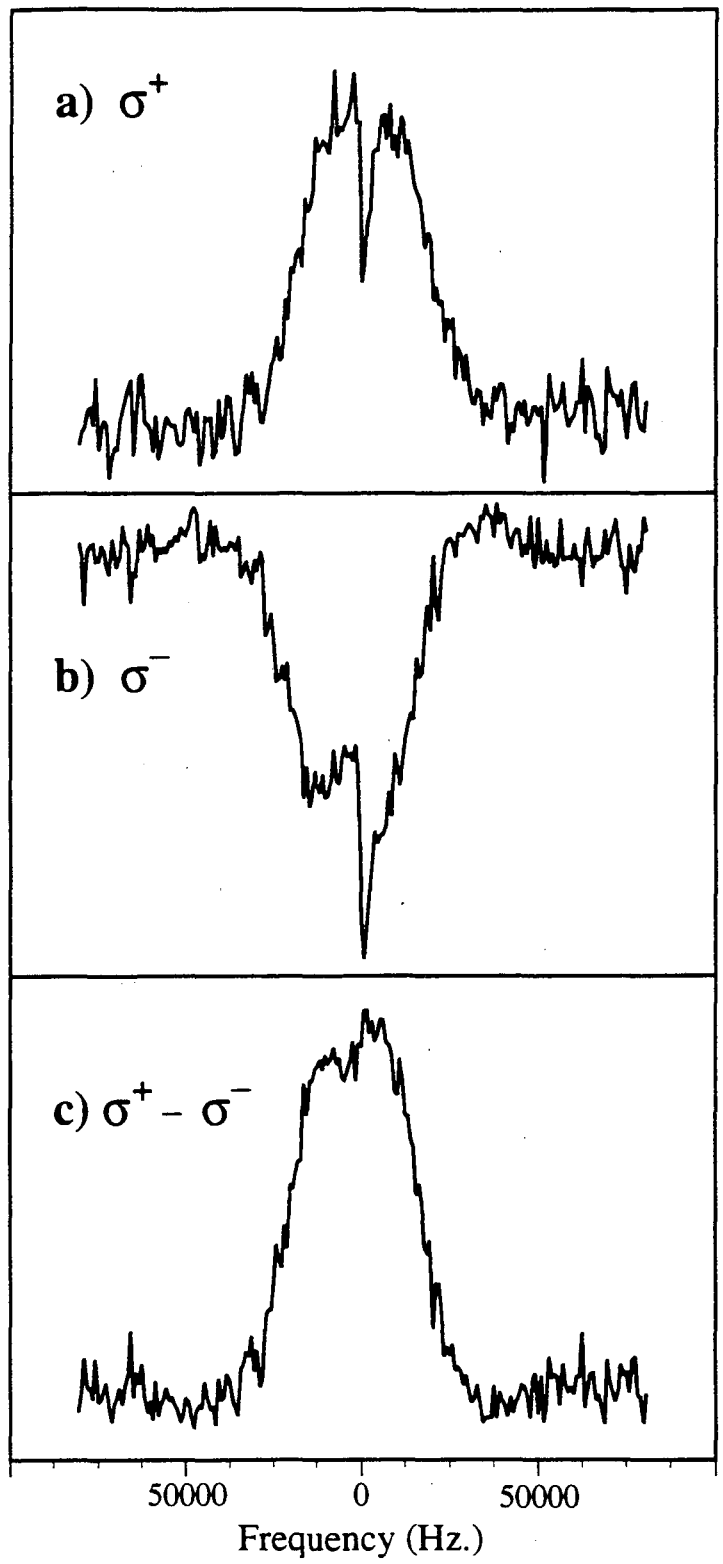

Figure 5.5 Proton spectra of poly(triarylcarbinol) enhanced by laser polarized xenon. T_{CP}=4 ms (1 contact).

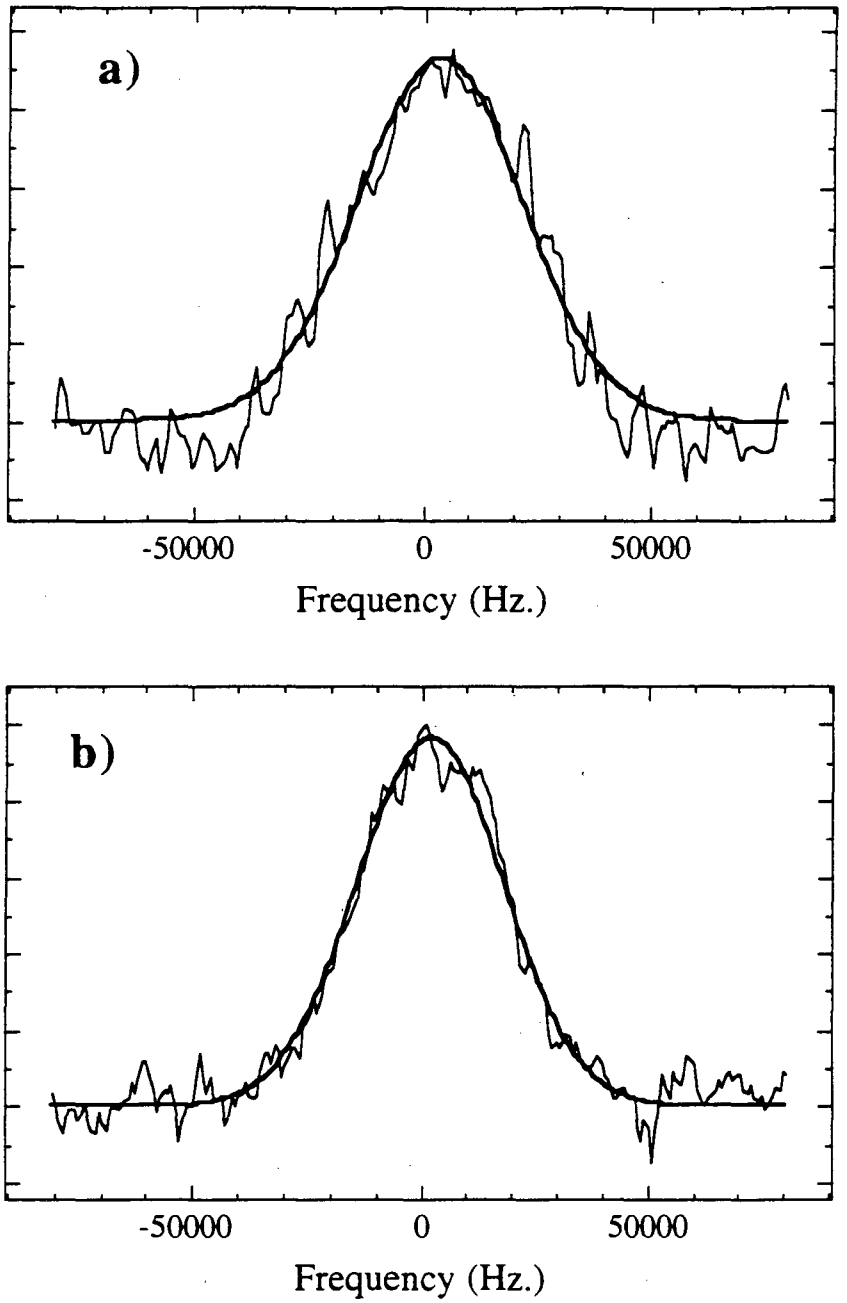

Figure 5.6 Proton spectra of poly(triarylcarbinol) obtained with (a) T_{CP}=200 us (8 contacts) and (b) T_{CP}=20 ms (1 contact).

As far as the signal enhancement, the signal obtained from the cross polarized protons, obtained with the optimal single contact time (20 msec, figure 5.6b), is estimated to have an enhancement in excess of 70. This estimate is based on the signal to noise in the time domain and the observation that no signal could be detected when thermally polarized xenon was used as the magnetization source.

In this section we have demonstrated that laser polarized, adsorbed xenon can be used to selectively transfer spin order to a surface directly in high magnetic field. The phase of the signal is absorptive or emissive depending on the optical preparation of the system providing a convenient way of discriminating against nuclei not in dipolar contact with the adsorbed xenon. Low surface area materials would be particularly suitable for this technique if the rapid surface diffusion (such as that observed on polymers in the previous chapter) can be quenched at sufficiently low temperatures without causing bulk condensation of the xenon. Variable contact time cross polarization studies may allow "depth profiling" of spin densities near the surface due to the geometric factors involved in the cross polarization dynamics.

5.4 Future Possibilities

5.4.1 Cross Relaxation with Quadrupolar Nuclei

It may prove possible to transfer spin order from laser polarized xenon to quadrupolar nuclei at surfaces. Quadrupolar nuclei pose special problems in high field when the quadrupolar interaction is made orientation dependent by the Zeeman interaction. In zero field, however, crystalline field gradients result in splittings which are independent of crystallite orientation and therefore narrow. Pure NQR, as it is known, has long been used to determine information about molecular symmetry, motion, and structure [199], but due to the low frequencies involved (1-10 MHz for most quadrupolar nuclei) sensitivity is a prime concern and limitation in many experiments. Figure 5.7a shows the one shot NQR

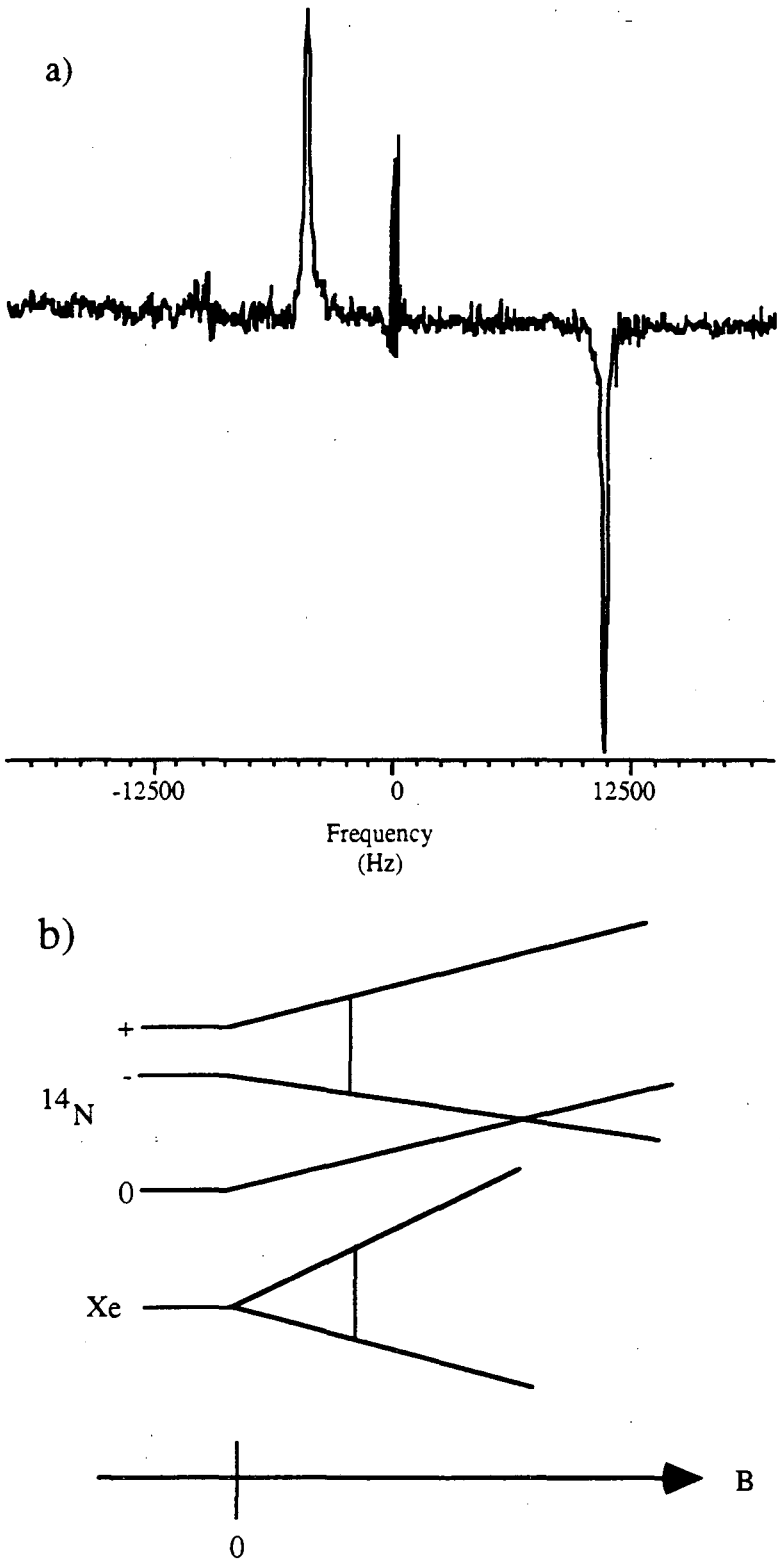

Figure 5.7 (a) Pure NQR spectrum of acetonitrile (≈$5x10^{22}$ nuclei, one scan) acquired at a frequency of 2.8 MHz. (b) Scheme for resonant cross relaxation between ^{129}Xe and ^{14}N.

spectrum of polycrystalline acetonitrile at 77K. It requires $\approx 5 \times 10^{22}$ nuclei to obtain this sensitivity.

It was shown many years ago that there can be a resonant interaction between a spin-1/2 nuclei and a quadrupolar nucleus at the appropriate magnetic field strength [200]. A possible scheme for matching the energy levels of ^{129}Xe to a spin-1 nucleus, such as ^{14}N, with a non-zero asymmetry parameter is shown in figure 5.7b. When the magnetic field strength is set at the appropriate value, the spin temperature should equalize between the two systems and thus enhance the population difference between the |+> and |-> eigenstates in zero field. This difference can then be observed at the much larger ν_+ and ν_- transition frequencies (seen in figure 5.7a) which determine uniquely the two parameters (quadrupolar coupling constant and asymmetry) in the quadrupolar Hamiltonian. Preliminary experiments indicate that the sensitivity may be sufficient for certain ^{14}N systems such as cyano (CN) groups if the inhomogeneous broadening is not too large.

5.4.2 Experimental Prospects

The above examples of polarization transfer show some of the exciting possibilities that can be imagined with this technique. The high field technique seems particularly promising, especially if extended to low gamma or less abundant nuclei. These might be polarized either directly from the xenon, or in a second cross polarization step from protons, which will have a much stronger dipolar interaction with such nuclei. Possible nuclei include ^{13}C or ^{29}Si. which should have higher resolution than the ^{1}H spectra described in section 4.3 and contain correspondingly more information about surface chemistry.

The capabilities of the high field cross polarization experiment would be enhanced by performing it at 77K or below. When the bulk freezing difficulties are overcome this will allow cross polarization on a wide range of surfaces as both the coupling and spin-lattice relaxation will become more favorable.

Other possible improvements include a continuous gas flow system such as that demonstrated for hydrogen [201]. This would allow two dimensional experiments, such as the exchange experiment discussed in chapter one, to be performed with laser polarized xenon. While there are no direct technical obstacles to this, the polarization transfer from rubidium to xenon might be too slow to allow a large flux at significant polarization levels. However, it has been reported recently that deuterium polarized by spin-exchange optical pumping achieved a flow rate of $\approx 10^{17}$ atoms/sec at 70% polarization [202].

Pure spin physics of highly polarized spin systems has long been of considerable interest in the magnetic resonance field [203]. Laser polarized xenon may be useful for studying such phenomena as the breakdown of the high temperature approximation [204, 205], nuclear spin ordering [206], demagnetizing field effects [207, 208], NMR lasers [209], etc.

Bibliography

[1] A. Abragam, *Principles of Nuclear Magnetism* (Oxford University Press, 1960).

[2] U. Haeberlen, *High Resolution NMR in Solids: Selective Averaging*. J. S. Waugh, Ed., Advances in Magnetic Resonance (Academic Press, New York, 1976).

[3] E.W. Wooten, K.T. Mueller, A. Pines, *Accounts of Chemical Research,* **25**, 209 (1992).

[4] R.J. Knize, Z. Wu, W. Happer, *Adv. in At. and Mol. Phys.,* **24**, 223 (1988).

[5] D.I. Hoult, R.E. Richards, *J. Mag. Res.,* **24**, 71 (1976).

[6] J.S. Waugh, P.C. Hammel, P.L. Kuhns, O. Gonen, *Bull. Mag. Reson.,* **11**, 97 (1988).

[7] J.S. Waugh, P.C. Hammel, P.L. Kuhns, O. Gonen, *Phys. Rev. B,* **35**, 4591 (1987).

[8] O. Gonen, P.L. Kuhns, C. Zuo, J.S. Waugh, *J. Mag. Reson.,* **81**, 491 (1989).

[9] O. Gonen, P.L. Kuhns, J.S. Waugh, J.P. Fraissard, *J. Phys. Chem.,* **93**, 504 (1989).

[10] S.R. Hartmann, E.L. Hahn, *Phys. Rev.,* **128**, 2042 (1962).

[11] A. Pines, M. Gibby, J.S. Waugh, *J. Chem. Phys.*, **59**, 569 (1973).

[12] G. Feher, *Phys. Rev.*, **105**, 1122 (1957).

[13] M. Goldman, *Spin Temperature and Nuclear Magnetic Resonance in Solids* (Oxford Univ. Press, Oxford, 1970).

[14] G.L. Closs, *Advances in Magnetic Resonance*, **7**, 157 (1974).

[15] R.G. Lawler, *Progress in NMR Spectroscopy*, **9**, 145 (1975).

[16] C.R. Bowers, D.P. Weitekamp, *Phys. Rev. Lett.*, **57**, 2645 (1986).

[17] C.R. Bowers, D.P. Weitekamp, *J. Am. Chem. Soc.*, **109**, 5541 (1987).

[18] C. Hermann, G. Lampel, V.I. Safarov, *Ann. Phys. Fr.*, **10**, 1117 (1985).

[19] I.I. Rabi, J.R. Zacharias, S. Millman, P. Kusch, *Phys. Rev.*, **53**, 318 (1938).

[20] C.P. Slichter, *Principles of Magnetic Resonance* (Springer-Verlag, Berlin, 1990).

[21] W. Lamb, *Physical Review*, **60**, 817 (1941).

[22] D.W. Davies, *The Theory of Electric and Magnetic Properties of Molecules* (Wiley, New York, 1967).

[23] G. Malli, C. Froese, *Inter. J. of Quant. Chem.*, **1**, 99 (1967).

[24] G.J. Schrobilgen, The Noble Gases, in *NMR and The Periodic Table* R. K. Harris, B. E. Mann, Eds. (Academic Press, New York, 1978) p. 439.

[25] N.F. Ramsey, *Phys. Rev.*, **103**, 20 (1956).

[26] C.J. Jameson, *Bulletin of Magnetic Resonance*, **3**, 3 (1980).

[27] C.J. Jameson, *Chem. Rev.*, **91**, 1375 (1991).

[28] D. Raftery, H. Long, L. Reven, P. Tang, A. Pines, *Chem. Phys. Lett.*, **191**, 385 (1992).

[29] M. Mehring, *Principles of High Resolution NMR in Solids* (Springer, Berlin, 1983).

[30] S.J. Opella, J.S. Waugh, *J. Chem. Phys.*, **66**, 4919 (1977).

[31] K.W. Miller, N.V. Reo, D.P. Stengle, T.R. Stengle, K.L. Williamson, *Proc. Natl. Acad. Sci. USA*, **78**, 4946 (1981).

[32] T. Ito, J. Fraissard, *J. Phys. Chem.*, **76**, 5225 (1982).

[33] J.A. Ripmeester, *J. Am. Chem. Soc.*, **104**, 289 (1982).

[34] J.A. Ripmeester, C.I. Ratcliffe, J.S. Tse, *J. Chem. Soc., Faraday Trans. 1,* **84**, 3731 (1988).

[35] B.F. Chmelka, L.C.d. Menorval, R. Csencsits, R. Ryoo, S.-B. Liu, C.J. Radke, E.E. Petersen, A. Pines, in *Structure and Reactivity of Surfaces* C. Morterra, Ed. (Elsevier, Amsterdam, 1989) p. 269.

[36] P.-K. Wang, J.-P. Ansermet, S.L. Rudaz, Z. Wang, S. Shore, C.P. Slichter, J.H. Sinfelt, *Science,* **234**, 35 (1986).

[37] R. Grosse, R. Burmeister, B. Boddenberg, A. Gedeon, J. Fraissard, *J. Phys. Chem.,* **95**, 2443 (1991).

[38] J.A. Ripmeester, D.W. Davidson, *Journal of Molecular Structure,* **75**, 67 (1981).

[39] T.R. Stengle, K.L. Williamson, *Macromolecules,* **20**, 1428 (1987).

[40] D. Raftery, L. Reven, H. Long, A. Pines, P. Tang, J. Reimer, *J. Phys. Chem.,* **97**, 1649 (1993).

[41] T. Ito, J. Fraissard, *Zeolites,* **8**, 350 (1988).

[42] P.J. Barrie, J. Klinowski, *Prog. in NMR Spec.,* **24**, 91 (1992).

[43] C. Dybowski, N. Bansal, T.M. Duncan, *Ann. Rev. Phys. Chem.,* **42**, 433 (1991).

[44] M.D. Raftery, B.F. Chmelka, Xenon NMR Spectroscopy, in *NMR Basic Principles and Progress* B. Blü mich, R. Kosfeld, Eds. (Springer-Verlag, Berlin, 1993).

[45] M. Schadt, *Liquid Crystals,* **5**, 57 (1989).

[46] S.W. Depp, W.E. Howard, in *Scientific American* . 1993), pp. 90.

[47] J.W. Doane, NMR of Liquid Crystals, in *Magnetic Resonance of Phase Transitions* C. P. Poole, H. A. Farach, Eds. (Academic Press, 1979) pp. 171.

[48] A. Lowenstein, M. Brenman, *Chem. Phys. Lett.,* **58**, 435 (1978).

[49] P. Ingman, J. Jokasaari, P. Diehl, *J. Mag. Reson.,* **92**, 163 (1991).

[50] J. Jokisaari, P. Ingman, J. Lounila, O. Pulkkinen, P. Diehl, O. Muenster, *Mol. Phys.,* **78**, 41 (1993).

[51] R.J. Ondris-Crawford, G.P. Crawford, S. Zumer, J.W. Doane, *Phys. Rev. Lett.,* **70**, 194 (1993).

[52] H. Hsiung, T. Rasing, Y.R. Shen, *Phys. Rev. Lett.,* **57**, 3065 (1986).

[53] G.P. Crawford, D.K. Yang, S. Zumer, D. Finotello, J.W. Doane, *Phys. Rev. Lett.,* **66**, 723 (1991).

[54] P.G. de Gennes, *The Physics of Liquid Crystals* (Oxford University Press, 1974).

[55] G.P. Crawford, L.M. Steele, R. Ondris-Crawford, G.S. Iannacchione, C.J. Yeager, J.W. Doane, D. Finotello, *J. Chem. Phys.*, **96**, 7788 (1992).

[56] J. Jokisaari, P. Diehl, O. Muenster, *Mol. Cryst. Liq. Cryst.*, **188**, 189 (1990).

[57] J. Jokisaari, P. Diehl, *Liquid Crystals*, **7**, 739 (1990).

[58] P. Diehl, J. Jokisaari, *Chem. Phys. Lett.*, **165**, 389 (1990).

[59] J. Jeener, B.H. Meier, P. Bachmann, R.R. Ernst, *J. Chem. Phys.*, **71**, 4546 (1979).

[60] R.R. Ernst, G. Bodenhausen, A. Wokaun, *Principle of Nuclear Magnetic Resonance in One and Two Dimensions* (Oxford, Clarendon, 1987).

[61] G.P. Crawford, R. Stannarius, J.W. Doane, *Phys. Rev. A*, **44**, 2558 (1991).

[62] J.H. Erdmann, S. Zumer, J.W. Doane, *Phys. Rev. Lett.*, **64**, 1907 (1990).

[63] B.F. Chmelka, D. Raftery, A.V. McCormick, L.C.d. Menorval, R.D. Levine, A. Pines, *Phys. Rev. Lett.*, **66**, 580 (1991).

[64] C.J. Jameson, A.K. Jameson, R. Gerald, A.C. DeDios, *J. Chem. Phys.*, **96**, 1676 (1992).

[65] R. Larsen, J. Shore, K. Schmidt-Rohr, L. Emsley, H. Long, A. Pines, M. Janicke, B.F. Chmelka, *Chem. Phys. Lett.*, **submitted**, (1993).

[66] A. Kastler, *J. Phys. Radium*, **11**, 255 (1950).

[67] J. Brossel, A. Kastler, J. Winter, *J. Phys. Radium*, **13**, 668 (1952).

[68] W.B. Hawkins, R.H. Dicke, *Phys. Rev.*, **91**, 1008 (1953).

[69] L.W. Anderson, F.M. Pipkin, J.C. Baird, *Phys. Rev.*, **120**, 1279 (1961).

[70] A. Kastler, *J. Opt. Soc. Am.*, **53**, 902 (1963).

[71] H.G. Robinson, T. Myint, *App. Phys. Lett.*, **5**, 116 (1964).

[72] J. Dupont-Roc, S. Haroche, C. Cohen-Tannoudji, *Phys. Lett.*, **28A**, 638 (1969).

[73] H. Hellwig, in *Precision Measurements and Fundemental Constants II* B. N. Taylor, W. D. Phillips, Eds. (NBS Spec. Publ., 1984), vol. 617, p. 11.

[74] H.G. Dehmelt, *Phys. Rev.*, **109**, 381 (1958).

[75] E.M. Purcell, G.B. Field, *Astrophys. J.*, **124**, 542 (1956).

[76] R.J. McNeal, R.A. Bernheim, R. Bersohn, M. Dorfman, *J. Chem. Phys.*, **40**, 1678 (1964).

[77] R.J. McNeal, *J. Chem. Phys.*, **37**, 2726 (1962).

[78] R.A. Bernheim, *Optical Pumping: An Introduction* in Frontiers in Chemistry (Benjamin, New York, 1965).

[79] B.C. Grover, *Phys. Rev. Lett.*, **40**, 390 (1978).

[80] W. Happer, E. Miron, S. Schaefer, D. Schreiber, W.A.v. Wijngaarden, X. Zeng, *Phys. Rev. A*, **29**, 3092 (1984).

[81] X. Zeng, Z. Wu, T. Call, E. Miron, D. Schreiber, W. Happer, *Phys. Rev. A*, **31**, 260 (1985).

[82] J. Barat, C. Cohen-Tannoudji, *Compt. Rend.*, **252**, 93 (1961).

[83] C. Cohen-Tannoudji, *Ann. Phys. (France)*, **7**, 423 (1962).

[84] A. Kastler, *J. Opt. Soc.*, **47**, 460 (1957).

[85] T.R. Carver, *Science*, **141**, 599 (1963).

[86] A. Kastler, *Science*, **158**, 214 (1967).

[87] C. Cohen-Tannoudji, A. Kastler, Optical Pumping, in *Progress in Optics* E. Wolf, Ed. (1966), vol. 5, p. 1.

[88] W. Happer, *Rev. Mod. Phys.*, **44**, 169 (1972).

[89] L.C. Balling, Optical Pumping, in *Advances in Quantum Electronics* P. W. Goodwin, Ed. (Academic Press, New York, 1975), vol. 3, pp. 1.

[90] W. Happer, W.A.v. Wijngaarden, *Hyperfine Interactions,* **38**, 435 (1987).

[91] P.W. Atkins, *Molecular Quantum Mechanics* (Oxford University Press, London, 1983).

[92] J.C. Camparo, *American Journal of Physics,* **51**, 1077 (1983).

[93] W. Happer, *Ann. Phys. Fr.,* **10**, 645 (1985).

[94] C.C. Bouchiat, M.A. Bouchiat, L.C. Pottier, *Phys. Rev.,* **181**, 144 (1969).

[95] M.A. Bouchiat, J. Brossel, L.C. Pottier, *J. Chem. Phys.,* **56**, 3703 (1972).

[96] N.D. Bhaskar, W. Happer, M. Larsson, X. Xeng, *Phys. Rev. Lett.,* **50**, 105 (1983).

[97] R.M. Herman, *Phys. Rev.,* **137**, 1062 (1965).

[98] R.L. Gamblin, T.R. Carver, *Phys. Rev.,* **138**, 946 (1965).

[99] N.D. Bhaskar, W. Happer, T. McClelland, *Phys. Rev. Lett.,* **49**, 25 (1982).

[100] T.E. Chupp, M.E. Wagshul, K.P. Coulter, A.B. McDoñald, W. Happer, *Phys. Rev. C,* **36**, 2244 (1987).

[101] T.E. Chupp, K.P. Coulter, *Phys. Rev. Lett.,* **55**, 1074 (1985).

[102] C.H. Volk, J.G. Mark, B.C. Grover, *Phys. Rev. A,* **20**, 2381 (1979).

[103] S.R. Schaefer, G.D. Cates, W. Happer, *Phys. Rev. A,* **41**, 6063 (1990).

[104] M. Kitano, M. Bourzutschky, F.P. Calprice, J. Clayhold, W. Happer, M. Musolf, *Phys. Rev. C,* **34**, 1974 (1986).

[105] M. Augustine, K. Zilm, 35th Rocky Mountain Conference Denver, CO, (1993).

[106] V. Lefevre-Seguin, J. Brossel, *J. Low Temp. Phys.,* **72**, 165 (1988).

[107] X. Zeng, C. Wu, M. Zhao, S. Li, L. Li, X. Zhang, Z. Liu, W. Liu, *Chem. Phys. Lett.,* **182**, 538 (1991).

[108] D. Raftery, H. Long, T. Meersmann, P.J. Grandinetti, L. Reven, A. Pines, *Phys. Rev. Lett.,* **66**, 584 (1991).

[109] C.H. Volk, T.M. Kwon, J.G. Mark, Y.B. Kim, J.C. Woo, *Phys. Rev. Lett.,* **44**, 136 (1980).

[110] T.M. Kwon, J.G. Mark, C.H. Volk, *Phys. Rev. A,* **24**, 1894 (1981).

[111] Z. Wu, W. Happer, J. Daniels, *Phys. Rev. Lett.*, **59**, 1480 (1987).

[112] Z. Wu, W. Happer, M. Kitano, J. Daniels, *Phys. Rev. A*, **42**, 2774 (1990).

[113] S.K. Lamoreaux, J.P. Jacobs, B.R. Heckel, F.J. Raab, E.N. Fortson, *Phys. Rev. A*, **39**, 1082 (1989).

[114] T.E. Chupp, R.J. Hoare, R.A. Loveman, E.R. Orteiza, J.M. Richardson, M.E. Wagshul, A.K. Thompson, *Phys. Rev. Lett.*, **63**, 1542 (1989).

[115] T.E. Chupp, R.J. Hoare, *Phys. Rev. Lett.*, **64**, 2261 (1990).

[116] P.K. Majumder, B.J. Venema, S.K. Lamereaux, B.R. Heckel, E.N. Fortson, *Phys. Rev. Lett.*, **65**, 2931 (1990).

[117] A.J. Shaka, J. Keeler, *Prog. in NMR Spec.*, **19**, 47 (1987).

[118] T. Killian, *Phys. Rev.*, **27**, 578 (1926).

[119] C. Cohen-Tannoudji, *J. Phys. Radium*, **24**, 653 (1963).

[120] E.L. Hahn, *Phys. Rev.*, **80**, 580 (1950).

[121] R.M. Sternheimer, *Phys. Rev.*, **105**, 158 (1957).

[122] M.R. Keenan, L.W. Buxton, E.J. Cambell, T.J. Balle, W. Flygare, *J. Chem. Phys.*, **73**, 3523 (1980).

[123] M.W. Garrett, *J. Appl. Phys.*, **38**, 2563 (1967).

[124] M.D. Raftery, PhD. Thesis, University of California, Berkeley (1992).

[125] R.G. Brewer, *Review of Scientific Instruments,* **32**, 1356 (1961).

[126] D.P. Weitekamp, A. Bielecki, D. Zax, K. Zilm, A. Pines, *Physical Review Letters,* **50**, 1807 (1983).

[127] D.B. Zax, A. Bielecki, K.W. Zilm, A. Pines, D.P. Weitekamp, *Journal of Chemical Physics,* **83**, 4877 (1985).

[128] W.G. Breiland, C.B. Harris, A. Pines, *Phys. Rev. Lett.*, **30**, 158 (1973).

[129] L. Emsley, A. Pines, Lectures on Pulsed NMR, in *Nuclear Magnetic Double Resonance* B. Maraviglia, Ed. (1993).

[130] S. Meiboom, D. Gill, *Review of Scientific Instruments,* **29**, 6881 (1958).

[131] M.H. Levitt, R. Freeman, T. Frenkiel, *Journal of Magnetic Resonance,* **50**, 157 (1982).

[132] A.T. Nicol, Nuclear Moment Alignment, Relaxation and Detection, Air Force Technical Report, AFOSR-TR-82-0418 (1982).

[133] A.T. Nicol, *Phys. Rev. B,* **29**, 2397 (1984).

[134] Z. Liu, X. Sun, X. Zeng, Q. He, *Chin. Phys. Lett.*, **7**, 399 (1990).

[135] F.D. Doty, R.R. Inners, P. Ellis, *J. Magn. Reson.*, **43**, 399 (1981).

[136] J.C. Camparo, *Contemp. Physics*, **26**, 443 (1985).

[137] P.F. Moulton, in *Photonics Spectra* . 1991), pp. 191.

[138] P.F. Moulton, in *Photonics Spectra* . 1991), pp. 123.

[139] M.E. Wagshul, T.E. Chupp, *Phys. Rev. A*, **40**, 4447 (1989).

[140] H. Hemmati, *Appl. Phys. Lett.*, **51**, 224 (1987).

[141] S.C. Wang, R.E. Stone, SPIE Free Space Laser Communication Technologies II (1990), vol. 1218, p. 278.

[142] Spectra Diode Labs, *Laser Focus World*, January 1993, p. 83.

[143] T.E. Chupp, E.R. Orteiza, J.M. Richardson, T.R. White, *Phys. Rev. A*, **38**, 3998 (1988).

[144] D. Brinkmann, H.Y. Carr, *Phys. Rev.*, **150**, 174 (1966).

[145] W.S. Warren, R.E. Norberg, *Phys. Rev.*, **148**, 402 (1966).

[146] J. Lurie, J.L. Feldman, G.K. Horton, *Phys. Rev.*, **150**, 180 (1966).

[147] D.F. Cowgill, R.E. Norberg, *Phys. Rev. B*, **6**, 1636 (1972).

[148] W.M. Yen, R.E. Norberg, *Phys. Rev.*, **131**, 269 (1963).

[149] M.S. Petterson, D.L. Goodstein, *Surf. Sci.*, **209**, 455 (1989).

[150] G. Neue, *Zeit. Phys. Chem. Neue Folge*, **152**, 271 (1987).

[151] G. Tastevin, P.J. Natcher, L. Weisenfeld, M. Leduc, F. Laloë, *J. Phys. Fr.*, **49**, 1 (1988).

[152] S.C.-K. Chu, Y. Xu, J.A. Balschi, C.S. Springer, *Mag. Reson. in Med.*, **13**, 239 (1990).

[153] N. Ramsey, *Nuclear Moments* (Wiley, New York, 1953).

[154] J.R. Zimmerman, M.R. Foster, *J. Phys. Chem*, **61**, 282 (1957).

[155] N. Bloembergen, T.J. Rowland, *Phys. Rev.*, **97**, 1679 (1955).

[156] H.Y. Carr, E.M. Purcell, *Phys. Rev.*, **94**, 630 (1954).

[157] R.C. Weast, Eds., *CRC Handbook of Chemistry and Physics* (CRC Press, Boca Raton, 1990).

[158] J.R. Packard, C.A. Swenson, *J. Phys. Chem. Solids,* **24**, 1405 (1963).

[159] D. Brinkmann, *Phys. Rev. Lett.,* **13**, 187 (1964).

[160] D.J. Suh, T.-J. Park, S.-K. Ihm, R. Ryoo, *J. Phys. Chem.,* **95**, 3767 (1991).

[161] G. Neue, *J. Mag. Reson.,* **78**, 555 (1988).

[162] J.-P. Korb, D.C. Torney, H.M. McConnell, *J. Chem. Phys.,* **78**, 5782 (1983).

[163] J.-P. Korb, M. Winterhalter, H.M. McConnell, *J. Chem. Phys.,* **80**, 1059 (1984).

[164] N. Bloembergen, E.M. Purcell, R.V. Pound, *Phys. Rev,* **73**, 679 (1948).

[165] S. Leutwyler, J. Jortner, *J. Phys. Chem.,* **91**, 5558 (1987).

[166] R.J. Birgeneau, P.M. Horn, *Science,* **232**, 329 (1986).

[167] H. Hong, C.J. Peters, A. Mak, R.J. Birgeneau, P.M. Horn, H. Suematsu, *Phys. Rev. B,* **40**, 4797 (1989).

[168] T. Shibanuma, H. Asada, S. Ishi, T. Matsui, *Japanese Journal of Applied Physics,* **22**, 1656 (1983).

[169] S. Brunauer, P.H. Emmet, E. Teller, *J. Am. Chem. Soc.,* **60**, 309 (1938).

[170] T.L. Hill, *J. Chem. Phys.*, **14**, 263 (1946).

[171] T.L. Hill, Theory of Physical Absorption, in *Advances in Catalysis* (1952), vol. 6, p. 211.

[172] M.P. Freeman, G.D. Halsley, *J. Phys. Chem.*, **60**, 1119 (1956).

[173] M.L. Smith, C. Dybowski, *J. Phys. Chem.*, **95**, 4942 (1991).

[174] C.J. Jameson, A.K. Jameson, S. Cohen, *J. Chem. Phys.*, **59**, 4540 (1973).

[175] G.A. Somorjai, *Chemistry in Two Dimensions: Surfaces* (Cornell University Press, Ithaca, NY, 1981).

[176] T.T.P. Cheung, C.M. Fu, S. Wharry, *J. Phys. Chem.*, **92**, 5170 (1988).

[177] T.T.P. Cheung, *J. Phys. Chem.*, **93**, 7549 (1989).

[178] W.C. Conner, E.L. Weist, T. Ito, J. Fraissard, *J. Phys. Chem.*, **93**, 4138 (1989).

[179] J. Tabony, *Progress in NMR Spectroscopy*, **14**, 1 (1980).

[180] J. Tabony, T. Cosgrove, *Chem. Phys. Lett.*, **67**, 103 (1979).

[181] J.H. Walton, J.B. Miller, C.M. Rowland, *J. Polym. Sci. B*, **30**, 527 (1992).

[182] D. Schulze, H. Ernst, D. Fenzke, W. Meiler, H. Pfeifer, *J. Phys. Chem.*, **94**, 3499 (1990).

[183] O.W. Webster, F.P. Gentry, R.D. Farlee, B.E. Smart, *Makromol. Chem., Macromol. Symp.*, **54/55**, 477 (1992).

[184] J.A. Ripmeester, C.I. Ratcliffe, *J. Phys. Chem.*, **94**, 7652 (1990).

[185] G.E. Maciel, D.W. Sindorf, *J. Am. Chem. Soc.*, **102**, 7606 (1980).

[186] Walters, Turner, E. Oldfield, *J. Mag. Reson.*, **76**, 106 (1988).

[187] N. Zumbulyadis, J.M. O'Reilly, *Macromolecules*, **24**, 5294 (1991).

[188] M. Afeworki, R.A. McKay, J. Schaeffer, *Macromolecules*, **25**, 4084 (1992).

[189] A. Abragam, W.G. Procter, *Phys. Rev.*, **109**, 1441 (1958).

[190] M. Gatzke, G.D. Cates, B. Driehuys, D. Fox, W. Happer, B. Saam, *Phys. Rev. Lett.*, **70**, 690 (1993).

[191] C.R. Bowers, H.W. Long, T. Pietrass, H.C. Gaede, A. Pines, *Chem. Phys. Lett.*, **205**, 168 (1993).

[192] A.J. Beeler, A.M. Orendt, D.M. Grant, P.W. Cutts, J. Michl, K.W. Zilm, J.W. Downing, J.C. Facelli, M.S. Schindler, W. Kutzelnigg, *J. Am. Chem. Soc.*, **106**, 7672 (1984).

[193] N. Bloembergen, P.P. Sorokin, *Phys. Rev.*, **110**, 865 (1958).

[194] N. Bloembergen, S. Shapiro, P.S. Pershan, J.O. Artman, *Phys. Rev.*, **114**, 445 (1959).

[195] R.R. Ernst, W.A. Anderson, *Rev. Sci. Instr.*, **37**, 93 (1966).

[196] D.A. McArthur, E.L. Hahn, R.E. Walstedt, *Phys. Rev.*, **188**, 609 (1969).

[197] D.E. Demco, J. Tegenfeldt, J.S. Waugh, *Phys. Rev. B*, **11**, 4133 (1975).

[198] H.W. Long, H.C. Gaede, J. Shore, L. Reven, C.R. Bowers, J. Kritzenberger, T. Pietrass, A. Pines, P. Tang, J.A. Reimer, *J. Am. Chem. Soc.*, **in press**, (1993).

[199] T.P. Das, E. Hahn, Nuclear Quadrupole Resonance Spectroscopy, (Academic Press, 1958).

[200] M. Goldman, A. Landesman, *Phys. Rev.*, **132**, 610 (1963).

[201] S.G. Redsun, R.J. Knize, G.D. Cates, W. Happer, *Phys. Rev. A*, **42**, 1293 (1990).

[202] K.P. Coulter, R.J. Hoult, E.R. Kinney, R.S. Kowalczyk, D.H. Potterveld, L. Young, B. Zeidman, A. Zghiche, D.K. Toporkov, *Phys. Rev. Lett.*, **68**, 174 (1992).

[203] A. Abragam, M. Goldman, *Nuclear Magnetism: Order and Disorder* (Oxford University Press, 1986).

[204] A. Abragam, M. Chapellier, J.F. Jacquinot, M. Goldman, *J. Mag. Reson.*, **10**, 322 (1973).

[205] J.S. Waugh, O. Gonen, P. Kuhns, *J. Chem. Phys.*, **86**, 3816 (1987).

[206] A. Abragam, *Proc. R. Soc. Lond. A*, **412**, 255 (1987).

[207] G. Deville, M. Bernier, J.M. Delrieux, *Phys. Rev. B*, **19**, 5666 (1979).

[208] R. Bowtell, R.M. Bowley, P. Glover, *J. Mag. Reson.*, **88**, 643 (1990).

[209] P. Bosiger, E. Brun, D. Meier, *Phys. Rev. Lett.*, **38**, 602 (1977).

LAWRENCE BERKELEY LABORATORY
UNIVERSITY OF CALIFORNIA
TECHNICAL INFORMATION DEPARTMENT
BERKELEY, CALIFORNIA 94720